**UNIVERSIDADE DE SANTIAGO
DE COMPOSTELA**

FACULTAD DE FÍSICA

Departamento de Física de Partículas

Measurement of the U-234(n,f) cross section with PPAC detectors at the n_TOF facility

Memoria presentada para
optar al Grado de Doctor
en Ciencias Físicas por:

Carlos Paradela Dobarro
Junio 2005

Ignacio Durán Escribano, Profesor Titular
de la **Universidad de Santiago de Compostela**,

CERTIFICO: que la memoria titulada **" Measurement of the U-234(n,f) cross section with PPAC detectors at the n_TOF facility"**, ha sido realizada por **Carlos Paradela Dobarro** bajo mi dirección en el **Departamento de Física de Partículas** de esta Universidad, y constituye la Tesis que presenta para optar al grado de **Doctor en Ciencias Físicas**.

Santiago de Compostela, 26 de Mayo de 2005

Prof. Ignacio Durán Escribano   **Carlos Paradela Dobarro**

AGRADECIMIENTOS

Para empezar me gustaría agradecer a mi tutor Ignacio Durán el haberme dado la oportunidad de trabajar en este apasionante mundo que es la Física Nuclear introduciendome en la Colaboración n_TOF, así como su siempre optimista punto de vista sobre este trabajo de tesis.

El número de personas al que tengo que agradecer alguna contribución en este trabajo se dispara, mereciendo mención especial: Daniel Cano, mi primer guía en el CERN, y demás gente del CIEMAT, J.M.Quesada y R. Capote, A. Mengoni, H. Alvarez-Pol, D. Cortina y J. Benlliure, y sobre todo L. Ferrant, S. Isaev, C. Stephan y L. Tassan-got y demás gente del grupo PACS de Orsay.

Durante cinco años de trabajo los buenos y los menos buenos momentos se han sucedido, siendo los primeros inolvidables y los segundos más llevaderos por culpa de gente como: César, compañero de fatigas y de Foyer, Kike, Carlos, Dani, la gente del experimento CAST, Pino, Pier Francesco y Mauro, Nicola y Stefano, David y Sara ..., que han convertido el CERN en una segunda casa; a mis compañeros de despacho, Jorge, Manolín, Manu, Dani, Noe y Carme, y a Rozas, Hector, Quique y demás gente del grupo GENP de la Universidad de Santiago; a Pichel, Yolanda, Paredes, Diego, y mis amigos pontevedreses, en particular Mar y Jaime por su contribución a la tesis.

Termino dando las gracias a Marga, por estar ahí aguantándome en este último año y medio, y a mi familia, sobre todo a mis padres, por su inquebrantable confianza y apoyo incondicional durante tantos años.

RESUMEN EN CASTELLANO

1. Introducción.

   La creciente demanda de energía ha hecho crecer el interés por el desarrollo de los reactores nucleares de fisión. Tanto si se pretende mejorar el rendimiento de los reactores actualmente en explotación (ciclos del U_{nat} y del Th), como si se busca un procedimiento para la trasmutación de los desechos radiactivos de larga vida media, es necesario disponer de datos más precisos sobre las secciones eficaces de interacción de neutrones sobre los actínidos menores y los productos de fisión de larga vida media.

   Los datos actualmente disponibles en las bases de datos nucleares (ENDF, JENDL, ...) muestran grandes discrepancias y tanto la OCDE-NEA como la IAEA han elaborado una serie de recomendaciones acerca de los datos más relevantes que han de ser medidos dentro de este contexto, entre los que se encuentra el ^{234}U, que es el principal objetivo de este trabajo de tesis.

   El trabajo que se presenta en esta Tesis se refiere a las medidas realizadas dentro de la colaboración n_TOF del CERN, con la finalidad de obtener datos precisos sobre las secciones eficaces de fisión de estos isótopos del uranio, con un haz de neutrones de muy alta resolución en energía, en el rango extendido desde 1 eV hasta 1 GeV.

2. Conceptos básicos de la fisión inducida por neutrones.

   La fisión es un proceso extraordinariamente complejo en el que el comportamiento colectivo de los componentes de un núcleo fuertemente deformado producen la ruptura nuclear en dos núcleos más ligeros de masas comparables, que llamaremos fragmentos de fisión (FF). Estos FF se producen con unas distribuciones de masas y energías cinéticas que son dependientes de la energía del neutrón incidente. También en función de la energía del neutrón incidente, se observa una determinada distribución angular de los FF.

   En el Capítulo 2 de esta memoria se analizan estos conceptos, profundizando únicamente en aquellos puntos que son relevantes para la interpretación de los datos obtenidos en este trabajo.

3. El dispositivo experimental.

El trabajo que ha conducido a esta Tesis doctoral ha sido realizado en las instalaciones del CERN (Ginebra Suiza) denominadas n_TOF. En la Figura 1 se puede ver un esquema de dichas instalaciones. Se ha utilizado un haz pulsado de protones del acelerador PS con una energía 20 GeV/c, una intensidad de 7×10^{12} protones y tiempo de duración del pulso de tan sólo 7 ns r.m.s.
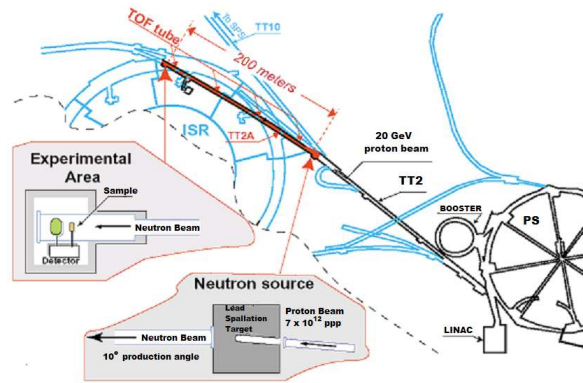

Figura 1: *Vista general de la instalación n_TOF en el CERN.*

El haz de protones incide sobre un blanco de plomo en el que, por espalación, se produce un pulso de neutrones. La principal característica de n_TOF fue la de producir un haz pulsado de alta intensidad de neutrones con un espectro blanco de energías en el rango 1 eV hasta 1 GeV. Su altísima intensidad lo convierte en único en el mundo. El haz, debidamente colimado, se dirige a la zona experimental a lo largo de un tubo de vacío, de unos 185 m de longitud, de forma que los neutrones de mayor energía llegan antes que los que tienen menos. De modo que, mediante la medición del tiempo de vuelo, se puede tener una determinación precisa de la energía de los neutrones que se hacen incidir sobre el blanco, en el que se ha depositado una muestra de los isótopos cuyas secciones eficaces se quieren analizar.

Los detectores utilizados han sido especialmente diseñados y construidos para este experimento. Son detectores gaseosos del tipo PPAC (Parallel Plate Avalanche Counter) [64] cuyas principales características son:
- gran rapidez de la señal y muy reducido tiempo muerto, lo que permite la detección precisa de los fragmentos de fissión en coincidencia, con al-

tas tasas de recuento y un fuerte rechazo del ruido;
- respuesta casi proporcional a la energía depositada, lo que facilita discriminar los pulsos producidos por las partículas alfa de emisión espontánea;
- alta resistencia a la radiación ionizante;
- posibilidad de cubrir grandes superficies de detección a bajo coste;
- poca sección eficaz de interacción con la radiación gamma, lo que permite realizar medidas en tiempos muy cercanos al del pulso inicial, es decir, hasta las máximas energías de los neutrones incidentes;
- la poca masa interpuesta en el flujo de los neutrones permite medir hasta nueve blancos simultáneamente.

El sofisticado sistema de adquisición de datos, basado en convertidores rápidos de analógico a digital (FADC), ha sido específicamente desarrollado para la colaboración n_TOF, aprovechando la gran capacidad de transmisión y almacenamiento de datos, así como la potencia de cálculo disponibles en el CERN.

Los blancos utilizados durante las campañas de medida en las que se ha desarrollado el trabajo de esta tesis, pueden verse en las Tablas 3.1 en la Sección 3.2.

4. La reducción de datos.

   Una parte importante del presente trabajo consiste en la descripción del procedimiento especialmente desarrollado para transformar la información registrada por los detectores que fueron utilizados en n_TOF, para obtener los valores de las tasas de reacción, definidas como las fracciones de los neutrones que inciden sobre las muestras y producen reacciones de fisión.

   Para definir un suceso de fisión se necesita la detección en coincidencia de sus dos fragmentos (ver Figura 4.4 de la memoria). Para ello, tanto los digitalizadores como los distintos electrodos de las PPACs utilizadas, fueron debidamente calibrados para obtener las estrechas resoluciones temporales requeridas.

   En la Figura 4.5 de la memoria se describen los distintos casos de sucesos que pueden obtenerse y, a lo largo de la Seccion 4.2, se describe la metodología empleada para reconstruir los sucesos de fisión con la mayor eficiencia posible.

5. Procedimiento de extracción de las secciones eficaces.

   La determinación de valores absolutos de secciones eficaces es una tarea muy complicada. En nuestra aproximación nos restringimos a producir

medidas relativas, aprovechando el hecho de que podemos poner varios blancos simultáneamente bajo el mismo flujo de neutrones.

Para una superficie unitaria centrada en una posición determinada (x,y), el número de fisiones que nuestro dispositivo experimental detecta, y cada intervalo de energía (E), puede escribirse como:

$$n(x, y, E) = \varphi(x, y, E) \ \rho(x, y) \ \sigma_f(E) \ \varepsilon(E) \tag{1}$$

donde σ_f es la sección eficaz de fisión, φ es el flujo de neutrones por unidad de surperficie y energía, ρ es la densidad superficial de masa (número de núcleos por unidad de superficie) y ε es la eficiencia en la detección de los fragmentos de fisión.

Considerando una superficie unitaria suficientemente pequeña como para poder considerar constantes tanto el flujo de neutrones como la densidad superficial de las muestras depositadas en los blancos, es fácil ver que

$$\frac{\sigma_f^a(E)}{\sigma_f^b(E)} = \frac{n^a(x, y, E)}{n^b(x, y, E)} \ \frac{\rho^b(x, y)}{\rho^a(x, y)} \ \frac{\varepsilon^b(E)}{\varepsilon^a(E)} \tag{2}$$

donde uno de los blancos, usado como referencia, ha de tener una sección eficaz de fisión bien conocida. En este trabajo han sido utilizados ^{235}U y ^{238}U como blancos de referencia.

En la Sección 5.1 se discuten los problemas relacionados con el cálculo de las eficiencias con el dispositivo experimental basado en las PPACs. Más adelante, se discuten los problemas encontrados debido a la anisotropía de la emisión de los fragmentos de fisión, que es un problema que afecta a la eficiencia de detección y que es complicado de corregir. Un resultado de las medidas obtenidas de la anisotropía del ^{238}U se pueden ver en la Figura 2.

En la Figura 5.22 de la memoria se pueden ver los resultados de las eficiencias calculadas para los blancos 0 y 1, ambos con muestras de ^{234}U. Los puntos representan las eficiencias calculadas para cada intervalo de energía, mientras que la curva es la función *spline* obtenida mediante ajuste por mínimos cuadrados. Si se compara con los datos obtenidos en la literatura, se observa que estos no llegan más que hasta 20 MeV.

6. Resultados obtenidos para el ^{234}U.

Las secciones eficaces de fisión del ^{234}U que han sido obtenidas en este trabajo, se muestran en el Capítulo 6, para todo el rango de energías de
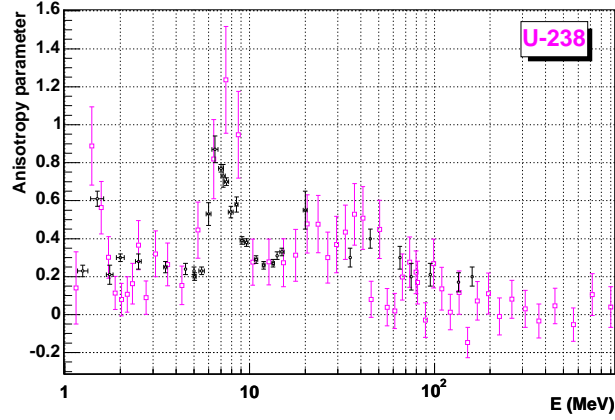
Figura 2: Parametro asociado a la anisotropía obtenido para el ^{238}U. En negro se muestran los resultados obtenidos por otros autores.
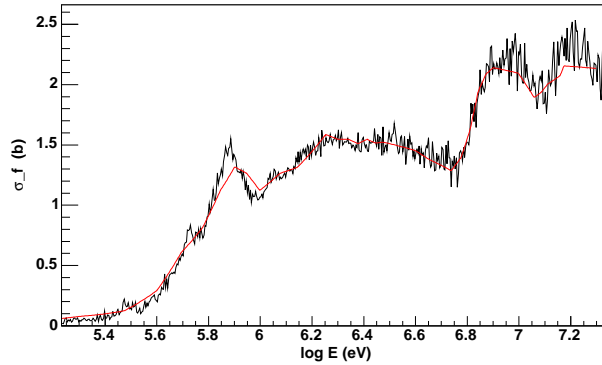

Figura 3: *Sección eficaz de fisin del ^{234}U en el rango de energías entre 200 keV y 20 MeV.*

n_TOF. Las medidas obtenidas son medidas relativas, normalizadas a la evaluación de la ENDF en la región entre 1 y 4 MeV. Como ejemplo, en la Figura 3 representamos los resultados obtenidos para energías por encima del umbral.

En el rango de bajas energías la extraordinaria resolución con la que medimos las resonancias nos invita a llevar a cabo, en un futuro próximo, un nuevo análisis de los parámetros de las resonancias, mejorando los medidos por James et al. [84] en el año 1977.

7. Conclusiones

El objetivo de este trabajo era la medida de la sección eficaz de fisión inducida por neutrones en el rango de energías desde 1 eV hasta cientos de MeV.

Se ha desarrollado un nuevo método adaptado para el tratamiento de los datos obtenidos con los detectores PPAC y utilizando el sistema de adquisición de datos de la instalación n_TOF incluyendo un estudio detallado del comportamiento de los detectores en las particulares condiciones de funcionamiento de la instalación.

Además de la medida de la sección eficaz, también se ha podido dar un valor cualitativo para la anisotropía en la distribución angular de los fragmentos de fisión emitidos en la reacción de fisión.

Con estas medidas se ha probado la aptitud de los detectores PPAC para medir secciones eficaces de núcleos radiactivos hasta energías tan altas como cientos de MeV, según lo cual se está planeando nuevas medidas en la ampliación del proyecto n_TOF que comienza en el año 2006.

Contents

Chapter 1

Introduction

Various sources alert us on the rapidly increasing energy demand for this century, mainly due to the increasing needs in developing countries. Currently, energy production is based on the combustion of fossil fuels (oil, coal and natural gas), hydroelectric power, renewables energies and nuclear fission (Figure 1.1).
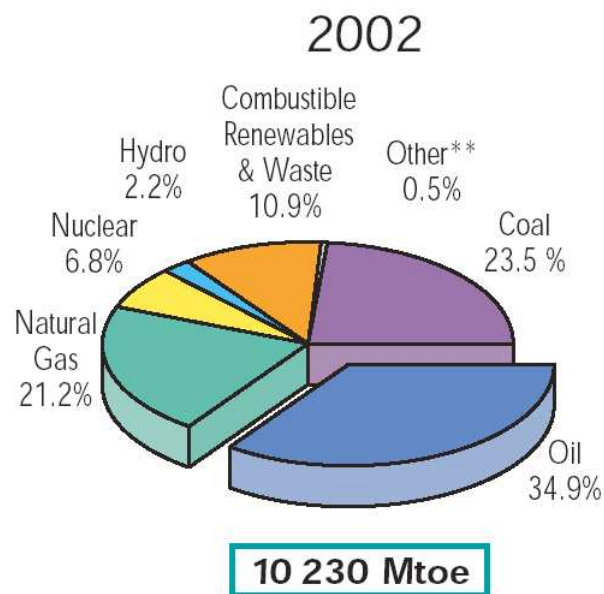

Figure 1.1: *Fuel Shares of the World Total Primary Energy (TPE) in 2002. Total energy values are supplied in Million Ton Oil Equivalents (Mtoe) [1]. Others includes geothermal, solar, wind, heat, etc.*

Roughly speaking, three fourths of the world's energy is produced by combustion of fossil fuels. The corresponding release of CO_2 into the atmosphere is the main cause of the greenhouse effect, resulting in global warming and the urgent need to reduce the amount of combustion emissions. Moreover, fossil fuels are non-renewable and, at current consumption levels, oil reserves are estimated to last about 40 years, gas reserves 60 years and coal reserves 200 years [2].

Renewable energy sources, such as solar and wind energies, are intermittent and less able to compete at the level of the high-power national networks. Nevertheless, with the present technological development, they can be considered as a mid-term option to replace a percentage of the traditional production (likely up to 20% by 2020).

Hydraulic resources are almost fully harnessed in developed countries and big dams have huge environmental and social implications. Therefore, only 10 % growth is expected for the mid-term.

At this point, we should consider the role of nuclear energy for the future [3]. At present, nuclear energy provides less than 10 % of total world's energy production, and there are several constraints to its large-scale development.

In what concerns safety, the so-called standard nuclear reactors, that are currently in use, function in the critical mode which means that the chain reaction is supported by one and only one of the neutrons released in the fission reaction [4]. If more than one released neutron causes a fission the reactor becomes *supercritical* (diverges): the amount of released energy increases and the temperature elevation can lead to a major nuclear accident. To avoid this, the security standards for nuclear reactors require that an increase in temperature must be automatically compensated by a decreasing number of fissions. This is referred to as passive safety.

Standard reactors generate energy from the fission of ^{235}U. Taking into account that the uranium isotopic composition is 99.3 % ^{238}U and 0.7 % ^{235}U, with traces of ^{234}U, only a small fraction of the natural uranium is converted into energy in these reactors. Moreover, the world supply of uranium ore is limited, so it must be considered too as a non-renewable energy source. Excluding fuel recycling or regeneration, "economical" uranium resources[1] are estimated to last several hundred years at current consumption rates. However, if the share of nuclear energy in the world's energy consumption were to increase significantly, these resources could be spent in a much shorter time.

Finally, the highly radioactive wastes generated during power production

---

[1]If extracting uranium from seawater becomes economical, uranium reserves could be practically unlimited

are the greatest challenge to the use of nuclear energy. They include long-lived radioactive elements like Plutonium, minor actinides or fission fragments, that must be isolated from biological systems for the time of their active life, which can be of the order of millions of years.

Nuclear waste storage in deep geological sites seems to be an effective procedure, but might prove insufficient if the wastes produced were constantly increasing. For this reason, waste transmutation should be considered as part of the solution. Transmutation can be defined as the process of converting one element into another. In the context of conditioning the constituents of the spent fuel, transmutation converts plutonium and other actinides and long-lived fission isotopes into isotopes with more favourable characteristics.

Several interesting proposals have been made in an attempt to resolve issues related to energy production by means of innovative nuclear technologies (Generation IV International Forum [5]). One of them is the Accelerator Driven System (ADS) concept, consisting of a sub-critical reactor operating with fast or thermal neutrons supplied by an external source such as a proton accelerator [6–8]. There are several advantages related to this kind of reactor:

- It operates in a sub-critical mode which reduces the risk of a diverging reactor behaviour. The neutrons required to sustain the chain reaction are produced by an accelerator that needs only to be turned off to stop the reactor immediately. This type of reactor is far more secure than the standard ones because efficient passive security devices can be built, such as automatic accelerator shutdown at the first sign of abnormal temperature rise, provided the criticity of the core is well probed.

- Thorium, in addition to uranium, can be used as nuclear fuel. ^{232}Th together with ^{238}U are the fertile elements existing in nature. In the thorium-uranium (Th-U) cycle, shown in the Figure 1.2, the fissile element ^{233}U is regenerated by the ^{232}Th$(n,\gamma)^{233}$Th$(\beta)^{233}$Pa$(\beta)^{233}$U process. Thorium has only one isotope, ^{232}Th, so his use is more efficient, and its abundance in the earth's crust is about three times that of uranium [9].

- Nuclear waste transmutation. Plutonium and minor actinides can be *incinerated* in an ADS. By placing them in the neutron flux for long periods they can be eliminated and their fission also produces energy. The resulting fission products are the same as in a standard reactor: some of them are radioactive with a long half life, and consequently need long-term storage. However, destroying existing stocks of plutonium and
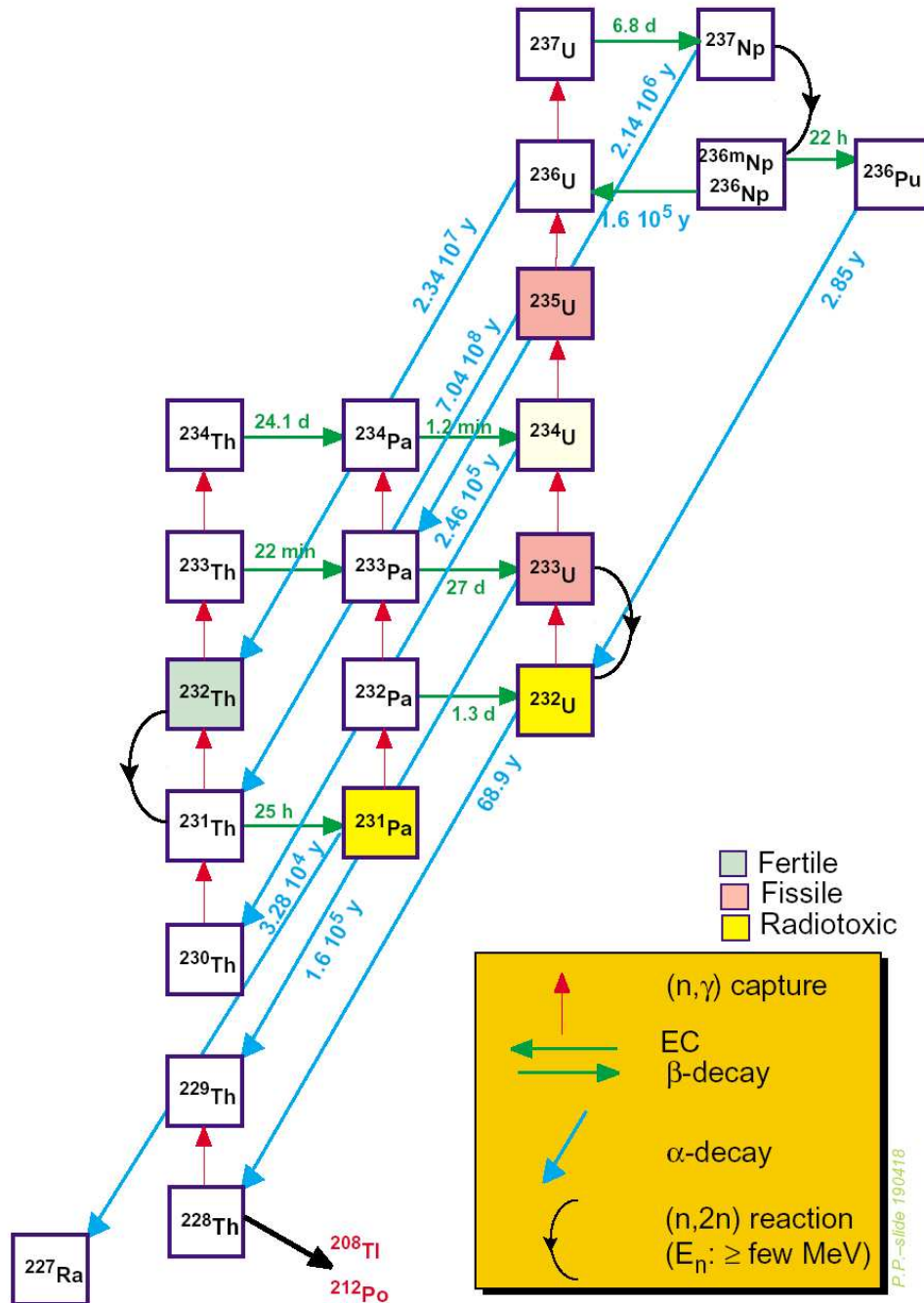
Figure 1.2: *Schematic view of the thorium-uranium cycle.*

minor actinides reduces significantly the volume of nuclear wastes that require long-term storage. Simulations done with the thorium-uranium cycle also show that the production of minor actinides is two or three orders of magnitude smaller than the uranium-plutonium cycle [10].

In the design of an ADS prototype, Monte Carlo techniques are used to predict its performance in different configurations and running conditions. These Monte Carlo simulations require an accurate knowledge of involved nuclear reaction data, in particular **neutron cross-section** data, because the quality of a simulation depends on the quality of the data used as input. Unfortunately, severe deficiencies and differences exist in the compilation databases currently available, which are generally based on different experimental measurements and existing theoretical models. Higher fuel burn-up and especially waste incineration options require new and better data on minor actinides and long-lived fission products. Better data are also needed for developing the structural components of the ADS.

In addition, these data also have significant implications for basic and applied research in other fields, such as astrophysics, fundamental nuclear physics and dosimetry.

1.1 Nuclear data for the Th-U cycle isotopes

The neutron data libraries presently in use are derived from evaluations based on experimental data or from nuclear models which are used where experimental data are lacking or inconsistent [11, 12]. The availability of complete evaluations with high accuracy and energy resolution influences the reliability of both design and safety studies in nuclear energy. Some of the evaluations currently available in the nuclear databases fall well below the required standards.

The International Atomic Energy Agency (IAEA) Nuclear Data Center (Vienna) recommendations [13] for improving the available nuclear data information include the isotopes relevant to the Th-U cycle, specifically ^{232}Th, ^{231,233}Pa, and ^{232,233,234,236}U, among the first priority isotopes. Of these seven isotopes, ^{233}Pa and ^{232}U are not easily accessible for experimental measurements due to their high specific activity, which limits their availability with the sufficient purity and makes transportation difficult.

In addition to their interest for the present nuclear technology, the fission cross sections of these isotopes generate important information on nuclear

structure due to their specific nucleonic composition; providing a very complex and well-defined fine structure for the potential surface energy around the fission barrier. The neutron induced fission process can be understood by introducing a double-humped fission barrier (DHB) [14, 15] (see Subsection 2.1), which is in good agreement with both the experimental data and theoretical predictions for light and heavy actinides. However, for some light actinides such as ^{232}Th and ^{234}U, the calculated first saddle and second minimum of the double-humped potential barrier are several MeV lower than the experimental values commonly attributed [16]. This discrepancy is referred to as the "thorium anomaly" in the fission literature [17]. In particular, experimental results on the nuclei ^{230}Th and ^{232}Th indicate a dominant additional barrier, resulting in the creation of a shallow third well, roughly 1 MeV deep, just deep enough to accommodate some very deformed metastable states. This effect suggests the existence of the so-called triple-humped fission barrier (THB) [18], which was predicted by Aage Bohr in 1955. The study of the vibrational resonance structures in these anomalous nuclei could directly confirm the existence of the THB and shed some light on the question of the thorium anomaly, which remains unresolved since the first half of the seventies.

The nuclear data for the Th-U cycle nuclides were evaluated in the early seventies and mid-eighties and do not fulfil the current accuracy requirements. There are large discrepancies between the evaluated neutron data files JENDL-3.3[2] and ENDF/B-VI[3] released by the IAEA Nuclear Data Service. One of the striking discrepancies is that the resolved and unresolved resonance regions are different for most isotopes. The cross-section shapes in the epithermal and resolved resonance regions also differ significantly for all these isotopes. A critical analysis of these two nuclear data files indicates that experimental data are incomplete or even missing in many cases and the evaluated cross sections rely heavily on theoretical models and nuclear systematics.

This work will focus on the neutron-induced fission cross section of the ^{234}U isotope. In the Th-U cycle, the ^{234}U is formed by neutron capture in ^{233}U, as well as by capture in ^{233}Pa and beta decay of the ^{234}Pa (see Figure 1.2). In thorium reactors, the formation of ^{235}U by neutron capture in ^{234}U helps to reduce the burn-up swing in long-lived cores. The ^{234}U plays a role in thorium fuel cycle similar that of the ^{240}Pu isotope in the U-Pu fuel cycle. Since ^{234}U also is formed by (n,2n) reactions in ^{235}U, it is a common isotope to both fuel cycles.

---

[2]Japanese Evaluated Nuclear Data Library
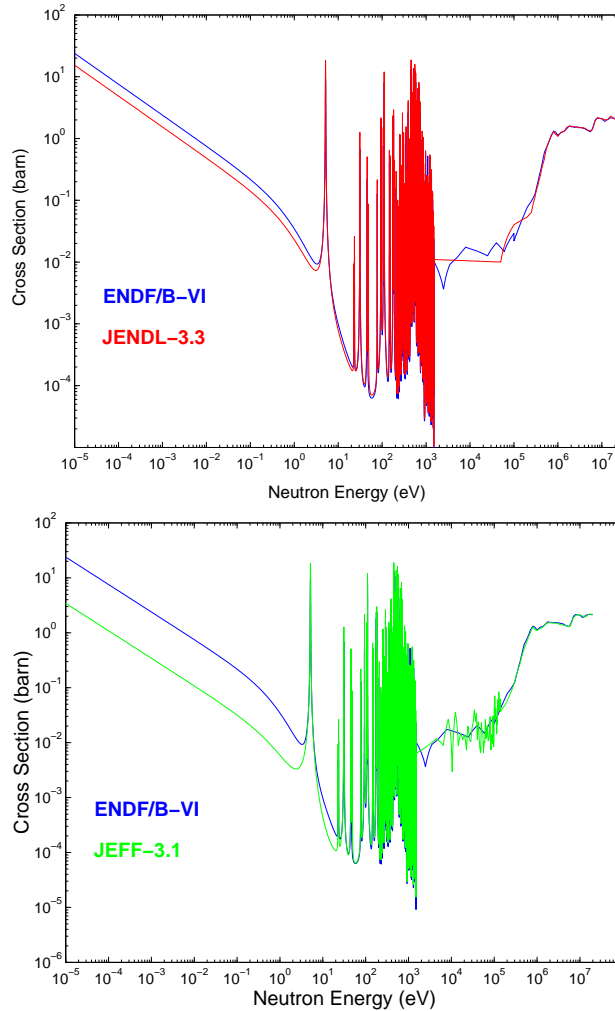[3]American Evaluated Nuclear Data Library

Figure 1.3: *Comparison of ^{234}U fission cross section as a function of the neutron energy for the currently available evaluations (ENDF/B-VI,JENDL-3.3,JEFF-3.1[4])*

For ^{234}U fission cross section the unresolved resonance region extends up to 100 keV in ENDF/B-VI/R5 as compared to 50 keV in JENDL-3.3. Additionally, in the 1-10 MeV region, both fission cross sections are within a 5 % band (Figure 1.3), whereas the accuracy required for this isotope should be lower than 3 %.

---

[4]Joint Evaluated Fission and Fusion Library, created by the Nuclear Energy Agency.

Motivated by the related issues, the Joint CERN-EC-GEDEON-OECD/NEA Workshop was organised at CERN (European Organization for Nuclear Research) in September 1998, inviting many interested experimental groups from almost all European countries to elaborate a physics programme to investigate the opportunities offered by the proposal of a new Neutron Time of Flight Facility at CERN (n_TOF) [19, 20]. These groups started the "European n_TOF Collaboration", establishing the main research lines that were presented in March 1999 in the proposal "European Collaboration for High-Resolution Measurements of Neutron Cross Section between 1 eV and 250 MeV".

The idea for the Neutron n_TOF facility was to take advantage of the high intensity proton accelerator PS at CERN to obtain an intense neutron source by spallation mechanisms. This neutron yield determines the accessible path length and thus the energy resolution obtained by means of neutron time of flight techniques. The construction and commissioning of the neutron beam line was finished in April 2001 and since then an important set of differential cross-sections measurements has been completed, which includes those described in this work.

This thesis work has been performed within the framework of the n_TOF-ND-ADS project. The layout of this thesis memory is as follows:

Chapter 2 provides a brief introduction to some fission concepts related to this work. The main characteristics of the n_TOF facility together with the experimental setup employed in the measurements are explained in Chapter 3.

The data reduction process for the fission detectors is described in Chapter 4, while the procedure implemented to determine the cross sections is explained in Chapter 5. Chapter 6 is a discussion about the results of the ^{234}U(n,f) cross section, the main aim of this work.

Finally, the most relevant contributions of this thesis are highlighted in the Conclusions.

Chapter 2

Neutron-induced fission backgrounds

In the quest for a deeper understanding of the nuclear fission process, neutron-induced fission has always played the most important role. Hahn and Strassmann actually discovered fission while investigating the reaction products of uranium irradiated with neutrons [21]. Many of the physically interesting detailed phenomena of nuclear fission were also found in later studies on neutron-induced fission. However, fission induced by neutrons cannot be separated from the general nuclear fission process. Nuclear fission is an extremely complex collective process in which a highly-deformed heavy nucleus undergoes a deep rearrangement, breaking into two fragments of comparable masses.

An extensive description of the fission reaction and review of the many experimental and theoretical works in this field is well outside the scope of this work, which is the measurement of fission cross sections. Here only a brief summary of those features relevant to this work will be presented, focusing mainly in the physical parameters of the fission products from which we identify the fission events. For an extended review, the lectures of the Vandenbosch [22] and Wagemans [23] books provide a thorough description of developments in this field.

2.1 The fission process

Fission is generally treated as a collective phenomenon according to the liquid drop model (LDM) [4, 24]. The analogy with a charged drop of liquid is not only helpful analytically, but also provides a useful image of the process. The liquid drop model predicts spherical shapes for the ground states of stable

nuclei and the "fission barrier" (see Figure 2.1). Inside this model spontaneous fission can occur via quantum mechanical tunneling through the fission barrier.
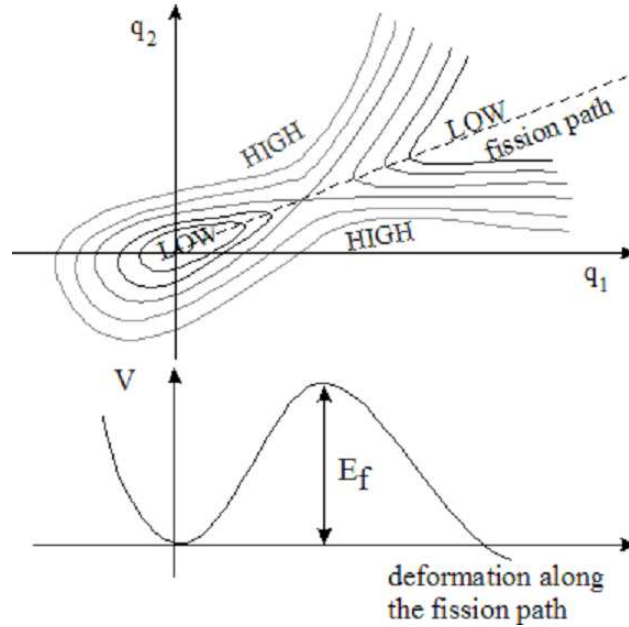

Figure 2.1: *Schematic picture of potential energy contours as a function of deformation parameters [14] (top). The fissioning system shape modifies continuously during the motion from the formation of the initial state to the elongated pre-scission shape. The fission path (dashed line) corresponds to the lowest potential energy when increasing deformation. The one-dimensional representation of the potential energy along the fission path (bottom figure) shows the referred fission barrier.*

In spite of the first successes in the fission process description, the LDM cannot explain some basic properties of the actinides: their non-spherical ground states and their asymmetric mass division (see Figure 2.7). It is necessary to introduce the shell effect in the fission process explanation.

The nuclear shell model [25] was developed in analogy to the atomic shell model. The mutual interaction between the nucleons is described by an average potential, the shell model potential, consisting of a central potential and a spin-orbit interaction, and the nucleons are assumed to move independently in this potential. The shell model accounts for the fission fragment asymmetry by means of the concept of closed nucleon shells and "magic numbers".

However, the most drastic effect of shell structure occurs in the fission barrier itself. As we begin to stretch the nucleus (characterized by an eccentricity
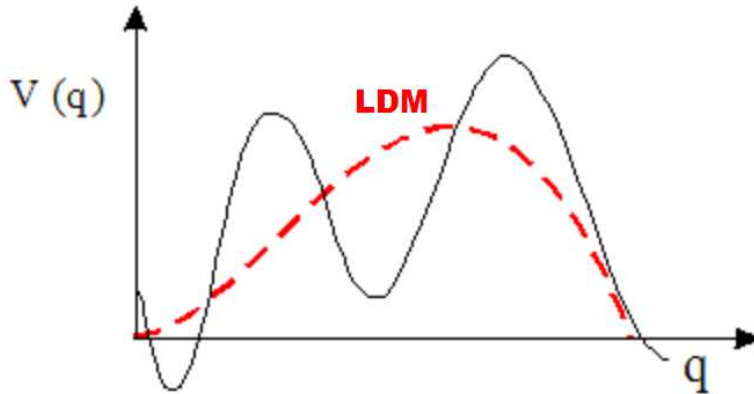
Figure 2.2: *Schematic picture of the fission barrier of a typical actinide nucleus. The dashed line shows the single barrier predicted by the LDM, while the solid line includes the corrections due to shell structure.*

parameter q), the potential energy increases like q^2, giving an approximate parabolic dependence. The now deformed nucleus is modelised by the few nucleons out of the spherical symmetry, which are called valence nucleons. The single-particle states [26] in the now deformed nucleus vary with deformation and their enery increases or decreases depending on the state. If the valence nucleons are in a state that happens to have $V(q)$ with positive slope, the net increase in energy with deformation will be faster than the parabola. At some point, however, increasing q a cross-point with a negative slope state is reached and the valence nucleon now follows the new state, with lowest energy, being now the net change in energy below the parabola. It remains so until a new crossing with a state whose energy increases with q. This oscillation due to the changing behaviour of the valence particles with q is shown in Figure 2.2. At the point where fission begins to occur, the form of the single barrier becomes modified and the energy dependence introduced by the single-particle shell structure results in a fission barrier with two humps. The net effect for a nucleus being excited above the bottom of the second well, is that penetration of the two thinner barriers becomes more probable and fission can occur.

The introduction of the double-humped barrier was necessary to explain the *fission isomers* or *shape isomers*, isomeric excited states with unusually short half-lives for spontaneous fission discovered in 1962 [27]. It was postu-

lated that these isomers were actually states in an intermediate potential well
and could decay either by fission through a relatively thin barrier, or by γ
emission back to the ground state (see Figure 2.3). This explanation of the
fission isomers was confirmed by measurements of the rotational spectra of the
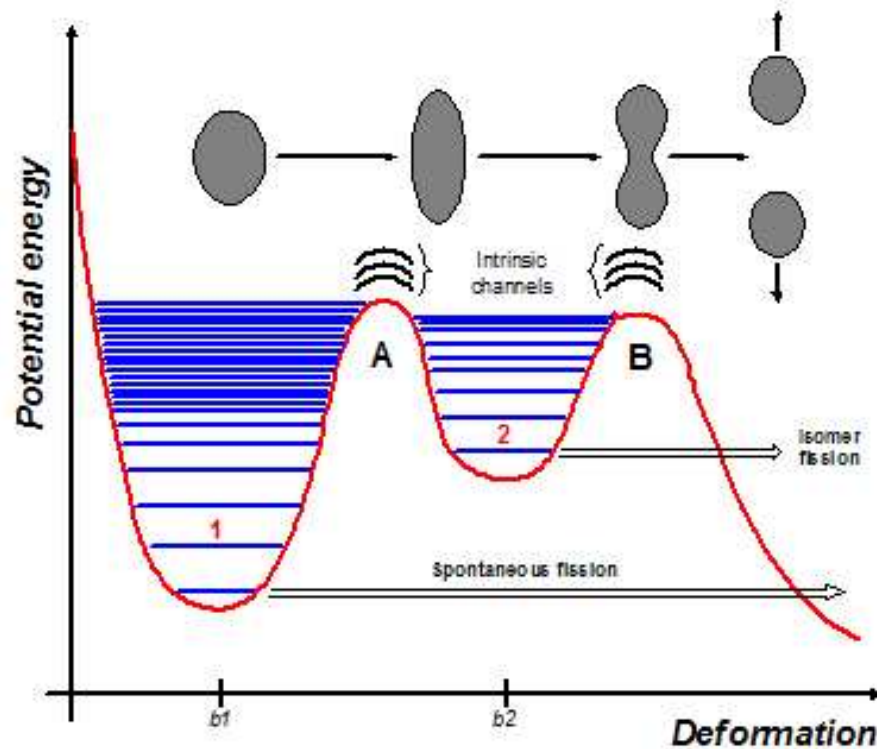excited states in the second potential well.

Figure 2.3: *The double-humped fission barrier can explain the existence
of short-live fission isomers. The penetrability of the second hump of the
barrier is greater that of the whole barrier. The nuclear states in the first
and the second well are referred to as class I and class II states, while
the states in the top of the barriers are the intrinsic or transition states.*

Another influence of the second potential well is on the structure of the
resonances in fission cross section. There are many individual fission reso-
nances in the eV-keV region and we can consider these resonances as originated
from excited states in the first potential well. In any nucleus, at an excitation
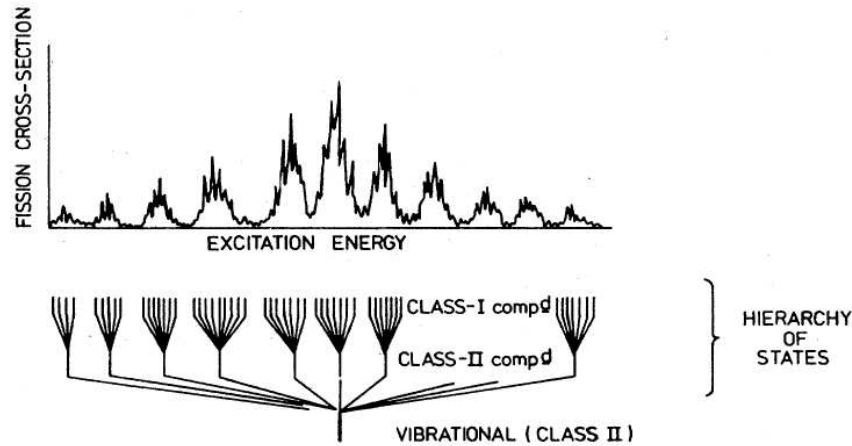of 6 MeV following neutron capture, the average level spacing is of the order

Figure 2.4: *The clustered resonance structure is expalined by the class I and class II states coupling. [14]*

of eV. Not all of these excited compound states following neutron capture are likely to fission and fission resonances are clustered in well-separated groups. This effect occurs because the second well is not quite as deep as the first. The density of the states of any nucleus depends on the excitation energy above the ground state – the higher we go above the ground state, the closer together are the states. States in the second well at the same energy as those in the first well are, on the average, further apart. Another difference is that states in the second well have a higher probability to fission, because they must penetrate only one barrier and thus a greater width than the states in the first well. This means that the fissioning states are selected through the overlap in energy between the narrow, closely spaced states in the first well and the broader, more widely spaced states in the second well. The effect is also translated to the cross section and gives rise to resonance structures as shown in Figure 2.4.

To close this preamble, it is worth to point out the strong dependence of the fission cross section on the nucleon pairing. Considering the uranium isotopes, the odd-A nuclei can fission with thermal neutrons while even-even nuclei present a fission threshold in the MeV region. For nuclei like the ^{235}U, cross section is characterised by a $1/v$ dependence in the thermal region and a very complex resonance structure (see Figure 2.5). At this energy region, fission cross section dominates over scattering and radiative capture and is three orders of magnitude larger than the cross section for fast neutrons. On

the other hand, ^{238}U requires more energy to fission than ^{235}U because of the energetics of the pairing term and so it will only fission with fast neutrons.
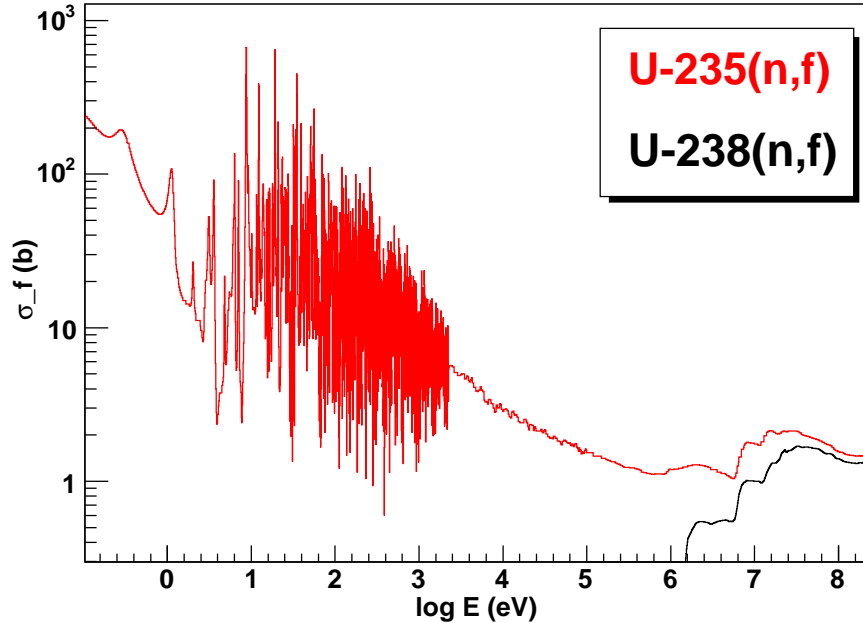

Figure 2.5: *Cross sections of the neutron-induced fission of ^{235}U and ^{238}U – isotopes used as standard references. Cross sections correspond to the probabilities for a given process, in this case fission, and are customarily expressed in units of barn ($1b = 10^{-24}cm^2$).*

2.2   Characteristics of fission fragments

Nuclear fission consists in the nucleus division into two fragments of comparable nuclei mass (primary fission fragments) and not uniquely determined. Neutron-induced fission events are described by their mass numbers (A_i), their charge numbers (Z_i) and their kinetic energies, and also their emission angles with respect to the beam axis must be known.

One or more neutrons are evaporated from the fissioning nucleus or from the excited fragments in times less than 10^{-15} s, which means that the nuclei actually detected in experiments are not the primary fragments, but secon-

dary fragments that have lost a varying number of neutrons. Nevertheless, it is important to note that both the energy and the angular momentum carried out by the evaporated neutrons is only a small fraction of those of the fragments.

Just mentioning that ternary fission processes are considered to have a low yield $(< 2\%)$ [28].

2.2.1   Mass distribution of the fission fragments

We have already mentioned that the nuclei produced by fission are called fission fragments (FF) and that they are not uniquely determined – there is a distribution of masses of the two fragments.
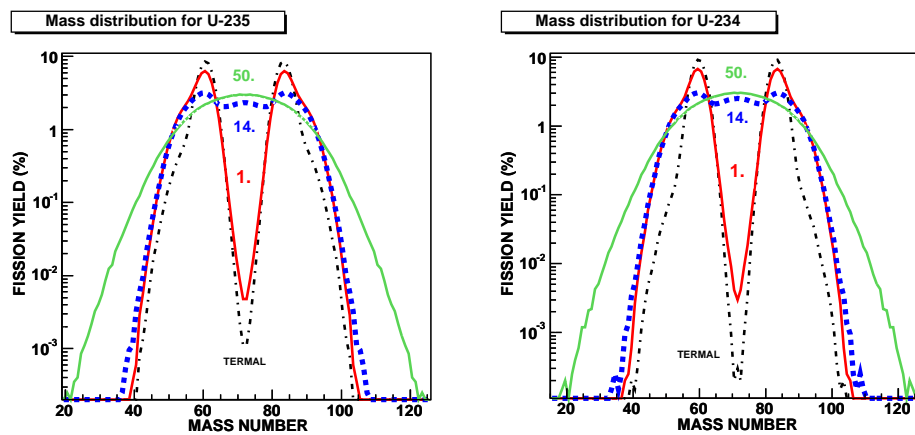

Figure 2.6: *Neutron mass yields for ^{235}U and ^{234}U vs. mass number. The energies of neutrons inducing fission are indicated in MeV by labels attached to the curves.*

Although a large amount of experimental data on the mass distribution has been available for a long time [29,30], no suitable theory yet exists that can account for all the observations. It is well-known from experiments that the mass distribution for a particular system changes with the excitation energy and that the mass distribution depends on the mass number A of the fissioning system. A mass distribution is said to be *symmetric* whenever the fragment yield peaks at $A_F/2$, that is, at half the mass number A_F of the fissioning nucleus. For *asymmetric* fission the highest yields are attained for two different but complementary fragment mass numbers, the sum being the mass of the fissioning nucleus A_F. In other words, the yield $Y(A)$ as a function of the fragment mass A is a single-humped or double-humped curve in case of symmetric or asymmetric fission, respectively. The mass yield curves obtained

by means of an advanced statistical saddle-scission model [31] for the fission of ^{235}U and ^{234}U for incident neutron energies ranging from thermal energies to 50 MeV are shown in Figure 2.6. The yield close to mass symmetry increases by more than two orders of magnitude when increasing the energy. Similar results are obtained for the isotope ^{239}Pu - thermally fissile- and the ^{238}U - thermally nonfissile. The only target nucleus from the minor actinides that exhibits a noteworthy peculiarity is the thorium [32].

When referring to asymmetric fission, the two humps corresponding to larger and smaller A values will be referred to as heavy and light groups, respectively.

As we observe the mass distributions for neutron-induced fission of several nuclei, another interesting feature appears. The average mass number of the heavy group is approximately constant, whereas the same quantity for the light group varies to account for the total mass of the fissioning system (Figure 2.7). The nearly constant position of the light side of the heavy group has been observed for a large number of fissioning nuclei and it is attributed to shell effects in the heavy fragment.

2.2.2   Average kinetic energies

The total kinetic energy and its distribution between the fragments is correlated to the mass distribution. Fission is one of the most energetic reactions, with typical Q-values of around 200 MeV in the actinides, averaging over all fragmentations. Shortly after scission, this energy is shared between the kinetic and the excitation energies of the fission fragments. The total kinetic energy release, E_k is the sum of the light and heavy fragment kinetic energies, E_{KL} and E_{KH}, respectively. Taking the uranium isotopes as an example, the total kinetic energy is roughly $E_k \approx 170 MeV$, which means that the largest share of the total energy goes into the kinetic energy of the fragments. The remaining energy, staying with the fragments as excitation energy, is ultimately released by neutron and gamma emission and subsequently by radioactivity.

The high average kinetic energy of the fragments can be explained by the high repulsive Coulomb force between the two nascent fragments upon splitting a charged liquid drop. This intuitive picture is corroborated by the systematic increase of the mean kinetic energy with the Coulomb parameter $Z^2/A^{1/3}$ of the fissioning nucleus. A comprehensive set of E_K data for a broad range of fissioning nuclei and fission reactions was analyzed by Viola [35], achieving the following correlation between the kinetic energy release and the
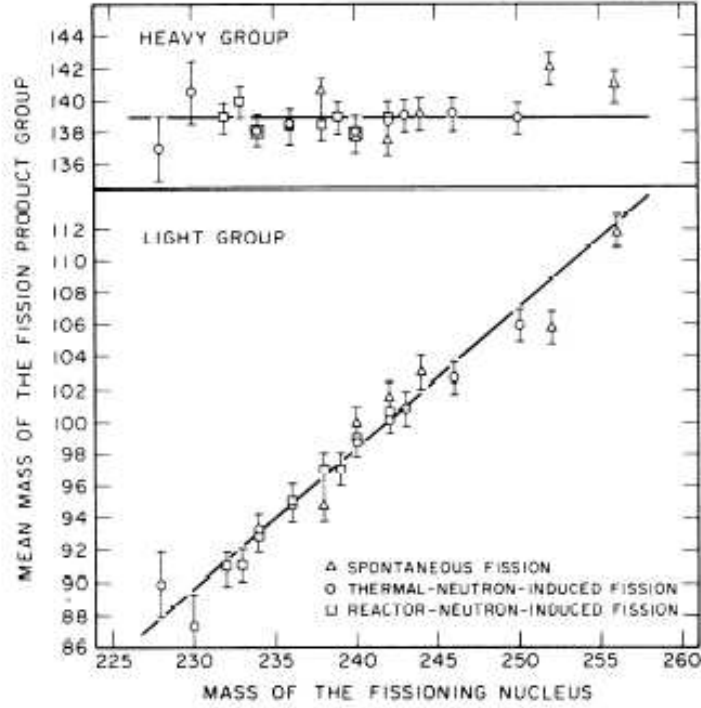
Figure 2.7: *The average masses of the light and heavy fission product groups as a function of the masses of the fissioning nucleus. This illustration shows that the heavy group mass remains approximately fixed, while the light group mass increases linearly with the mass of the fissioning nucleus [36].*

Coulomb parameter:

$$< E_K^* > = (0.1189 \pm 0.0011)Z^2/A^{1/3} + 7.3(\pm 1.5)MeV \qquad (2.1)$$

Figure 2.8 reproduces the kinetic energy distribution of a single fragment. In asymmetric fission a larger fraction of the available energy will be imparted to the light fragment than to the heavy one due to momentum conservation. Neglecting the momentum from the incident neutron and that carried by the evaporated neutrons, the two fragments have nearly equal and opposite momenta, so that the ratio between the kinetic energies should be the inverse of the ratio of the masses:

$$\frac{\frac{1}{2}A_L v_L^2}{\frac{1}{2}A_H v_H^2} = \frac{A_H}{A_L} \qquad (2.2)$$
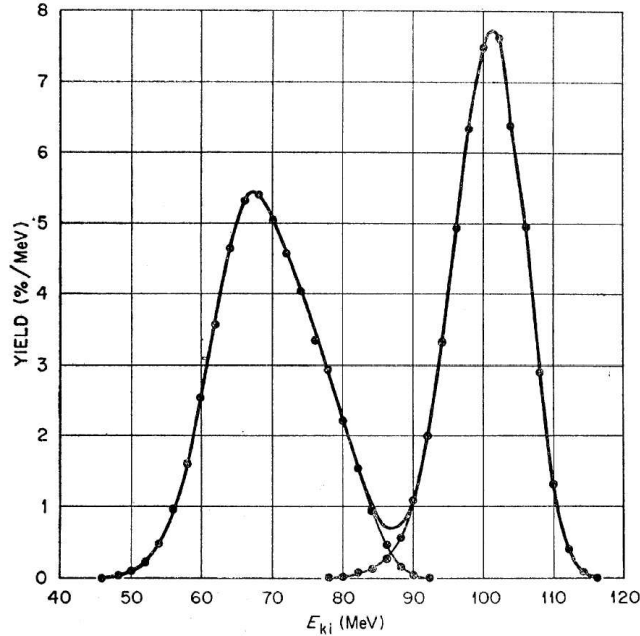
Figure 2.8: Energy spectrum of ^{233}U fission fragments for thermal neutrons [37].

Accordingly, the higher peak in Figure 2.8 traces the energy distribution of the light fragments, whereas the lower energy peak corresponds to the heavy fragments.

Besides the kinetic energy, the velocity of fission fragments can be easily calculated by the time-of-flight technique. The velocity of fission fragments is typically about 1 cm/ns, i.e., 3 % of the speed of light, which confirms the suitability of the non-relativistic approach in Equation 2.2.

2.2.3   Fission fragment angular distribution

The transition nucleus concept was first applied by A. Bohr [33] (1956) to explain fission-fragment angular distributions. The theory postulates that the fission fragments separate along the nuclear symmetry axis, and that the component of the total angular momentum along the nuclear symmetry axis, K, is a good quantum number beyond the saddle point of the fission process. Based on these assumptions the angular distributions of fission fragments is uniquely defined by the rotational wave function [22]:

$$W_{M,K}^J(\theta) = [(2J+1)/2]|d_{M,K}^J(\theta)|^2 \tag{2.3}$$

where J represents the total angular momentum, K is the projection of J on the nuclear-symmetry axis, and M is the projection of J on a space-fixed axis. The angle θ represents the angle between the nuclear symmetry axis and the space-fixed axis, which is usually taken as the beam direction for induced fission. The $d_{M,K}^J(\theta)$ functions are defined by the following relation

$$d_{M,K}^J(\theta) = \{(J+M)!(J-M)!(J+K)!(J-K)!\}^{1/2}$$
$$\times \sum_X \frac{(-1)^X[sin(\theta/2)]^{K-M+2X}[cos(\theta/2)]^{2J-K+M-2X}}{(J-K-X)!(J+M-X)!(X+K-M)!X!} \tag{2.4}$$

where the sum is over $X = 0, 1, 2, 3, ...$ and contains all terms in which no negative value appears in the denominator for any of the quantities in parentheses.

As long as the transition nucleus is "cold" enough, the fission process occurs through a few transition states (channels) with specific quantum numbers. Some typical $W_{M,K}^J(\theta)$ functions are plotted in Figure 2.9.

Low-energy neutron-induced fission of even-even nuclei with fission thresholds exceeding the neutron binding energy (such as ^{234}U) offers a good opportunity for characterising the transition state spectrum, since only a few states in the transition nucleus will be accessible (Figure 2.10).

In the case of target nuclei with odd neutron number (an odd-N target) the basic difference is the larger neutron binding energy. Hence, even the capture of a thermal neutron leads to an excitation energy in the compound nucleus which is considerably greater than the lowest fission barrier for the even-even transition nucleus. For this reason, most of the analyses of angular distribution data for fission induced by neutron capture of odd-N targets have been performed with the assumption of a Gaussian K distribution.

When the excitation energy increases, a continuum set of transition states comes into play. Statistical consideration in conjunction with a Fermi gas model predicts the K distribution to be Gaussian. The square of the standard deviation of the Gaussian, K_0^2, is related to both the temperature T above the barrier and to the effective moment of inertia at the saddle point $\Im_{eff}$. The $\Im_{eff}$ is defined as $\Im_{eff} = \Im_\perp \Im_\parallel / (\Im_\perp - \Im_\parallel)$, where $\Im_\perp$ and $\Im_\parallel$ are the moments of inertia about axes perpendicular and parallel to the symmetry axis, respectively. The excitation energy is related to the nuclear temperature by a state equation $U = a_f T^2$, where a_f is the level density parameter. If $\Im_{eff}$ is assumed to be independent of the excitation energy, then K_0^2 shows a square-root dependence upon U.
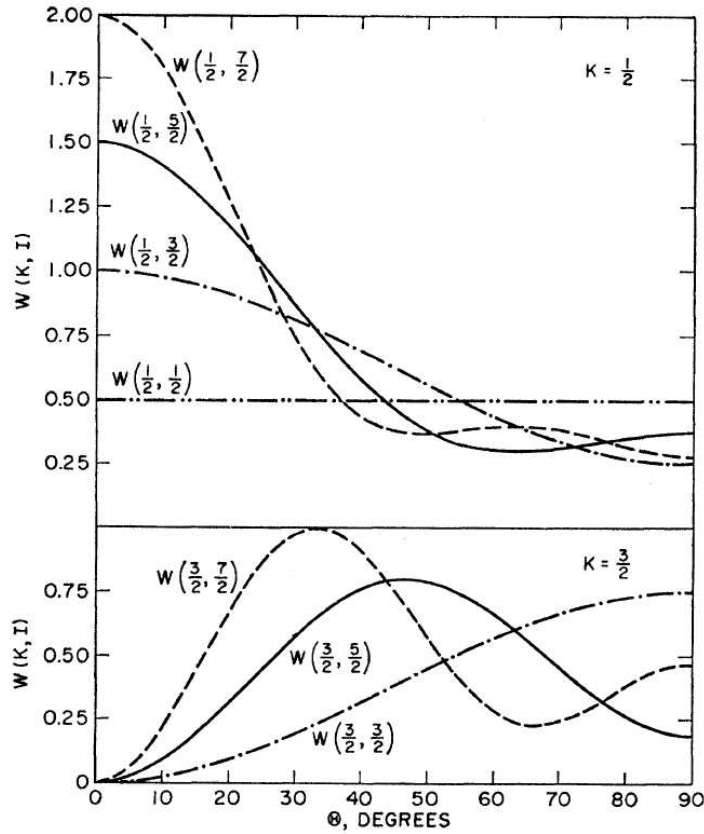
Figure 2.9: *Theoretical fission-fragment angular distributions for neutron-induced fission of even-even target nuclei [34]. The axis of quantization is along the beam direction and M has values of $\pm\frac{1}{2}$.*

For a fission reaction induced by energetic neutrons the fragment angular distribution is always the sum of the angular distributions of the contributing fissioning species, which come about from the multi-chance fission preceded by direct and pre-equilibrium reactions. Experimental and theoretical fission fragment angular distributions are generally compared in terms of the anisotropy ($A = W(0°)/W(90°)$). Unlike the total fission cross section, the anisotropy is more sensitive to the chance structure of the fission process because the contribution of the high chances (low excitation energies) is enhanced by the factor $W_{M,K}^{J}(\theta)$, which increases greatly with decreasing excitation energy.

For small angular momentum I introduced by the projectile ($\frac{I^2}{4K^2} << 1$),

the anisotropy can be written as

$$\frac{W(0°)}{W(90°)} \simeq 1 + \frac{I^2}{4K_0^2} \qquad (2.5)$$

Angular distributions have been studied in the excitation region up to several tens of MeV for many targets and for a variety of projectiles, including neutrons, protons, deuterons, α particles and heavy ions. The most interesting features of the experimental observations can be summarized in the following statements:

- Fission fragments have usually the largest differential cross sections in the forward and backward directions along the beam.

- Anisotropies are largest for the heaviest projectiles and smallest for neutron and proton bombardments.

- Anisotropy increases whenever a threshold is reached, where it becomes energetically possible for fission to occur in the residual nucleus that is left behind after the evaporation of some definite number of neutrons.

- Anisotropies for high projectile energies are approximately the same for odd-A targets as for even-even targets.

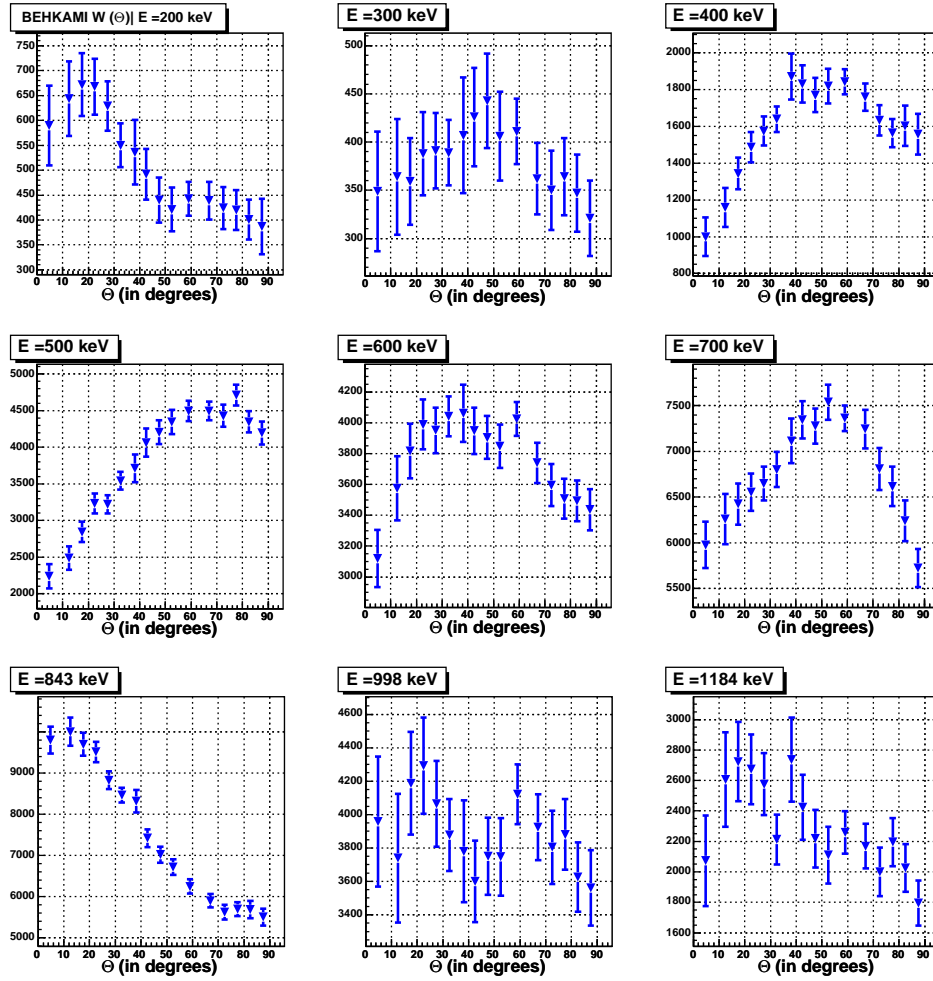- Anisotropy decreases as the Z^2/A value of the target increases.

Figure 2.10: *Fission fragment angular distributions for the $U^{234}(n,f)$ reaction at several incident neutron energies extracted from Behkami et al. [34].*

Chapter 3

Experimental setup

The purpose of this chapter is to introduce the experimental setup used at the n_TOF facility [19, 39–42] (CERN) to measure neutron-induced fission cross sections. The main characteristics of the n_TOF facility, the PPAC detection setup and the data acquisition system will be described, in particular those aspects relevant to our data analysis.
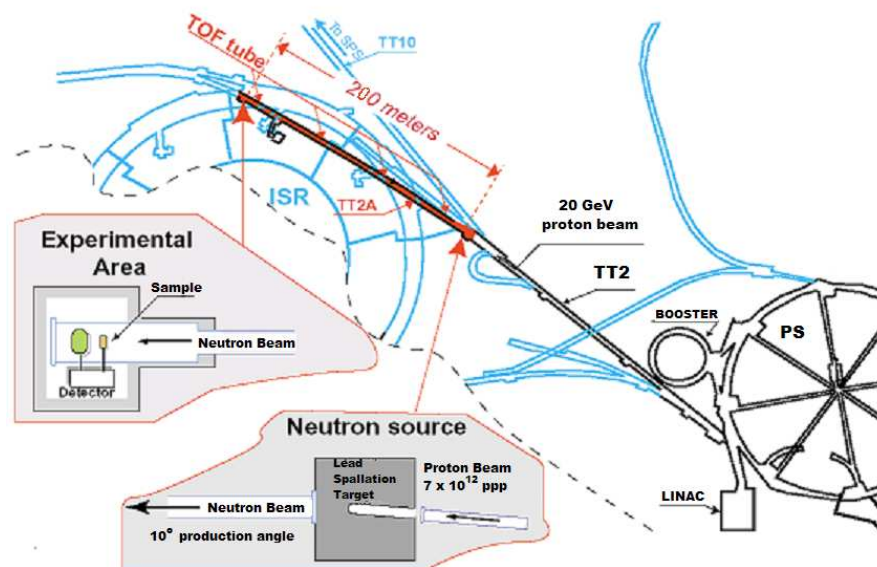

Figure 3.1: *General layout of the n_TOF facility.*

3.1 Description of the n_TOF facility

The main motivation of the n_TOF facility (Figure 3.1) was the need for accurate neutron cross sections, with a view to develop new concepts for nuclear reactors. The measurements carried out at the n_TOF facility can be divided in two areas: radiative capture and fission. This work will focus on the specific features of the fission experiments.

3.1.1 The PS beam

The proton beam is supplied by the CERN Proton Synchrotron (PS) and carried up to the Spallation Target through a transfer line (FTN). The main characteristics of the proton beam dedicated to the n_TOF facility are:

- 20 GeV/c momentum corresponding to the maximum attainable energy with a PS cycle of 1.2 s,

- a single proton bunch of 7×10^{12} particles of 7 ns r.m.s. width,

- possibility of up to 6 bunches per PS supercycle of typically 14.4 s. This parameter is limited to 5 bunches due to the maximum power dissipation allowed on the spallation target and by the radiation level in the target area.

In addition to this *dedicated* mode, which achieves the highest bunch intensities, proton bunches are usually available in the so-called *parasitic* mode. In this mode, the n_TOF bunch is accelerated together with a much lower intensity bunch extracted to the East Hall experimental areas. In the parasitic mode the bunch length is the same that in the dedicated mode, but the maximum intensity is reduced to $\sim 4 \times 10^{12}$ protons/bunch.

Several devices supply information about the beam. The Beam Current Transformers (BCT), installed 6 m before the end of the FTN line, provide a pulse by pulse measurement of the proton intensity delivered to the Target. The digitized value, available through Ethernet, is included in the Data Acquisition System (DAQ) for use in the further data analysis. The Wall Current Monitor provides a pulse (pick-up signal [43]) in the n_TOF Control Room proportional to the instantaneous proton beam intensity and it can be used for timing purposes. In addition, timing signals are available for both modes, which are used to trigger the DAQ.

3.1.2 The Spallation Target

The spallation mechanism is a remarkably powerful neutron source that consists of a highly energetic proton beam hitting on a heavy element target. In a lead spallation target, one $1\,\mathrm{GeV/c}$ proton produce 20-30 neutrons.

The n_TOF neutron source consists of a spallation target made of lead blocks with a total volume of $80\times80\times40\,\mathrm{cm}^3$ [41]. The lead target dimensions have been optimized by means of simulation codes to achieve a compromise between the neutron flux intensity and the neutron energy resolution: a larger target would produce a higher intensity flux but involves longer moderation paths, which decreases precision in neutron energy determination. A $5\,\mathrm{cm}$ layer of water on the exit face of the target slows the neutrons down so that a wide energy spectrum can be obtained. The moderating water is part of the target cooling system that dissipates the large amount of heat generated in the spallation process. The water is in direct contact with the lead target and separated from the TOF tube by an aluminum window [41].

The proton beam enters the target at an angle of $10°$ with respect to the TOF tube axis, that is perpendicular to the target front face. Such an incident angle was adopted in order to reduce neutron beam contamination from the high-energy charged particles and γ rays going out of the target in the forward direction.
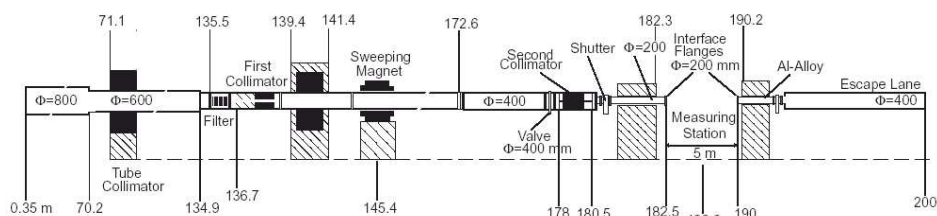

Figure 3.2: *Elements of the TOF tube.*

3.1.3 The TOF tube and beam optics

The neutrons generated at the Target travel nearly $180\,\mathrm{m}$ inside a stainless steel vacuum tube divided in several sections with a progressively reduced diameter. The pressure in the vaccuum tube is less than $1\,\mathrm{mbar}$.

Two collimators are placed at $136\,\mathrm{m}$ and $175\,\mathrm{m}$ to define the neutron beam in the Experimental Area (EA) [44, 45]. The first collimator, made of $1\,\mathrm{m}$ of

iron and 1 m of concrete, has an inner diameter of 11 cm, while the second one, with an inner diameter of 1.8 cm, consists of three sections made of 50 cm of 5 % borated polyethylene, 125 cm of iron and 75 cm of 5 % borated polyethylene. This beam-optics configuration is used for the capture measurements, providing a 4 cm diameter beam profile at the sample location. For the fission campaign, the second collimator has an inner diameter of 8 cm in order to use the larger fission samples.

A 2 m long dipolar magnet, placed behind the first collimator, sweeps away the charged particles from the beam, and an iron shielding, placed downstream the magnet, reduces the muon background.

3.1.4   The Experimental Area and the Escape Line

The Experimental Area (EA) is located after the second collimator shielding wall. It extends from 182.5 m downstream from the spallation target to 190 m. A neutron flux monitor, the capture detectors (C_6D_6) [47] and the sample exchanger were placed in the Area for the capture measurements. For the fission campaigns, they were replaced by the fission detector chambers: the PPACs and the Fast Ionization Chamber (FIC) [17]. The PPAC reaction chamber, placed at approximately 187.5 m, contains the fission detectors used in this work that are described in Section 3.2.

After the Experimental Area, the TOF tube continues along the so-called Escape Line. At the end, a beam dump consisting of a polyethylene block with a cadmium cover reduces the neutron back-scattering to the Experimental Area. Inside the block, three BF_3 gas counters are used to monitor the neutron beam pulse to pulse [49]. Since the 2003 fission campaign, the crates with the front-end electronics, the data acquisition system and the PPAC gas regulation system (Figure 3.6) are located in the Escape Line area.

Different detectors for measuring and monitoring the neutron beam are placed in the experimental area. A monitor consisting of thin-windowed silicon detectors (SiMON) [48] has been permanently placed in-beam during the capture campaigns. The measurements performed with SiMON have been complemented by the PTB detector [42], a standard fission chamber employed to determine the neutron flux during the n_TOF facility commissioning.

3.1.5   Neutron beam characteristics

One of the major tasks during the design phase of the n_TOF facility has been the simulation of its physical performances that were confirmed by the results from the facility commissioning [42]. The most important features for

determining the performance of the n_TOF facility are:

- The integrated neutron fluence at the Experimental Area, which is $\approx 9.6 \times 10^5$ neutrons/7×10^{12} protons with the capture collimating system.

- The time-averaged neutron flux in the flight path direction, as a function of neutron energy [50]. The n_TOF neutron spectrum, plotted in isolethargic units as $\mathrm{d}n/\mathrm{d}(\ln \mathrm{E})/\mathrm{cm}^2/7\times10^{12}$ p, is shown in Figure 3.3. The flat shape of the spectral function of n_TOF in a wide energy domain, from 1 eV up to 10 keV, confirms the isolethargic character expected from the neutron moderation in water. A gravitational cut-off occurs due to the geometry of the beam pipe for neutrons with kinetic energies lower than 0.02 eV.
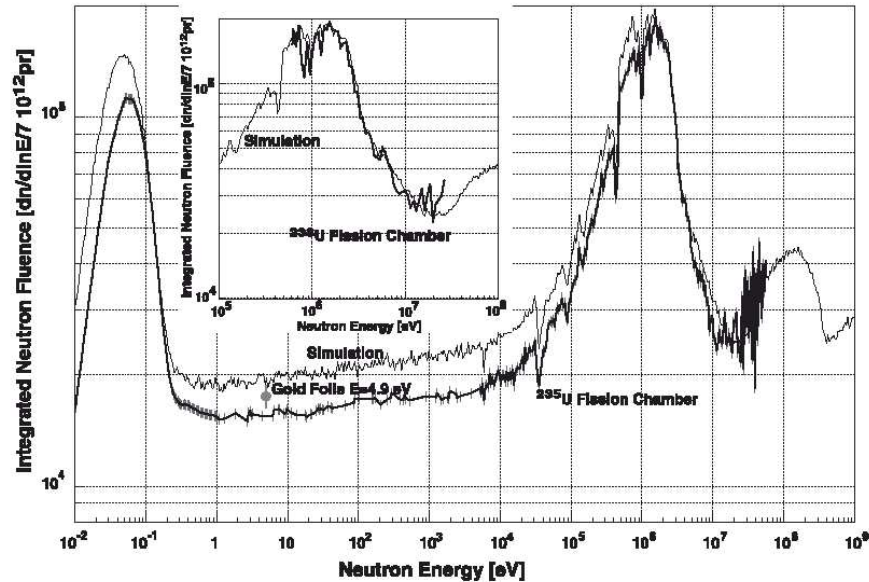

Figure 3.3: *Integrated neutron fluence as a function of neutron energy from ^{235}U and ^{238}U fission chambers (PTB) compared with simulation.*

- The spatial distribution of the neutron beam (beam profile), which has evaluated by the Micromegas detector [51] for the capture campaign configuration.

- The energy resolution as a function of neutron energy [52, 53] and the time-energy relation [54](Appendix C).

- The neutron and gamma background at the area where the detectors are placed [55, 56].

3.2 Fission detection setup

3.2.1 Parallel plate avalanche counters

Gas detectors have been used since the early times of particle and nuclear physics. Nowadays, because of the recent development of heavy ion physics, they are widely used when background radiation prevents the use of scintillator or semiconductor detectors. One of this new detectors is the **P**arallel **P**late **A**valanche **C**ounter (PPAC) that consists in a very thin proportional gas chamber with valuable fission fragment detection qualities [57, 58].

PPACs present many attractive features: they have good timing properties and are not sensitive to radiation damage, there are no sparks from wires, the fast removal of positive ions gives them a high rate capability and they can be built in large dimensions with little cost increase [59], to name a few. They are widely used as first detectors in many experimental equipments to obtain a timing signal [60], also in heavy ion spectrometers [61, 62].

A PPAC consists of two thin parallel stretched foils with the particles passing through the detector perpendicularly to the planes. The gap between the foils must be only a few millimetres wide in order to maintain a high electric field and to reduce the time spread, leading to a good time resolution. The inner pressure of the detector ranges from 1 to 20 mbar. Under these low pressure conditions, a voltage of a few hundred volts, typically $300\,\mathrm{V/(cm\,mbar)}$, is sufficient to reach the proportional regime. The electrons released gain enough energy to produce secondary ionization in the homogeneous electric field, and a Townsend avalanche is triggered.

Typical gases used at proportional counters are mixtures based on rare gases, but when timing is crucial pure hydrocarbons are the best suited. The highest gains have been obtained with isobutane, achieving up to $100\,\%$ detection efficiency in a wide deposited energy range. However, because of the straggling in the gas, the energy resolution is seldom better than about $20\,\%$.

Because of the high electron velocity and the electric field homogeneity, a very short pulse is collected (2 ns rise time). When compared to wire counters, the positive ions hardly contribute to the signal because they are not created so close to the anode. Only the fast component of the signal, produced by the electron drift, is used, while the slow part of the positive ions is suppressed by differentiation of the signal. In some applications it is possible to obtain time resolutions better than 200 ps, even in large dimension detectors [58].
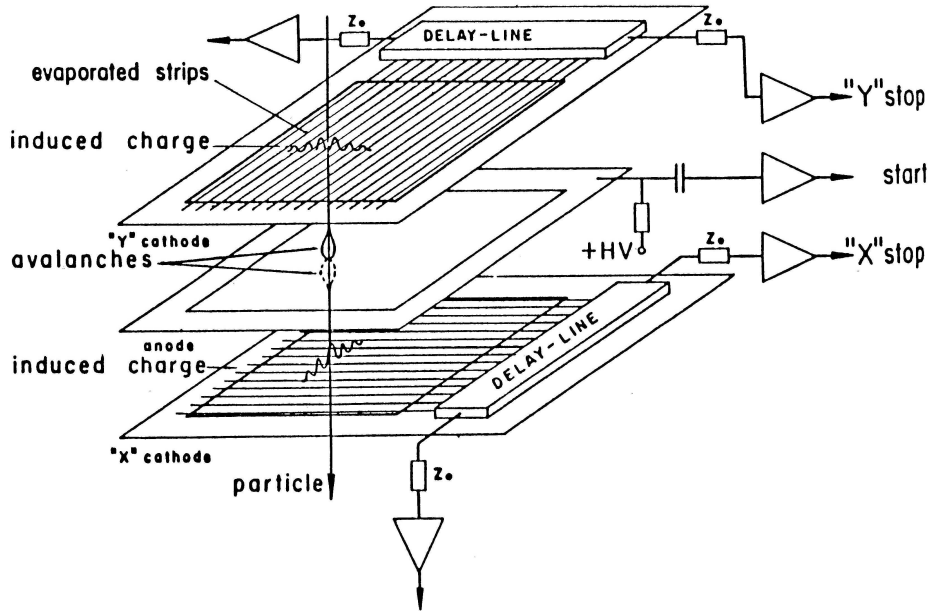
Figure 3.4: *Principles of bidimensional, induced charge read out from parallel plate avalanche counters [63].*

With this kind of avalanche parallel plate detectors, the localization of the primary ionization is obtained by means of stripped cathodes, using fast delay lines to reconstruct the center of gravity of the induced charges [62, 63] (Figure 3.4). A resolution better than $300\,\mu$m has been obtained using detectors with a strip pitch of $2\,$mm. Although most authors use manufactured delay lines, the best results have been obtained by those who built their own delay lines. Delay lines are made of a continuous winding on a threaded plastic rod that has taps every 3 to 5 windings to constitute individual cells. Delays of a few nanoseconds per element have been obtained with impedances of the order of $100\,\Omega$ [57]. These delay lines have a better rise time, higher impedance and less amplitude attenuation than the commercial ones.

For the n_TOF facility, several PPAC of $20 \times 20\,$cm^2 surface were built at IPN d'Orsay (France) [64]. The anodes consist of a $1.5\,\mu$m Mylar foil aluminized on both sides and glued onto a frame (see Figure 3.5). The frame is made of a kind of epoxy resin, which is coated with a thin metallized layer of copper – gold plated to prevent copper oxidation – in order to shield the detector against electromagnetic noise.
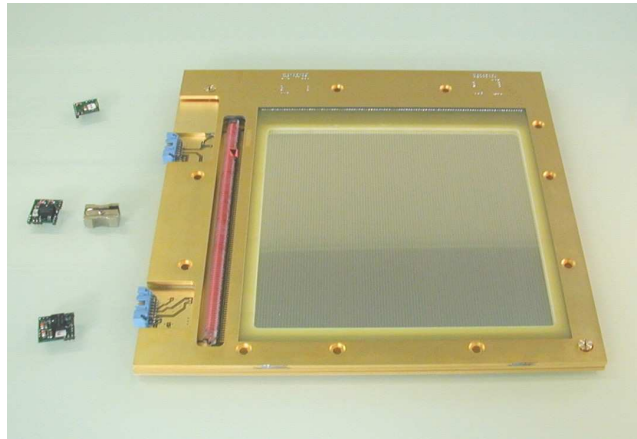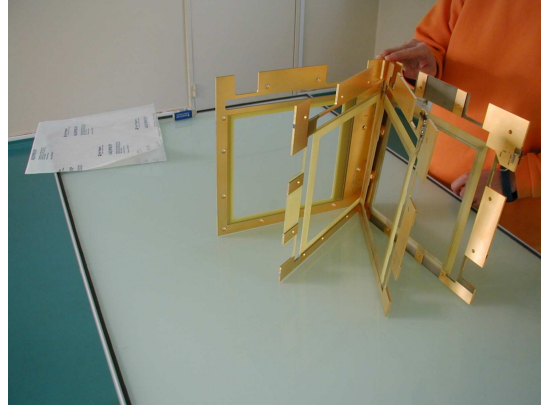
Figure 3.5: *In the top picture the PPAC frame is shown before the installation of the electrodes. In the middle, PPAC appearance where the stripped cathode, the delay line on one side and some preamplifiers are shown. In the bottom, a delay line detail showing how each cathode strip is soldered to a delay line rod.*
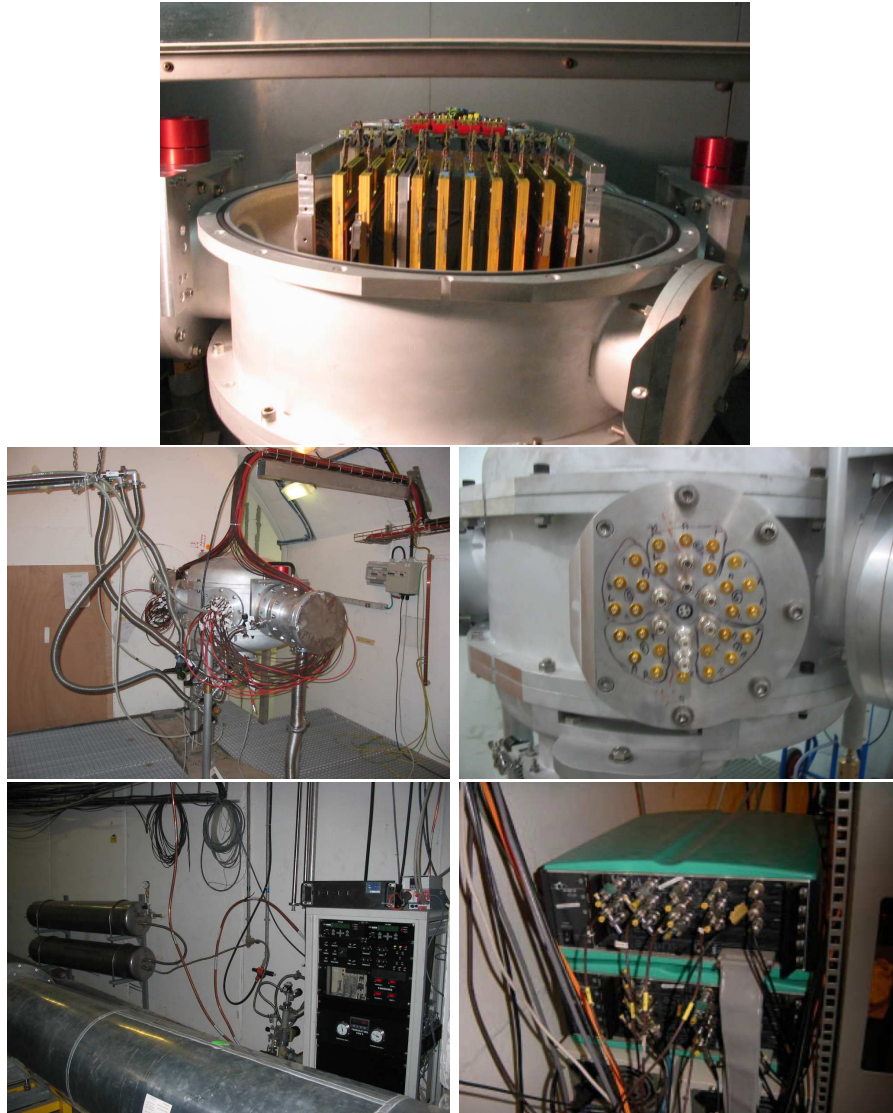
Figure 3.6: *In the top, a picture of the opened PPAC chamber during the target replacement, while in the middle, the chamber already installed at the Experimental Area and a detail of signal connections. In the bottom, the gas regulation system and some of the DAQ crates are shown.*

The cathodes, placed at both anode sides, are also made by Mylar foils with deposited aluminium strips every $2\,\mathrm{mm}$. Each strip is connected to a cell of a delay line. The two cathode strips are orthogonally placed in order to achieve the two-dimensional position (X,Y) of the fission fragment hit.
The delay line, designed at IPN, consists of a plastic rod with a coiled copper wire. The effective length of the rod is $20\,\mathrm{cm}$ and an intermediate space of $6\,\mathrm{mm}$ at each side connects the delay line to the preamplifiers.

The spacing between the anode and each cathode is $3.2\,\mathrm{mm}$. Before 2003, isobutane ($\mathrm{C_4H_{10}}$) at $7\,\mathrm{mbar}$ was used to fill the detectors, but for the 2003 campaign, for safety reasons, it was replaced by octafluoropropane ($\mathrm{C_3F_8}$) and the operating pressure was reduced to $4\,\mathrm{mbar}$. $\mathrm{C_3F_8}$ is a non-flammable gas with a fast signal rise time and larger ion energy loss. During the experiments, the entire detector setup is confined in a vessel (reaction chamber) to keep the under-pressure (see Figure 3.6). The enclosure consists of a cylindrical aluminum chamber of $600\,\mathrm{mm}$ of diameter, with $6\,\mathrm{mm}$ thick walls, and two hemispherical lids. It is connected to the beam pipes by two flanges where $75\,\mu\mathrm{m}$ Kapton foils ensure the sealing of the chamber.

The electrodes of the detectors are fed by a general-purpose CAEN High Voltage module. The selected voltages vary for each detector because the registered current depends on the target activity. Table 3.1 presents the values used during the measurements included in our analysis.

Detector	HV (Setup 0)	HV (Setup 1)
0	550	560
1	540	560
2	550	570
3	540	550
4	540	560
5	540	560
6	540	560
7	530	540
8	540	550
9	550	570

Table 3.1: *PPAC detectors HV for Th-U runs. Two different sets of HV values, referred to as Setup 0 and Setup 1, have been used.*

Figure 3.7: *Schematic view of the ^{234}U and ^{232}Th setup used during the 2003 campaign. The detectors are labelled by their numeration in the arrangement; the same convention is used with the targets.*

3.2.2 The fissile targets

The targets are made from the fissionable isotopic samples that we want to measure. They are placed in between two PPAC detectors, so that in the n_TOF PPAC setup, which consists of ten detectors in a row, up to nine targets can be included at the same time (Figure 3.7). The targets were made at the IPNO[1] and installed inside the chamber at Orsay. The chamber transportation to the n_TOF facility was done in agreement with the Swiss and CERN authorities, in charge of radioprotection.

Target availability

During both fission campaigns at the n_TOF facility, in 2002 and 2003, targets of thorium, uranium and neptunium were measured with PPAC detectors. A detailed list of the different nuclei is presented in the following tables:

Sample	Purity(%)	Nb of targets	total mass(mg)	activity/target
^{232}Th	99.99	4	60	60 Bq
^{234}U	99.08	3	45	5 MBq
^{235}U	93.20	1	15	25 kBq
^{238}U	99.99	1	15	190 Bq

Table 3.2: *Targets measured during 2002 n_TOF campaign (September-October)*

---

[1]Institut de Physique Nucléaire d'Orsay

Sample	Purity(%)	Nb of targets	total mass(mg)	activity/target
^{232}Th	99.99	5	75	60 Bq
^{234}U	99.08	2	45	5 MBq
^{235}U	93.20	1	15	25 kBq
^{238}U	99.99	1	15	190 Bq

Table 3.3: *Targets measured during the first period (September) of 2003 campaign*

Sample	Purity(%)	Nb of targets	total mass(mg)	activity/target
^{237}Np	99.99	4	60	0.6-0.8 MBq
^{233}U	99.95	1	15	5.4 MBq
^{235}U	93.20	1	15	25 kBq
^{238}U	99.99	1	15	190 Bq

Table 3.4: *Targets measured during the second period (October-November) of 2003 campaign*

^{235}U and ^{238}U are the standards for fission cross section, so they are included in every setup to provide the neutron flux information.

Target description

Thorium and uranium targets were made using bulk material from IPNO and IRMM[2] (Geel). The targets are composed of an 80 mm diameter deposit of the element over an aluminium foil $2\,\mu$m thick, with a surface area of $10\times10\,$cm^2 and 99.5 % of purity (Figure 3.8). The aluminum foil is glued to a 1.5 mm thick epoxy support of 270 mm$\times$240 mm with a 120 mm diameter centre hole in which to place the target.

The deposit is made by a chemical method known as *molecular plating*. In this procedure, a nitrate form of the element is dissolved in isopropylique alcohol with a small amount of water. A 600 V potential is then applied for 15 minutes between a platinum foil and the aluminium foil which is used as backing to obtain by electrodeposition an adequate amount of material on the aluminum support. After electrolysis, the material is stoved during few hours to remove the residual alcohol and water. The resulting deposits are in the form of nitrates, oxides or hydroxides. Very pure isotopes were used in all cases, especially for ^{234}U, ^{238}U, ^{232}Th and ^{237}Np, for which fissile isotopes impurities were always negligible.

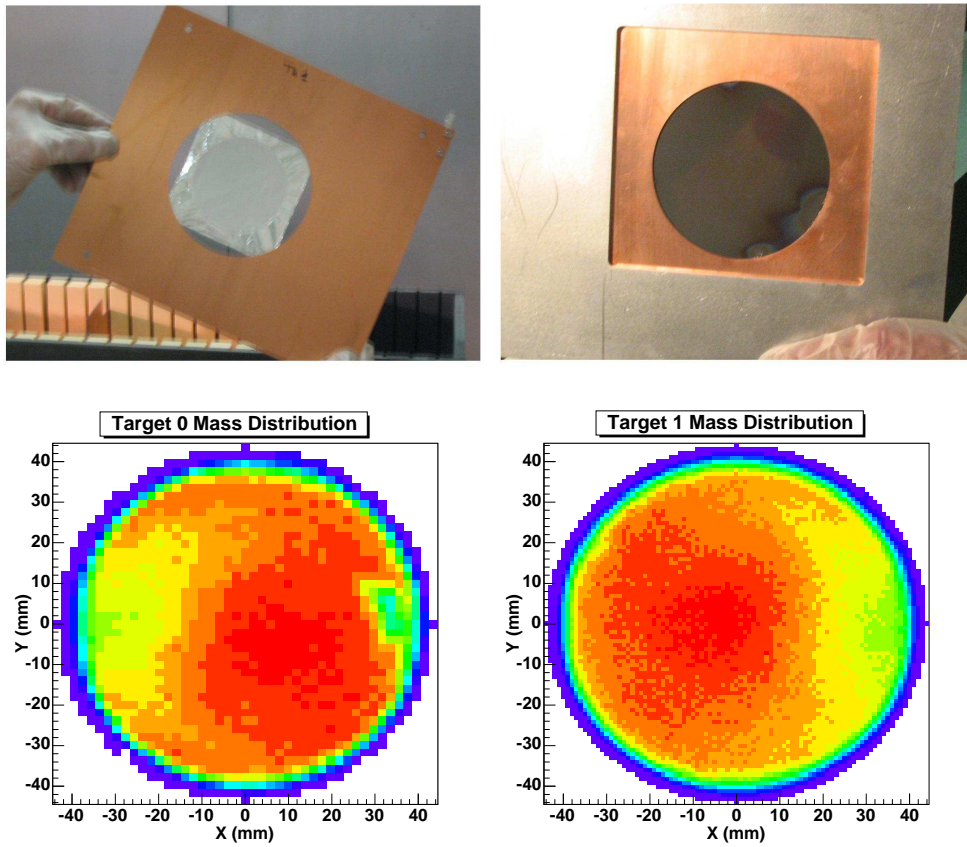[2]Institute for Reference Materials and Measurements

Figure 3.8: *The upper photos show the backing and the deposit of the targets. The color histograms represent the two ^{234}U mass distribution targets obtained from alpha counting.*

The accurate knowledge of the thickness of the deposited layer and its inhomogeneities is required for a reliable determination of the absolute cross sections. For all the radioactive targets, the total amount of nuclei is measured by counting alpha radioactivity at large distances with a collimated silicon detector, taking into account the presence of impurities by a selection in the energy spectrum of the alpha particles. In the case of ^{235}U, where an impurity of ^{234}U was present, this measurement is complemented with a mass spectrometry analysis from which we are able to measure the total number of nuclei per target with an accuracy better than 1 %.

A more detailed description of the target fabrication and characterisation procedures can be found in Laure Ferrant's thesis [65].

3.2.3   Gas regulation system

Due to the experimental characteristics, a gas flow system gives the best performance conditions. The gas enters the chamber flowing in between the PPAC electrodes to ensure a proper sweeping of the ions created by the fission fragments. A steady flow of around 50 litres per hour is enough to keep a constant pressure in the chamber. The gas is continuously renewed, so the proportionality remains practically constant during the experiment. The regulation system maintains a constant differential pressure between the vacuum tube and the detector device by means of a pressure sensor connected to the vacuum and the gas circuit [41].

Specific safety circuits are activated in case of any failure of the regulating devices. Lower and higher pressure thresholds prevent over or under-pressure in the system, which could happen if the pump breaks down, for instance.

3.2.4   Electronics

Two different types of preamplifiers have been used in the PPAC detectors. Those connected to the anodes are simple current amplifiers, which are used to get an enhanced signal as fast as possible. They are implemented to cut the large time tail coming from the positive ions, so that only the electron fast signal is used. The cathode signal treatment is more complex. A charge amplifier is used under conditions that a circuit with only resistive impedance is obtained. This is designed to match the delay line resistance, thus minimizing the signal reflected in the union.

Both types of preamplifiers have been designed at the IPN d'Orsay, optimising their behaviour for the detector signal expected from the fission fragment ionization. Their small size is well-suited to fit inside the PPAC frame

(Figure 3.5). Each preamplifier is fed with 5 V. The technical drawings are shown in the Appendix D.

The preamplifier outputs are carried by approximately 10 m BNC cables from the PPACs to the Escape Line area, where the Data Acquisition System is placed.

3.3   Data Acquisition System

One of the unique features of the n_TOF facility is its powerful Data Acquisition System (DAQ) [66], based on Flash Analog to Digital Converter (FADC) modules, which has been developed with special attention to the neutron beam repetition rates, the expected number of event rates and the signal characteristics of the different detectors employed. It has the exclusive capability to sample and store the full analogue waveform of the detector signals for each neutron pulse by using on-line zero-suppression. This DAQ architecture permits the full reconstruction of the detector response in the off-line analysis, so that pile-up or background events can be resolved. Nevertheless, because of the huge amount of data accumulated, this procedure is only possible where high transfer rate and storage capabilities are available, such as we have at CERN.

The FADC modules used at n_TOF are Acqiris Digitizers [40] with a coding range of 8 bit and an internal buffer memory of 8 MB for each channel. The PPAC channels work typically with a sampling rate of 500 MHz; at this rate the buffer is full in 16 ms after the trigger, which corresponds to 0.7 eV when translated to the neutron energy scale. The data stored by a Digitizer channel in its 8 MB memory buffer contains the full detector information for a neutron pulse; we will refer to it as the *FADC movie*.

After the sampling is completed, the data are transferred to a readout PC which is connected to the FADC modules placed in a PCI crate via a PCI link (see Figure 3.9). Accordingly, the data transfer rate from the FADC to the PC memory is limited by the PCI bus bandwidth to the usual value of 80-100 MB/s. Because of this rather slow transfer rate, only a certain number of channels can be transferred to the readout-PC during the 1.2 s of minimum time between two proton bunches. For this reason, we have reduced the number of channels served by each PC to eight, which corresponds to a data stream. As each digitizer has 2 or 4 channels, we have two or three modules for each PCI crate and so the 50 channels needed by the PPAC detectors are distributed in 7 streams.
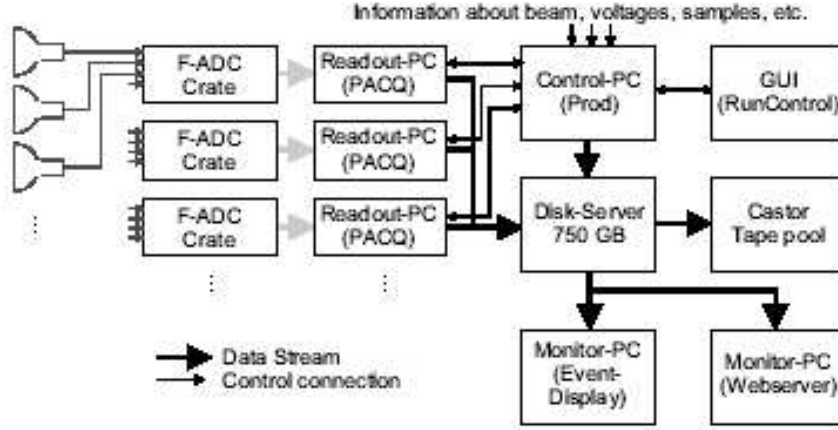
Figure 3.9: *Schematic view of the n_TOF data acquisition system. The output produced by the detectors is digitized by the FADCs over a period of typically 16 ms. The data is transferred via cPCI/PCI adapters into the readout PCs which compress the data and transfer it over Gigabit links (bold black arrows) to the disk server. Here, the data is waiting to be transported to the tape pool. An additional PC synchronizes the whole system and acquires information about the proton beam high voltages, samples, etc.*

3.3.1   Trigger signal

The prompt beam pulse from the PS, properly attenuated and delayed, generates the trigger signal at the Control Room. The jitter of the prompt beam pulse is of the order of few nanoseconds. A single, high quality coaxial cable conveys this signal to the experimental area where a special fan-out unit distributes it to the individual digitizer modules via equal length cables. The skew of each output is less than 200 ps with respect to all other outputs. The time T0 (the time when the beam hits the target) is calibrated by a current pulse signal arriving from the beam monitor situated at the entrance to the target.

3.3.2   Zero-suppression algorithm

Software is used to remove unnecessary information from the data stream (i.e. zero's). In the zero-suppression algorithm [40] method:

- Only pulses above a set threshold (the hardware threshold) are considered as valid data (signal).

- A number of pre-samples and post-samples must be recorded with each signal, according to a set value.

- No pulse below the threshold is copied to memory except if it is included inside the pre- or the post-samples of a valid signal.

Therefore, for every signal, the data copied to memory comprise the pre-samples followed by the valid data, followed by the post-samples. There are a few exceptions, however:

- At the start of acquisition memory, if a signal is present closer to the acquisition begin than the set pre-sample period, only the reduced sample interval is added to the data stream.

- At the end of acquisition memory, if a signal is followed by an interval of post-samples smaller than the set post-sample period, only the samples from this interval is added to the data stream.

- When a new signal arrives during the post-sample interval of the preceeding signal, the post-sample interval is reset to the set value and pushed forward until data go again below the threshold. Both signal frames appear merged in the *FADC movie*.

After zero-suppression data are ready for transfer via a Gigabit link to the disk server where it is temporarily stored before being sent to the CASTOR (CERN Advanced Storage Manager) mass storage system by the Central Data Recording (CDR) [68]. The file size (2 GBytes) has been selected to minimize the data losses in case of file corruption whereas the number of files produced is not excessive. A continuous data acquisition period is called a *run* and each one of the files in which a run is partitioned due to size constraints is called a *segment*. The recorded data at the disk server can be displayed for monitoring purposes by means of the Event Display software, which allows an on-line checking of the detectors.

Chapter 4

PPAC data reduction

The procedure of transforming the information provided by the detectors into a reaction yield is usually called **data reduction**. The fission reaction yield is defined as the neutron fraction that undergoes a fission reaction when it impinges the sample. The observed counting rate is then determined by the reaction yield, the incoming flux and the detector system efficiency. A full description of the data reduction method we are using is also required in order to produce evaluated neutron-induced fission cross sections. In this chapter, the data-reduction process is described step by step.

4.1   Raw data treatment

As explained in the previous chapter, the Central Data Recording service of CERN manages the n_TOF raw data that are stored at CASTOR [68]. The zero-suppressed raw data stored for an experiment contain the frames of the signals for each detector and for every neutron pulse and have been recorded according to a logical structure of headers called BOS Banks [39]. In order to handle these raw data files, a software package was developed, translating them into DST (Data Summary Tape) format[1]. This software is used for all the detectors employed at the n_TOF experiment, including a routine which is specific for each detector and supplies the list of signal parameters useful for the analysis. The DST files, stored also at CASTOR, are accessible by means of the same software from any CERN LXPLUS computing machine.

The specific routine written for the PPAC signals includes a pulse shape

---

[1]The n_TOF DST-creation software, available at CERN LXPLUS from the directory $/afs/cern.ch/user/n/ntofuser/public/last\_soft$, accesses files in CASTOR using rfio (Remote File Input/Output) protocols.

analysis [67] that makes it easier to recognise the true peaks. The routine calculates the derivative of the signal by a convoluting procedure that includes a high-frequency filter to remove the baseline fast variations.
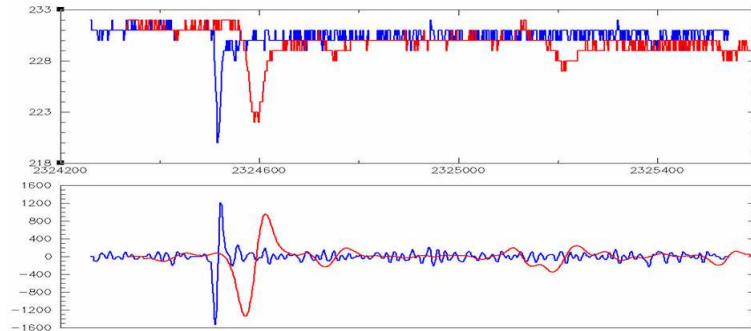

Figure 4.1: *An anode (narrowest peak) and cathode (broadest one) signals before (upper part) and after (lower part) the convolution is applied.*
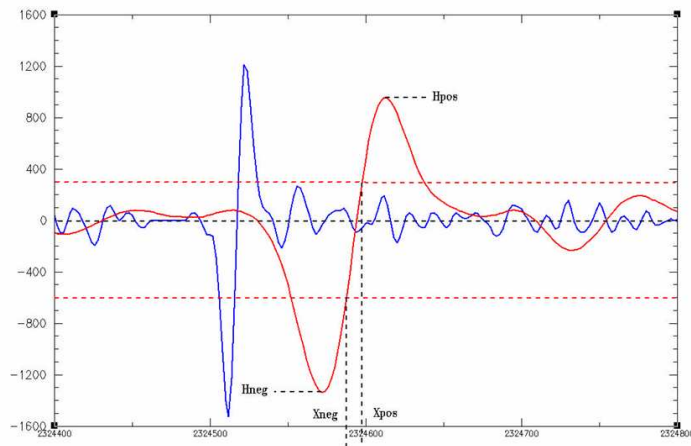

Figure 4.2: *A zoom into the second chart of Figure 4.1 shows the thresholds set for the cathode signals (dashed horizontal lines), the separation between threshold-crossing points (Xpos-Xneg) and the signal amplitude (Hpos-Hneg).*

After derivation, the signals have a bipolar shape (see Figure 4.1) and the peak discrimination is carried out by applying the following conditions to the signal polarity, the threshold-crossing points and the peak separation of the bipolar signals (shown in Figure 4.2):

- Two thresholds, positive and negative, must be crossed by the bipolar signal, producing four crossing points.

- The polarity must be negative, i.e., the negative part is coming first in time.

- If the two alternations are too far from each other or they have very different amplitudes, the bipolar signal is rejected.

For each signal two parameters are saved in the DST files: a time, defined by the zero-crossing of the filtered derivative, and an amplitude, defined as the peak-to-peak amplitude of the filtered derivative. In addition, there must be a time calibration for channel synchronisation, in order to achieve a good time accuracy when searching for time coincidences between the anode signals.

4.1.1 Time calibration of the Digitizers

Each Acqiris digitizer has an internal clock with a nominal accuracy of ± 2 ppm (parts per million) [69], which means that, inside a *FADC movie* (defined in Section 3.3), it is possible to have deviations of up to tenths of ns between Digitizers. The fission event building, that will be described later, requires time coincidences of only a few nanoseconds accuracy. Therefore, the time differences among the Digitizers need to be very precisely calibrated. This must be done for each campaign using the same DAQ configuration settings that are used for the experiments. For calibration we use a pulse generator signal that is split by an accurate fan-out, and every output is connected to a Digitizer. One channel is taken as the reference channel and the differences between the other channels and the reference are measured and time deviations are corrected by software at the DST creation level.

The calibration signal used is a squared pulse of 20 ns width and 100 μs period. The memory buffer of the Digitizer channels can hold with 160 calibration pulses that give accurate threshold-crossing points for the calibration procedure. As the reference signals are split in parallel for all the channels, the time differences between reference and every channel change slightly as their internal clocks count up. We have found differences of the order of ten nanoseconds at the 16 ms full scale. A linear fit for each channel gives us the time corrections (Figure 4.3) that we are included in the PPAC routine.
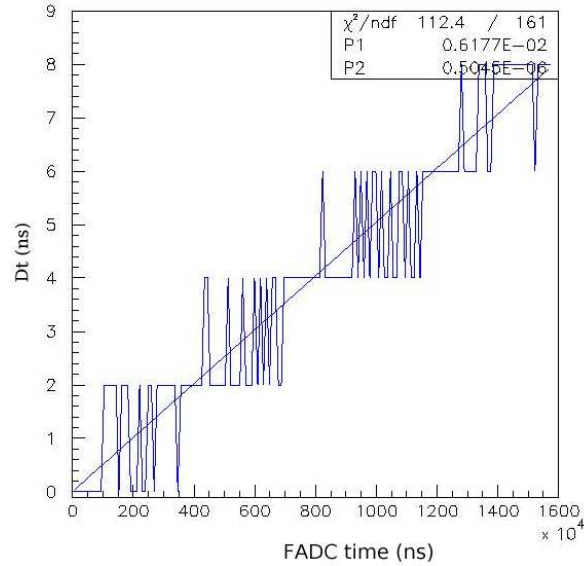
Figure 4.3: *Example of the time deviation from the reference channel (Dt) versus the absolute time of the signal (FADCtime). Both axis are given in ns. As it is shown in the figure the deviations can reach several nanoseconds at the last part of the movie. The slope of the fit contains the information about the deviation of the internal time scale of the considered channel.*

4.2   Fission event building

As the raw signals are treated by derivation, their shape becomes meaningless and the only quantities saved to the DST files are the peak time and the amplitude, as previously defined, so that the data treatment is based only on these parameters. Actually, fission identification lies on the time coincidence between adjacent detectors, hit by the two fission fragments coming from the same fission reaction (*complementary* fission fragments). In order to understand the fission event building process, it is worth to review briefly the functioning of the PPAC detectors.

A PPAC, as explained in the previous chapter, is a very thin gas detector, practically insensitive to gamma rays and neutrons but virtually 100 % efficient for the detection of massive charged particles that cross it, as fission fragments do. It means that we can place two PPAC detectors inside the neutron beam, up and downstream from the fissioning target, without significantly disturbing
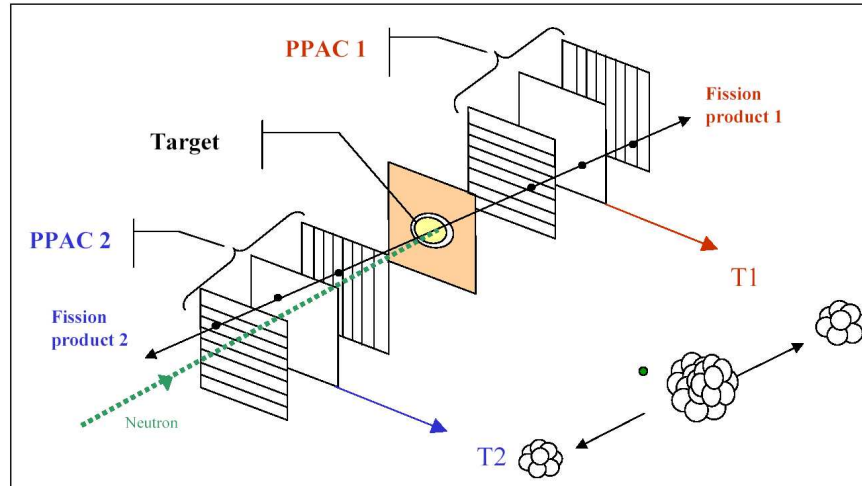
Figure 4.4: *Schematic diagram of a fission event in the PPAC detector.*

the beam. As the PPAC detectors are close to the target (less than 2 cm), the two fission fragments reach the detectors almost simultaneously, producing two signals in close coincidence that characterise a fission event (see Figure 4.4).

However, the actual setup is more complex because, in order to optimize the beam time, nine targets were simultaneously placed in beam, instead of just one, for a total of ten detectors with nine targets in-between (Figure 3.7). Thus, the task of identifying the target where the fission occurs becomes more difficult: each PPAC (except the external ones) faces two targets and some fission fragments can cross more than one PPAC before stopping, producing a fission event where more than two detectors have been fired.

Several types of fission events have been defined to describe the cases where two or more detectors are fired by the two complementary fission fragments, and are named as type_2, type_3 and type_4, according to the number of detectors involved. A schematic description of each type is shown in Figure 4.5. Any higher order of coincidences is disregarded because the probability that it would occur is too remote.

The main part of the event-building process consists in identifying which signals belong to the fission fragments coming from a fission in the target of interest and distinguishing them from signals produced by other fission products or background signals such as alpha activity or high-energetic reactions in the detectors. When, at least two adjacent detectors fired within a narrow window of less than 10 ns, this is considered a fission event. Nevertheless, as we
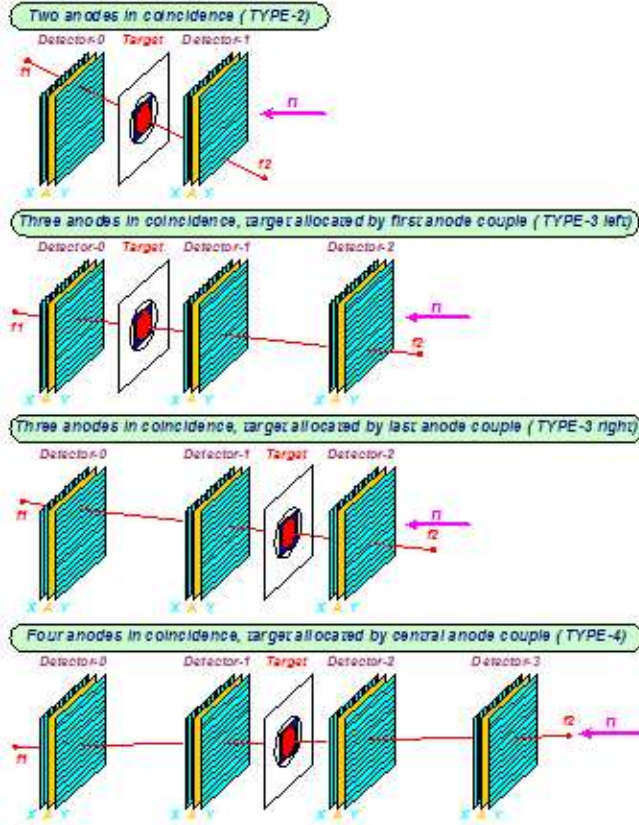
Figure 4.5: *Description of the possible cases for fission fragments at the PPAC setup. Only the target where fission happens is represented with the involved detectors. Notice that two diagrams represent the type_3 case, depending on the FF that crosses two PPACs.*

explained before, it is possible for the fission fragments to fire more than one detector. In Figure 4.5, the type_3 events are ambiguous because the fragments can come from the target on the left (second figure) or from the target on the right (third figure). Ambiguity increases even more, if a given event is close in time with a spurious signal in any of the surrounding detectors. This ambiguity can be resolved by measuring the time that the fission fragments need to reach the detectors involved against the time between two complementary fragments. Hence, for the different types of fission events, the time differences (correlations) among the involved detectors were estimated in a preliminary analysis. Likewise, the signals from the cathodes and the signal produced in the PPAC by the Gamma Flash were also properly examined.

4.2.1 Search for coincidences of anode signals

As mentioned above, coinciding anode signals point the fission events and their signal times determine the time at which a fission event has taken place. Before describing the search algorithm, we should define what we understand by a PS event and how it is used.

The distinguishing feature of the n_TOF facility is the use of a pulsed neutron source in which the neutron pulse is produced by a PS proton bunch impinging the spallation target. The signals registered by the PPACs for a neutron pulse come in a short interval of several milliseconds and are gathered together by the DAQ in what is called a PS event. A PS event contains complete information for all the signals in the 50 FADC channels connected to the PPACs, including the channel, time and amplitude for each signal. In the DST files, the signals of a PS event are grouped by FADC channels and each channel is sorted by time.

The analysis program downloads from the DST all the data related to the current PS event and stores it into a temporary memory buffer from where the data are used by the analysis subroutines. The analysis program accessess the buffer by means of a two-dimensional array of pointers with the array indexes related to the detector and electrode numeric labels.

The algorithm implemented to look for the coincidences is rather simple: it uses a coincidence window between adjacent detectors of 40 ns width, large enough to contain not only the signal from the complementary fission fragment, but also the signal produced by the same fragment crossing a second detector. Starting from the first detector, the one labelled as zero, every anode signal is taken to search for anode signals in the next detector within the coincidence window. For every matching signal at the second detector, we repeat the previous step: a time window is opened and we search inside for anode signals in the next detector. This iterative process ends when no matching signal is found or when four different detectors have already been considered. From here on, every set of coincident signals from different detectors is referred to as a *configuration*. With this procedure, several types of *configurations*, depending on the number of included signals, can be found and they can be classified as type_2, type_3 or type_4, using the previously defined notation.

Once all the signals belonging to the first detector have been treated, the same procedure is repeated for the next detector, excluding those signals which are already included in any previous *configuration*. The remaining detectors are processed in the same way, considering every possible coincidence.

This algorithm is quite simple but the number of *configurations* so obtained greatly overestimates the actual number of fission events because the same

signals can be used to build several *configurations*. Despite this, it turns out very useful for studying the performance of the different targets and detectors.
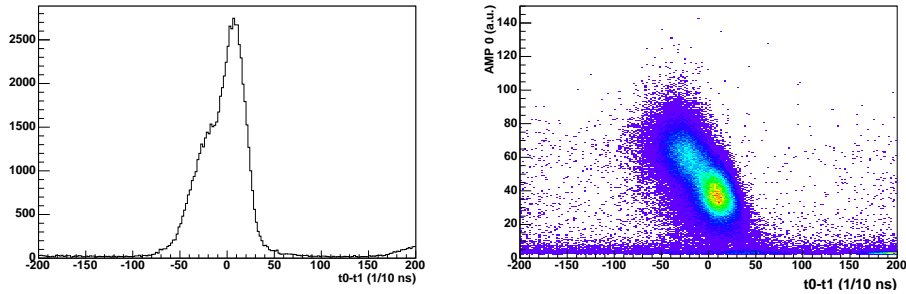

Figure 4.6: *Distribution of the time differences in type_2 configurations found in detectors 7 and 8 for run 4902. In the second plot, the time difference is represented versus the signal amplitude at detector 7.*
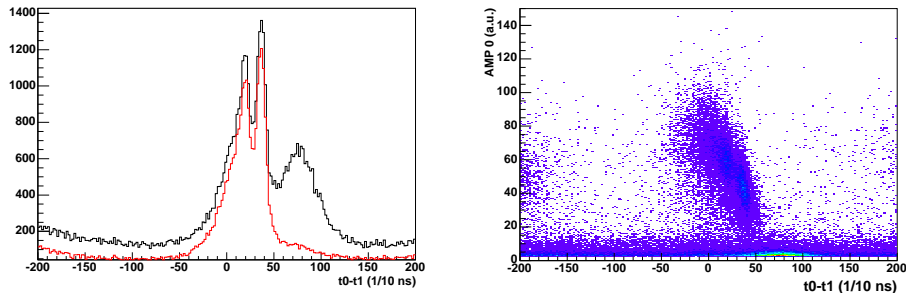

Figure 4.7: *The same for detectors 0 and 1 and several runs grouped. The large background contribution around 8 ns disappears when very low amplitude signals are rejected (light histogram).*

The remaining analysis work has been developed on the ROOT framework [70]. For every run we create the corresponding ROOT file where the *configurations* that we found are saved by assigning them to a ROOT class called *TTree*. This ROOT class provides a powerful system for storing and compressing a large amount of data that can be quickly accessed. Each *configuration* is saved to a *Ttree* labelled with the *configuration* multiplicity and the index of the first detector included. Using a specific ROOT script we can group a full set of runs together and study each type of *configuration* by selecting the corresponding *Ttree*. This make it possible to determine the time and the amplitude conditions that fulfill the true fission events related to each target and fission type.
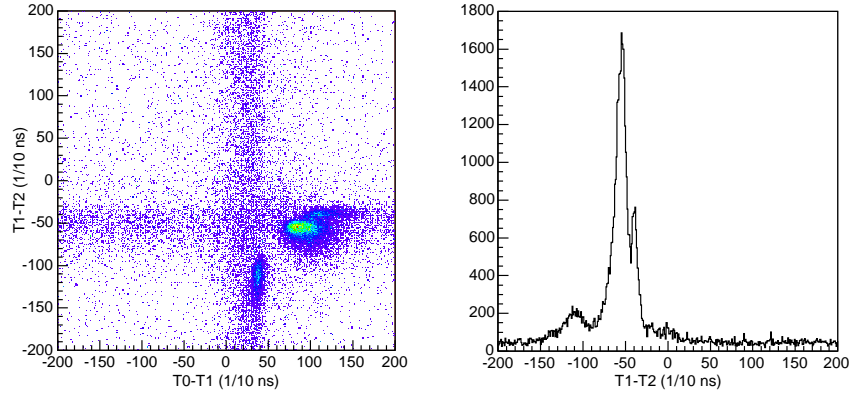
Figure 4.8: *Two-dimensional time difference distribution for Type-3 events involving the former three detectors. As we see in the second histogram (Y projection of the first plot), if only the time window is considered, some ambiguity is present in the identification of the target, because the two peaks corresponding to both possible targets overlap.*

The results of this analysis have given us some helpful information:

- Most of the signals from fission fragments have large amplitudes. Therefore, setting by software an amplitude threshold for the anode signals greatly reduces the low amplitude noise, especially at high neutron energies.

- The time difference between two complementary fission fragments varies within a range of about 10 ns (see Figures 4.6 and 4.7). Although the distribution spread of this difference is practically constant for all the detector couples, the mean value may vary by a few nanoseconds, due to the different electronic path of each channel. As we will see in Subsection 4.2.3, the offsets of the channels can be accurately corrected using the additional information from the Gamma Flash.

- By studying those *configurations* with multiplicity greater than two, we realised that it may take less time for a *fast* fission fragment (those very energetic in the light group) to travel between two adjacent detectors than a *slow* fragment to reach the closest detector from the target. This possibility introduces additional ambiguity in the identification of the target where the fission occurs (see Figure 4.8). The amplitudes of the signals involved help us to recognise such cases and the separation
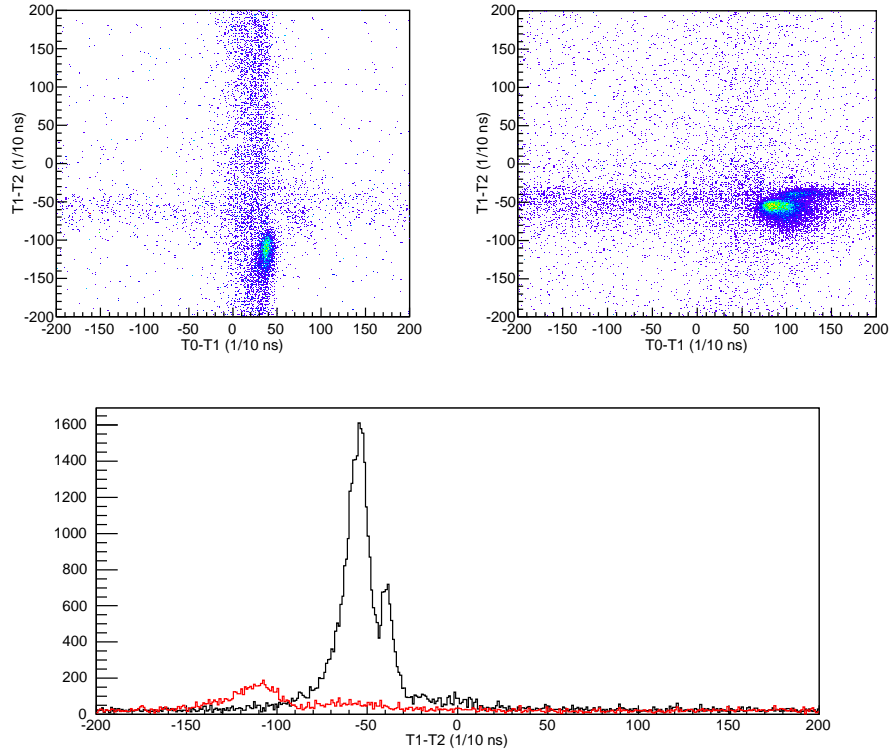
Figure 4.9: *Time-difference distributions applying amplitude selections: first plot, first detector amplitude larger than the third one, the events originated at the first target remain; second plot, third amplitude larger than first one, the events from the second target remain; 1-dimensional projection of the previous cases, the ambiguity is resolved.*

among fission events originated at the different targets can be achieved by setting additional amplitude conditions (see Figure 4.9).

4.2.2   Cathode signal analysis

As explained in Chapter 3, a particle crossing the detector produces signals in both cathodes. The cathodes are divided into parallel strips that are placed horizontally in the first cathode and vertically in the second one. The strips are soldered to a delay line where the signal propagates in both directions, with both ends connected to their corresponding preamplifiers. Using the time information from both cathodes we can obtain the detector-crossing position

of the hitting particle.

To get the spatial position of a given fission fragment, a couple of signals for each detector cathode and the related anode signal are required. Both cathodes are treated separately using the same procedure: starting with the anode signal, the correlated cathode signals are searched in a time interval equivalent to the delay line length after the anode signal. We assume that a cathode signal reaching either end of the delay line spends a time Tch1-T0 or Tch2-T0 travelling along the delay line, where Tch1 and Tch2 represent the time registered for a signal at one of the cathode channels and T0 is the anode signal time for the hitting fragment. When the two signals produced by the same fragment arrive at both ends of the delay line, the sum of their propagation times must be the total delay length (DLT), so that they fulfill the expression:

$$Tch1 + Tch2 - 2 \times T0 = DLT. \qquad (4.1)$$

that is referred to as the *diagonal* condition. This name is taken from the appearance of the propagation time distribution when plotted the one against the other (see Figure 4.10). For the sake of simplicity, those signals produced by the split of one pulse in the delay line will be referred to as **_siamese_** signals.
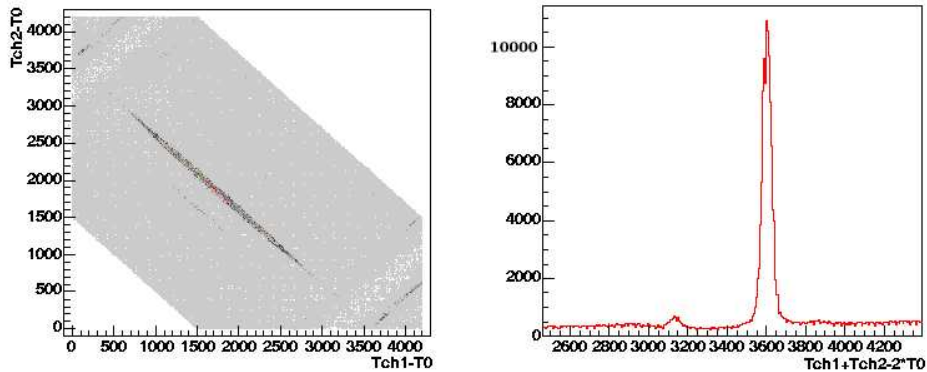

Figure 4.10: *The correlation between the propagation times along the delay line for a couple of cathode channels is shown in the first chart. The second chart shows the time distribution when the times are added. Time units are tenths of nanoseconds.*

The time resolution in the signal measurement implies some uncertainty
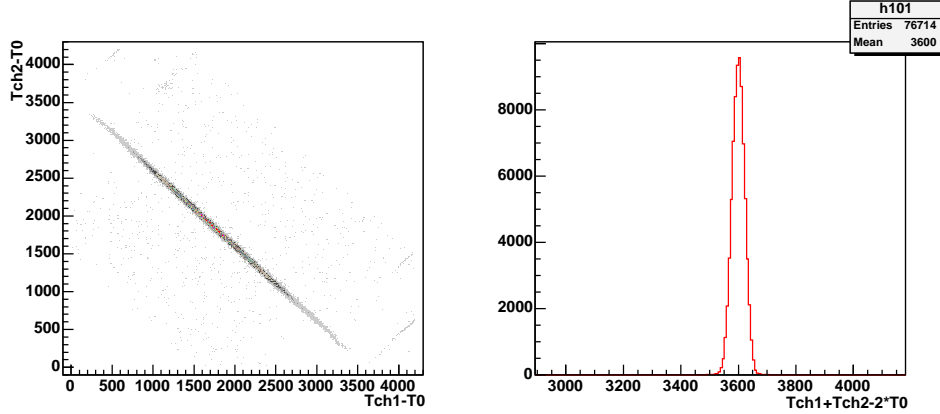
Figure 4.11: *Histograms from Figure 4.10 after applying some cuts in amplitude (amplitudes larger than 12) and time-of-flight (removing high-energy spectrum). Most of the spurious couples disappear, whereas a large percentage of the real signals due to fission fragments are remaining. This is the case of a detector near the ^{235}U target, which presents many fission signals at low energies.*

in the obtained DLT which is shown in Figures 4.10 and 4.11 as a broadening of the width around the average DLT value. Random associations between non-correlated signals can be observed as background outside the diagonal.

The cathode signals in the FADC channels are accessed by means of pointers in the same way than the anode signals, so that a procedure similar to that used for finding anode coincidences can be implemented to search for *siamese* signals. At this preliminary stage, generous limits for the DLT condition are set in order to obtain a general overview of cathode behaviour, studying the DLT widths for every cathode and obtaining the limits for a later use. The amplitudes of the *siamese* signals have also been studied, supplying additional information about the performance of the delay lines. Since they come from the same hitting fission fragment, their amplitudes should be correlated and, besides, this correlation is extended to the anode signal amplitude as it is produced too by the same fission fragment.

The amplitude features have been studied for the different cathodes and we found that the amplitude ratio between *siamese* signals in a cathode (Ach1/Ach2) and between the cathodes and the related anode signals (Ach1/A0 and Ach2/A0) are also useful for removing spurious couples. Some results obtained for one of the cathodes of detector 7 are shown in Figures 4.12 and 4.13. At low energies, the background due to random signal associations is
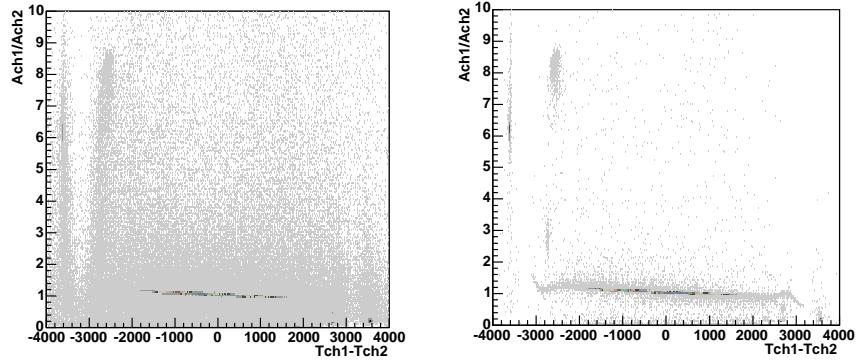
Figure 4.12: *The cathode amplitude ratio is shown for the full energy spectrum (left chart) and for low-energy signals when random background is suppressed (right chart). The correlation for the fission signals is certainly high, lying the ratio near 1.*
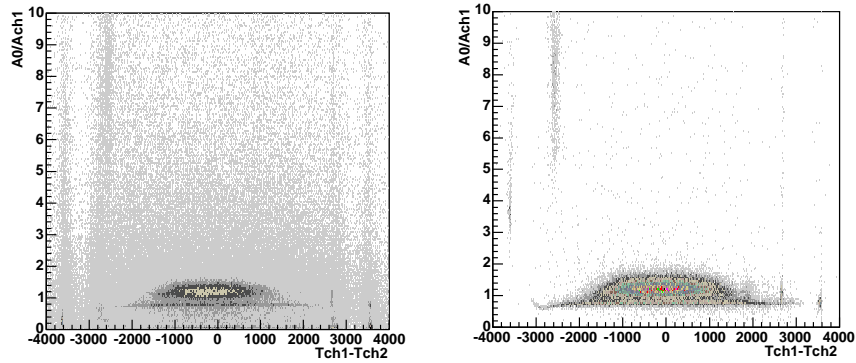

Figure 4.13: *The anode/cathode amplitude ratio is plotted here against the signal position along the delay line, given by the cathode time difference. When we select the low-energy signals (second plot), the correlation between the amplitudes appears clearly.*

very suppressed; only the actual couples of signals produced by fission fragments coming from ^{235}U target remain. The slightly sloped distribution in Figure 4.12 shows the amplitude ratio performance for the *siamese* signals with respect the time difference between the signals. The slope of the correlation is explained by the attenuation of the signal along the delay line. The time difference between the *siamese* signals provides the position of the original signal in the delay line.

4.2.3 Identification of the Gamma Flash signal

Gamma Flash (GF) refers to those gamma rays and relativistic particles produced in the spallation target at the n_TOF facility that reach the Experimental Area before the neutron beam. Although for most detectors this background component is very annoying because they go blind during a while after the Gamma Flash, the PPACs are quite insensitive to it. In fact, the Gamma Flash signal seen by a PPAC does not differ from the signals produced by the fission fragments and its amplitude depends on the proton beam intensity.

The Gamma Flash also presents some particular features that make it a good reference signal: it is the first signal correlated with the neutron pulse, it is present in every detector and, as it takes around 1 ns to travel from the first to the last PPAC, we can consider it as instantaneous. Nevertheless, in a *FADC movie*, it is possible to find a signal preceding to that of the Gamma Flash, this happens because of either the alpha emission of the radioactive targets or the fission fragments originated by neutrons without beam correlation. However, these background signals involve only one or a few detectors, and they can be easily distinguished from the Gamma Flash signals that are produced in all of them. Therefore, a very good discrimination of such contamination is achieved demanding that at least eight detectors are fired simultaneously. The Gamma Flash search algorithm is rather similar to that of the anode coincidences, but has been modified to search for coincidences among the first signals of each anode.

The results obtained by studying the Gamma Flash were used to improve the event-building program. The first improvement is related to the timing of the Gamma Flash signals produced in every detector. By averaging the time differences between the Gamma Flash signals of the anodes over many PS events, we found that the FADC channels presented time offsets among themselves; which were not observed for previous fission campaigns. We realised that before 2003 fission measurements, the whole DAQ had been moved from the Experimental Area to the Escape Line before for safety reasons. Consequently, the electronic paths connecting the PPACs to the Digitizers were
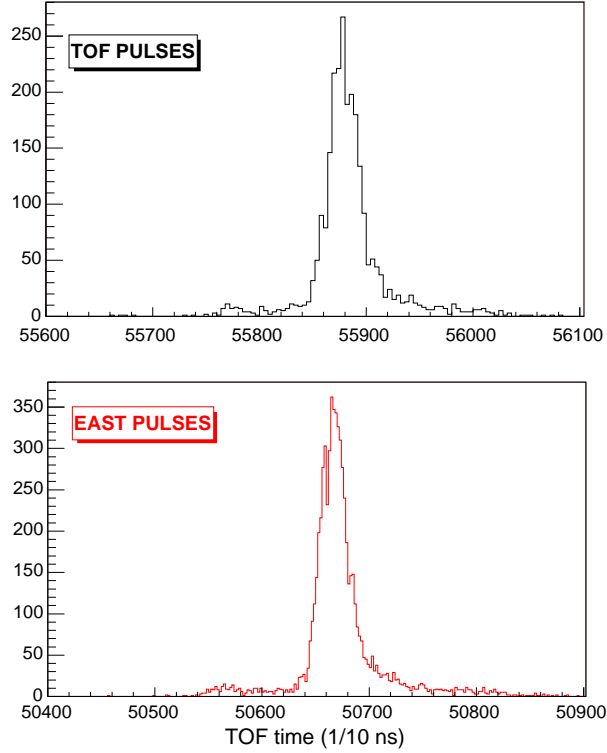
Figure 4.14: *Time distribution of the Gamma Flash signal obtained from PPAC 1 for every PS pulse of the run 5011. The dedicated (TOF) and parasitic (EAST) pulses, with different timing properties, are shown separately.*

drastically increased by more than $10\,\mathrm{m}$ and the previously slight differences among the paths become now observed. The offsets for each anode channel have been calculated averaging over the full set of runs the time differences with respect to the second anode channel, which presented the minimum Gamma Flash average time.

The intrinsic offsets of the anode channels can be corrected to improve the performance of the coincidence search algorithm. If the correction is applied, we get that a strict time window can be used to search for signal coincidences between every pair of detectors. The limits obtained for this unique coincidence window are given by:

$$-80\,ns < T_i - T_{i+1} < 30\,ns \tag{4.2}$$

where T_i and T_{i+1} are the time of signals from adjacent anodes. Times in the right anode (T_{i+1}) are, on average, larger than times in the left anode (T_i) because the fragments reaching the detector on the right must go through the backing, which slows them down.

The Gamma Flash signal also supplies a time reference for each neutron pulse, which is very useful in the energy calibration of the fission events being measured. The gamma flash timing depends on the type of PS pulse: dedicated or parasitic, because the trigger signal supplied by the PS Control Room is different for each pulse type (Subsection 3.1.1).

Finally, the Gamma Flash signals help us to solve the time offset arising when any Digitizer clock shifts with respect to the others. This cumbersome problem is thoroughly explained in the Appendix A.

4.3   Event building software

For practical reasons, we have divided the PPAC analysis in two stages. The first one is an event building routine which provides access to the DST files, builds up the possible fission events for every target and saves them into ROOT format files. This routine was mainly written in C language, although some C++ features were included to enable the ROOT framework capabilities. The second stage analysis software is written in the CINT C/C++ interpreted language [71] and it handles the ROOT files previously created.

The motivation for splitting the analysis is the huge size of the DST files that prevents their transfer to a local computer. Therefore, the event building program must work at a CERN computer; once the ROOT files are obtained, we can work locally after transferring them.

Once the functioning of our detection setup was understood, we developed the definitive event building routine. Information extracted from the previous studies served to improve the efficiency of the event-building program. The algorithm for searching the coincident signals was fine-tuned to find the signals produced by the complementary fission fragments in the pair of detectors adjacent to the fissioning target. In this way, the target is directly identified and all the *configurations* are simplified to type_2.

The following points summarize the event-building program:

Data readout and Gamma Flash part

For a given run, the program accesses the related DST files. Each PS event is temporarily stored in a memory buffer, from where it is read by the different analysis subroutines.

The first task is the time correction of the anode channels according to the offsets obtained by means of the Gamma Flash averaged values (Subsection 4.2.3). Such correction allows us to use a unique coincidence window (Equation 4.2) in a strict coincidence search for all targets.

Then, the Gamma Flash signals are searched for every detector and their average value is calculated for timing purposes. The Gamma Flash information is used to determine if any FADC module has shifted and the program corrects them as explained in Subsection 3.2.5.

Search for signal coincidences

The next step in the analysis program is the search for the coincident *configurations* that exist among the anode signals of the detectors. As in the previous coincidence algorithm, PS event signals are treated detector by detector, but now only the signals with an amplitude larger than a given threshold are considered. The search algorithm takes a signal in a given detector as a starting point and then looks at the next detector in the row for signals inside a window of 40 ns. The same search is carried out from the matching signals and the program proceed until there are no more signals in coincidence or the last detector is reached. All signals found in coincidence are grouped into a list that includes the starting signal. The maximum amplitude signal in the list is then selected and the strict time window given by Equation 4.2 is introduced in order to find the pair of signals produced by complementary fission fragments. This window is applied to the selected signal and the signals on the list that belong to the detectors adjacent to that containing the selected signal. If more than one signal fits the conditions, the larger amplitude signal is chosen. The *configuration* is discarded if the starting signal does not form part of it; in this way, we can assign the *configuration* directly to the target on the right of the current detector. If the *configuration* does not include the starting signal, it will be considered at a later time, the two signals found are removed from the list and the program looks inside the remaining signals on the list for the highest amplitude signal, repeating the procedure until a valid *configuration* is found or the list ends. Eventually, if the search is successful, we get a type_2 *configuration* that includes the starting signal and another signal belonging to the detector on the right. If not, the starting signal is discarded and the program repeats the full procedure for the next signal in

the row. The signals on the list which have not been included in an accepted *configuration* are available for next searches.

Search of the cathode signals

For every *configuration* found, now consisting of two signals from adjacent detectors, we must determine the position of the fission fragments crossing both detectors. Therefore, we need to find two pairs of cathode signals for each anode signal. The couple of signals of one cathode must have the same origin, the so-called **siamese** signals. The search procedure is repeated for each cathode as follows:

- Starting from the anode signal, a time window is open ranging from the anode time to the anode time plus 400 ns in order to look for signals from both cathode channels inside. These limits take into account that the maximum delay introduced by the delay line is given by its total length (around 320 ns).

- Then we check which signals pairs fulfill the diagonal condition as we explained in the Subsection 4.2.2. At this stage of the analysis, the limits required for the diagonal condition are quite tolerant and they are common for all the cathodes: 330 ns <DLT< 400 ns. These limits, determined by the previous analysis, include the time spent in the connections between the delay line and the preamplifiers, which is the reason why we obtain values larger than the delay line. In case that more than one couple of cathode signals fulfills the condition, all are kept.

- In an attempt to be more restrictive in the cathode signal selection, additional conditions are demanded of their amplitudes. As shown before, the amplitudes of the *siamese* signals are very similar because they come from the same cathode signal. Therefore, if a signal amplitude is twice larger than the other, the pair is discarded. An amplitude threshold is set for the cathode signals, as it was for the anode signals.

- Finally, the couple or couples of signals remaining are stored together with the anode signals and the other cathode signals. Additional information is supplied about the multiplicity found for each cathode. If no valid pair is found, a dummy pair is supplied with times and amplitudes equal to zero.

Saving the *configurations*

Once the cathode search is finished for one *configuration*, this is saved in a ROOT file. In the ROOT files, the *configuration* is stored in a *TTree* class labelled with the label of the target between the detectors that contain the *configuration* signals. At this level, the multiplicity for the cathode signals can be higher than 1, so that we can have several possibilities for each cathode. The ambiguity introduced is resolved in the next step of the analysis.

ROOT *Ttree* classes allow us to store large amounts of data while maintaining the accessibility by means of the *TBranch* classes. In the event building software we have defined five branches: one for the general pulse information and the anode signals, called the *event2* branch, and one branch for each cathode, named with the cathode names (x_0,y_0,x_1,y_1). The *event2* branch contains the event number, the beam intensity, the calculated Gamma Flash time and the times and amplitudes of both anode signals in the *configuration*. Every cathode branch contains the times and amplitudes of both signals which, for historical reasons, are referred to as *direct* and *reflected* signals.

At this point, we have the ROOT files containing all the *configurations* found which are candidate for fission events. The data reduction process at the ROOT file level is described in the next section.

4.4   ROOT file data reduction

The ROOT files created by the event building routine are compact enough to be transferred from CERN to a local computer and the second stage of the data reduction is developed within the ROOT framework. This part of the analysis is written for the ROOT CINT (ROOT C interpreter).

Up to this point, data from all the targets have been stored together and managed in the same way. From this point on, each target is treated separately. We use the *Ttree* method MakeClass which creates a class that loops over the tree entries one by one. This class is expanded to include our own analysis, in which each entry contains full information about a *configuration*.

As we are not able to reconstruct the fission event when any of the cathode positions is missing, the *configurations* in which any of the cathodes has no valid signals (times and amplitudes equal 0) are discarded. The possible valid fission events rejected by this cut are accounted by the detector efficiency as explained in Chapter 5.

A further selection at the anode signals is then done by means of a contour cut in the two-dimensional histogram obtained for the anode time difference

against the amplitude of the first anode (the anode of the detector on the left). This amplitude has the highest average value because the fission fragment reaches the detector without crossing the backing. The contour cut is given by the expression:

$$(AMP0 - C) * CS + (T0 - T1 - B) * SN + C <$$
$$< A * ((T0 - T1 - B) * CS - (AMP0 - C) * SN)* \qquad (4.3)$$
$$* ((T0 - T1 - B) * CS - (AMP0 - C) * SN) + C$$

where the curve parameters A, B, C and α have been obtained for the different sets of runs and targets and CS and SN are expressions in the cosine and the sine of the α parameter, respectively. The effect of this cut is shown in Figure 4.15. Practically all the remaining low-amplitude noise is suppressed with this cut.
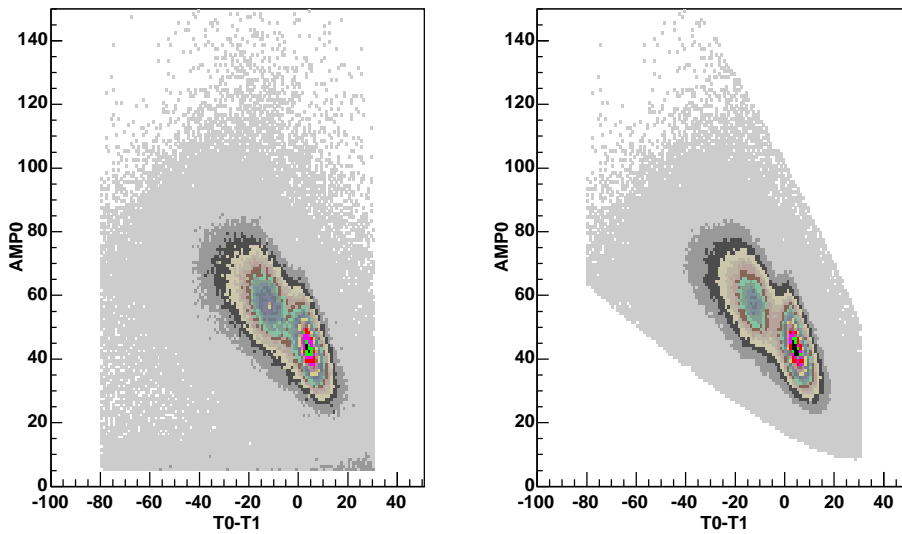
Figure 4.15: *The distribution of the time difference between anodes versus the amplitude of the anode on the left is shown before (left) and after (right) applying the contour cut for the Target 1 data.*

4.4.1 Reconstruction of the fission fragment trajectory

The remaining selection process is based on the cathode signal performance with the aim of reconstructing the fission fragment trajectories. In the first part of the data reduction process we allowed some multiplicity for the cathode signal choice. As the fission fragment trajectory is unique, we have to identify which pair of cathode signals is produced by each fragment. Therefore, stricter limits are required for the diagonal condition and for the amplitude ratio condition to solve the multiplicity. These limits strongly depend on the cathode and also vary slightly with the fission fragment origin: whether it originates from the target on the right or the left of the cathode. If any ambiguity still remains an additional condition on the ratio between the cathode and anode amplitudes determines the best choice.

Nevertheless, these restrictive conditions do not exclude those *configurations* in which all the signals of any of the cathode are suppressed. In the case that any of the required conditions rejects all the possibilities, the closest one is selected. *Configurations* without cathode multiplicity are directly considered in the same way.

Once the cathode multiplicity is resolved, fission fragment trajectory can be reconstructed. The first step consists in the position calculation in every cathode. For this, two approximations are assumed: that a signal produced at the delay line mid-position reaches both preamplifiers at the same time and that the delay introduced by the electronics is much smaller than that of the delay line. Under such conditions, the delay line mid-position corresponds to a time difference equal to 0 and the time difference between *siamese* signals in a cathode is proportional to the position in the delay line where the signals were produced. The time/lenght proportional coefficient is given by the intrinsic delay of the delay line that has been measured at the laboratory for each delay line.

As the nominal length of the delay lines is 200 mm, all the *configuration*s with any position value exceeding this dimension are rejected.

Having calculated the positions in the four cathodes, we can reconstruct the trajectories of the fission fragments, taking into account that they are emitted from the target in opposite directions in the center-of-masses. This assumes that the nucleus fissions at rest what is true for low and intermediate neutron energies, but at energies comparable to the kinetic energy of the fission fragments, around 100 MeV, the linear momentum transfer correction must be considered. The trajectory is fully determined by the target position where the fission occurs and the emission angle with respect to the neutron axis beam, θ. For practical reasons, we refer to the angular distribution of the fission

fragments by the cosine of θ.

From the setup geometry, the coordinates of the fission origin in the target are obtained as follows:

$$X_{targ} = x_1 - (x_1 - x_0)\frac{\frac{anode\_sep}{2} - cath\_anode\_sep}{anode\_sep} \tag{4.4}$$

$$Y_{targ} = y_1 - (y_1 - y_0)\frac{\frac{anode\_sep}{2} + cath\_anode\_sep}{anode\_sep} \tag{4.5}$$

where x_0, y_0, x_1 and y_1 are the X and Y cathode position in mm at the detectors to the left and right of the target, respectively; *anode_sep* is the separation (34.2 mm) between detectors and *cath_anode_sep* is the separation (3.2 mm) between the central anode and both surrounding cathodes in a PPAC. An additional cut is then included to reject the *configurations* in which the reconstructed origin position falls outside the target area.

The $\cos(\theta)$ is calculated from the expression:

$$\cos(\theta) = \frac{anode\_sep}{\sqrt{(x_1 - x_0)^2 + (y_1 - y_0)^2 + anode\_sep^2}} \tag{4.6}$$

4.4.2   Neutron energy estimation

The energy of the impinging neutron is calculated by its time-of-flight using the difference between the anode times and the Gamma Flash time of the pulse. In Appendix C, it is explained how the path length depends on the neutron energy due to the moderation inside the lead target and the moderator. This means that we have to apply a energy-dependent correction in the initial value of the path length.

Finally, the definitive fissions *configurations* are saved and displayed in the appropriate histograms which show directly the data reduction results.

Chapter 5

Fission cross-section analysis

Measuring absolute values of neutron-induced fission cross sections is a very complicated task. In our approach, we will limit ourselves to produce relative measurements, taking advantage that two samples used as standard references in fission reactions have been included among the targets placed simultaneously under the same neutron flux. For a surface unit centered on a given location (x,y) and a given energy interval (E), the number of fission events that our experimental setup is actually registering per target area can be written as:

$$n(x, y, E) = \varphi(x, y, E) \ \rho(x, y) \ \sigma_f(E) \ \varepsilon(E) \tag{5.1}$$

where:

σ_f is the fission cross section,

φ is the neutron flux in number of neutrons per surface unit for the given energy interval,

ρ is the target surface density (number of nuclei per surface unit),

ε is the efficiency in the detection of the fission fragments.

Let us consider a surface unit small enough to have both the neutron flux, φ, and the target surface density, ρ constant. It has been demostrated by simulations[1] that the neutron flux attenuation due to the full PPAC setup - including targets, backings, detectors and kapton windows - is less than 1%. Therefore, the flux ratio between two targets $[\varphi^a(x, y, E)/\varphi^b(x, y, E)]$ can be taken as the unit and we can write:

---

[1]The flux attenuation calculation is described in Laure Ferrant's thesis work [65]

$$\frac{\sigma_f^a(E)}{\sigma_f^b(E)} = \frac{n^a(x,y,E)}{n^b(x,y,E)} \ \frac{\rho^b(x,y)}{\rho^a(x,y)} \ \frac{\varepsilon^b(E)}{\varepsilon^a(E)} \tag{5.2}$$

where the target labelled as b must be one of the reference targets - in our case the ^{235}U and the ^{238}U samples - for which the fission cross section, $\sigma_f(E)$, is accurately known.

The surface densities of the targets were measured at IPNO [72], so that here we are dealing with the other two terms: the numbers of recorded fission events, obtained through the data reduction procedure described in Chapter 4, and the ratio of the efficiencies, which must be estimated.

In the following sections we will explain the procedure we followed for estimating the efficiency for every target and then we will focus on the neutron flux performance as seen by the PPACs.

5.1   Efficiency calculation for the PPAC setup

There are several factors that limit the fission-event detection efficiency of the n_TOF PPAC setup. They come from very different origins that will be discussed throughout this section. In order to obtain the cross sections that we are looking for, it is important to know how the efficiencies and their ratios depend on the neutron energy.

5.1.1   Geometric efficiency

The geometric acceptance of our detection setup is an evident factor that reduces the efficiency. The geometric efficiency has been obtained by means of a simulation, that reproduces schematically the actual setup geometry. The simulated setup consists of two square-shaped PPAC detectors with a sensitive area of $20 \times 20 \, \text{cm}^2$, equidistant from the central circular target which has a diameter of $8 \, \text{cm}$. Just for this simulation, let us assume that the two complementary fission fragments are emitted isotropically in opposite directions. Thus a particle generator that launches fission fragments from a random position inside the target following an isotropic angular distribution is a good approximation to the fission events.

The results, shown in Figure 5.1, imply that the geometric efficiency is $100\,\%$ for the fragments emitted at angles smaller than $74°$ and it drops to zero for higher angles, being $82°$ the maximum emission angle accepted for this geometry.
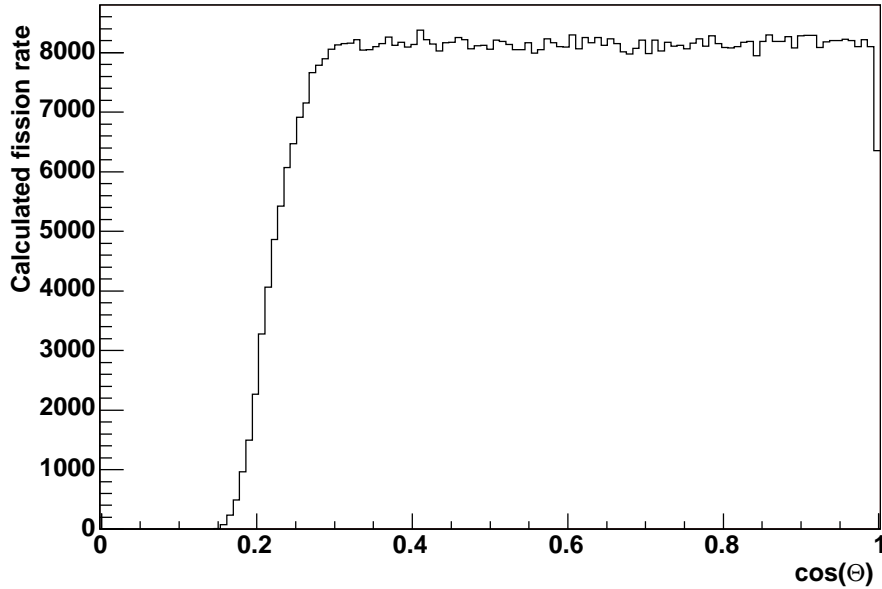
Figure 5.1: *Simulated cosine distribution for a FF isotropic distribution in the PPAC setup calculated by using a Monte Carlo program based on GEANT4 [73].*

5.1.2 In-medium fission fragment absorption

Another factor that significantly diminishes the PPAC efficiency is the energy lost by the fission fragments in the different layers of matter that they must pass through. If one of the fragments has not enough kinetic energy to reach the two gas gaps in the detector producing signals in every electrode, we will not be able to reconstruct the full fission event and it will be missed. The efficiency reduction due to the energy lost by the fragment and its absorption depends greatly on the emission angle: the higher the angle, the longer is the path through the successive layers of matter; the absorption probability increases and, consequently, the possibility of reconstructing the fission event decreases. For the same path, the heavy fission fragments (HFF) are much more affected than the light fission fragments (LFF) because they have higher Z values (Bethe-Bloch's formula predicts that the heavy charged particles stopping power depends on Z^2) and their initial kinetic energy is smaller. In addition, the situation is worse for those fission fragments having to go through the $2\,\mu$m thick aluminum backing before reaching the PPAC active
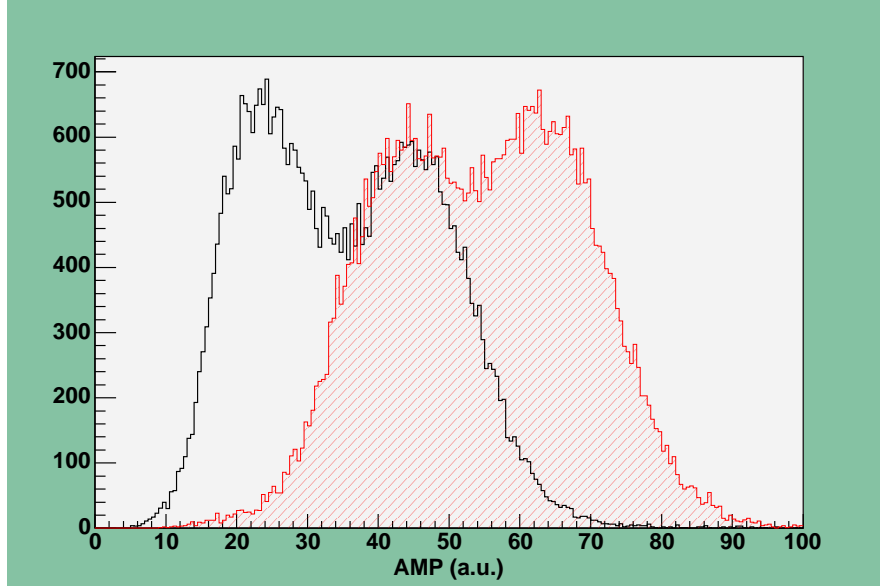
Figure 5.2: *The amplitudes(AMP) measured by PPAC 1 anode for the ^{234}U fission events from neutron energies around 5 MeV and emission angles about 40° are shown. The filled histogram reproduces the amplitudes of the fragments coming from the target on the right and the empty histogram shows those fragments coming from the target on left, which have to go through the backing. The average amplitude measured for the fragments crossing the backing is substantially less due to the energy losses on it.*

volume (see Figure 5.2). In consequence, those fission events in which the heavy fission fragment goes through the backing are more suppressed, thereby determining the reduction in the detector efficiency; cases were the light fission fragment crosses the backing are less critical.

A simulation work has been done with the SRIM software package [74], in order to estimate how the energy loss in the different layers of material affects the PPAC efficiency with respect to the emission angle. We have studied the transmission of a few typical HFFs through the target, the backing and two of the PPAC Mylar layers. The energy assigned to the fission fragments is calculated from the total kinetic energy released [35]. The results are shown in Figure 5.3, together with a similar simulation provided by the IPNO group, where different thresholds in the fission fragment kinetic energy were taken into account. According to the simulations, we can see that the HFFs emitted at polar angles smaller than about 55° can be fully recorded. For higher an-
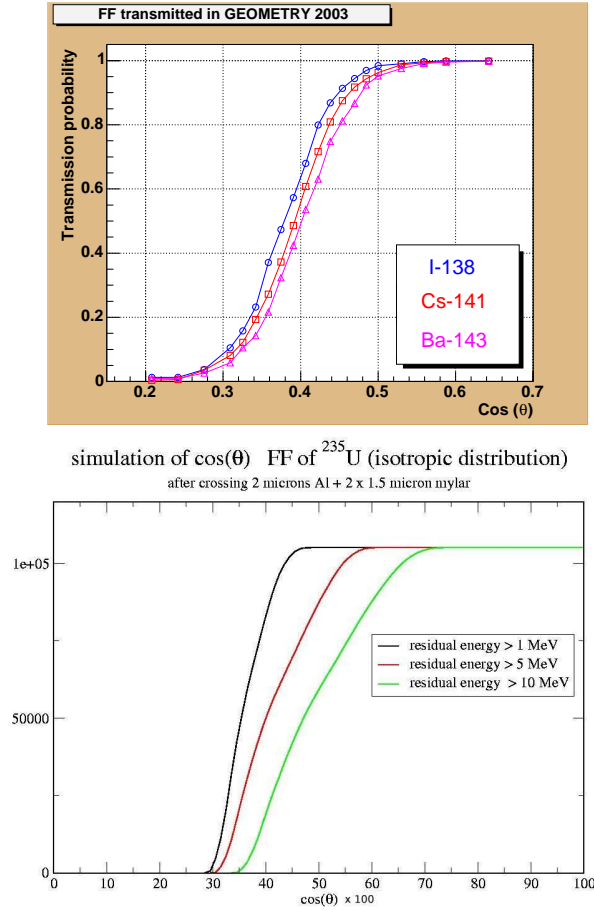
Figure 5.3: *Results obtained for the transmission, at different angles, of different HFF through the backing and half PPAC simulated with TRIM (first plot). The second plot shows the IPNO results when different thresholds for the remaining FF kinetic energy are required.*

gles, the probability of a FF being stopped increases steadily up to $75°$, angle at which the probability of registering a HFF is almost zero. This means that the efficiency reduction due to the HFF absorption actually limits the acceptance angle to a value lower than the one imposed by geometry. Moreover, if we were to establish a minimum residual energy for the fission fragment, in order to produce a signal large enough to be considered in the analysis, the maximum angle with full acceptance could be reduced to approximately $50°$ ($\cos(50°) = 0.65$).

5.1.3   Amplitude threshold cut

In order to avoid registering too many noise signals and filling the FADC buffer memory, a certain amplitude threshold must be set for every FADC channel. This means that, even if both fragments reach all the electrodes in the involved detectors, their signals may not be registered if the amplitude is under this threshold. For each channel in the setup configuration, the threshold settings are specified at the beginning of the run together with the Full-Scale and Offset parameters. Every time there was a change in the detector setup, a test run was taken in order to check signals from a few PS events and to extract the best thresholds for each channel which discriminate the true signals from noise. This task must be done channel by channel because:

1. Different detectors have different high voltages, so that the height of the fission signals may vary from one to others.

2. The signal shape is different for cathodes than for anodes because of the delay line and the different preamplifiers (see Chapter 3).
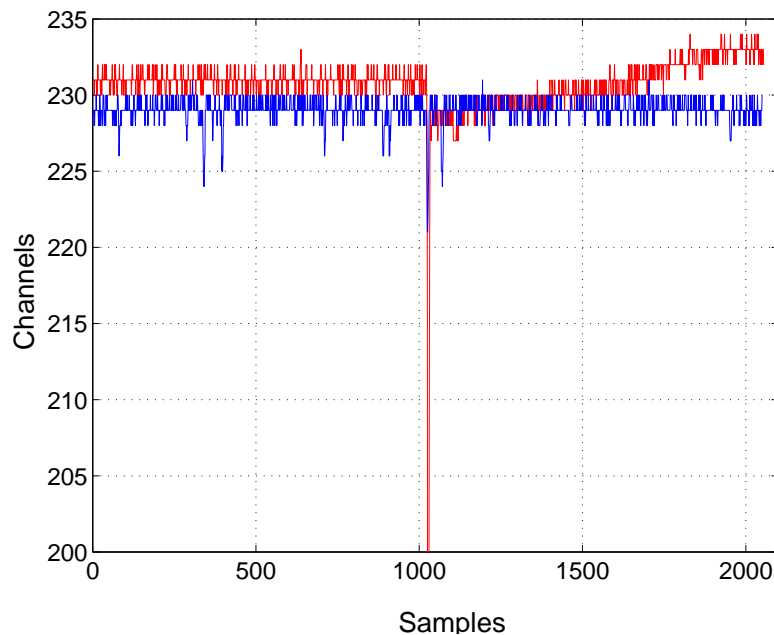
Figure 5.4: *Two signals from different anodes show how the baselines are located at slightly different positions.*

3. The position of the signal baselines in the FADCs can substantially change from one channel to other (see Figure 5.4), especially for the cathode channels. This variation affects the threshold selection because the amplitude of the signal must be compared to the height of the threshold with respect to their signal baseline (effective threshold).

The FADC works at 8-bit resolution, so that we have 256 amplitude channels for the full-scale range. The FADC gain is set in such a way that the full-scale corresponds to $0.5\,\text{V}$, while the offset is around $200\,\text{mV}$. With this configuration the baseline comes around the amplitude channel #230 for the anodes, while for the cathodes ranges from #225 to #234.

Looking at the hardware thresholds which have been used for the same run, we notice that the value threshold-minus-baseline ($< Th - BL > \sim 10$) varies a lot among cathodes, being for a few channels (16, 18, 22 and 45) higher than usual ($Th - BL = 13$, 16, 14.5 and 17.5, respectively). Such large thresholds, produced by baseline drifts, have a huge impact in the suppression of those fission fragments producing low-amplitude signals. This effect, that is referred to as *hardware threshold cut*, will be explained with more details in Section 5.2.

5.1.4 Angular distribution of the emitted fragments.

Until now, we have worked assuming an isotropic fission fragment distribution. But this is not the actual case and important angular anisotropies arise for neutron energies at the first or the second fission chance threshold. These anisotropies seriously affect the efficiency of our experimental setup due to its higher efficiency at forward angles.

The angular distribution of the fission fragments is included in the analysis by means of an anisotropy factor B which can be experimentally determined, as will be explained in Section 5.3. For each energy interval, the angular distribution is approximated by:

$$W(\theta) \propto 1 + B\,cos^2(\theta) \tag{5.3}$$

where θ is the angle measured with respect to the beam axis.

We also had to take into account that the impinging neutron transmits all or part of its linear momentum to the fissioning nucleus. In the case of high energy neutrons, the effect of the linear momentum transfer (LMT) is that the folding angle between both complementary fission fragments in the laboratory frame is no longer equal to $180°$. A discussion on this topic is

found in Appendix B, that shows how our particular geometry compensates this effect in such a way that no corrections are needed in a first approach.

5.1.5 Pile-up and noise effects

The previously mentioned points deal with the reduction of the maximum angle for which the PPAC is supposed to have full efficiency. However, there are two other factors that produce a loss of fission events at small angles:

- electronic noise coming from the temporarily sparkling of the detector when the ionisation density is high at the beginning of the neutron bunch, that masks the fission signals in the involved detectors (see Figure 5.5),
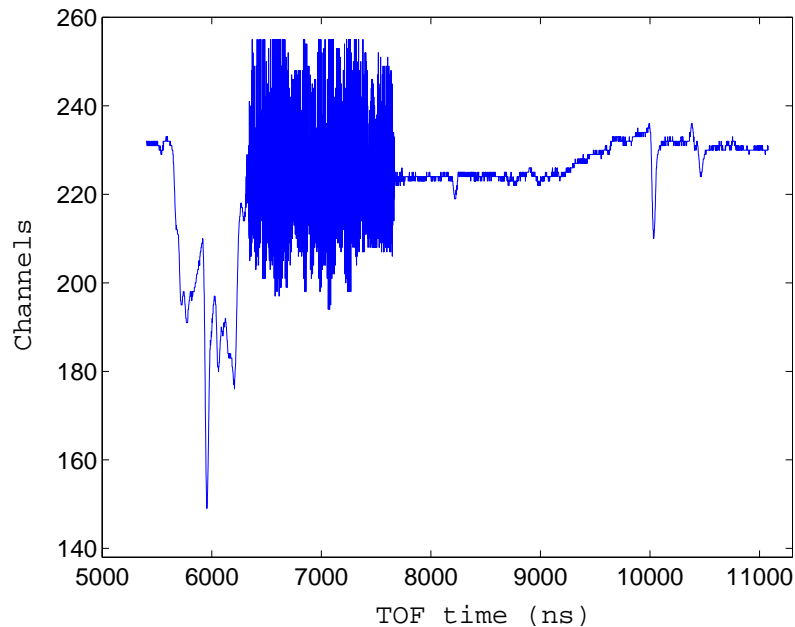
Figure 5.5: *A cathode channel showing too much electronic noise. Eventual true fission signals coming around 7000 ns are masked by the noise*

- high counting rates, that increases the signals missed because of pile-up.

Both factors become significant as neutron energy increases and we have times-of-flight near the Gamma Flash. The pile-up is assumed to be quite similar for the different targets, because their fission rates are very close at

very high energy. The noise problem has been mitigated by reducing the voltage of the noisy detectors and by the filtering applied to the raw signals which depresses the high frequencies, thus greatly decreasing the number of affected PS events. A more detailed study of them is foreseen in order to weigh up their influence in the counting rate at very high neutron energies.

5.2 Hardware threshold cut

Some of the cathode channels have a hardware threshold which turned out to be too high, so that they do not register those fission signals with amplitudes falling under this threshold. Therefore, the counting rate of the involved targets needs to be corrected.

The consequences of the hardware threshold cut has been studied target by target. For a given fission fragment, the signal amplitude depends on the detector high voltage and the relative position of the detector with respect to the fissioning target (different paths of a fragment imply different energy losses in the interposed material and thus different signal amplitudes).

What is common for all the involved targets is that the hardware threshold cut is not present at high energies, as can be seen comparing the results obtained for the cathode signals amplitude at low and high energies (Figure 5.6). This behaviour can be explained taking into account how the DAQ works: for short times-of-flight the counting rate is so high that the probability of signals coming together closer than the length of the signal frame is very high. The length of a signal frame is essentially given by the sum of pre-samples and post-samples which is equal to 1024×2 for PPAC channels, equivalent to $4\,\mu$s in time units. The performance of a FADC channel for times near the Gamma Flash can be observed in Figure 5.5: the raw data zero-suppression begins after $11\,\mu$s, that correspond to a neutron energy of a few MeV and all the signals arriving before the beginning of zero-suppression are registered by the DAQ, even when their amplitude is below the threshold. Therefore, the hardware threshold cut only needs to be corrected for neutron energies below a few MeV. This is the reason why, for the ^{238}U with a fission threshold around 1 MeV, the hardware threshold has no effect in the counting rate and no correction is required.

In Figure 5.7, we can see the signal amplitudes grouped around two values, corresponding to the cases of a light or a heavy fission fragment reaching a given detector. The heavy fission fragments produce a lower amplitude signal in the PPAC, so that these signals are more often suppressed. In order to correct the hardware threshold cut we divide the signals in two groups
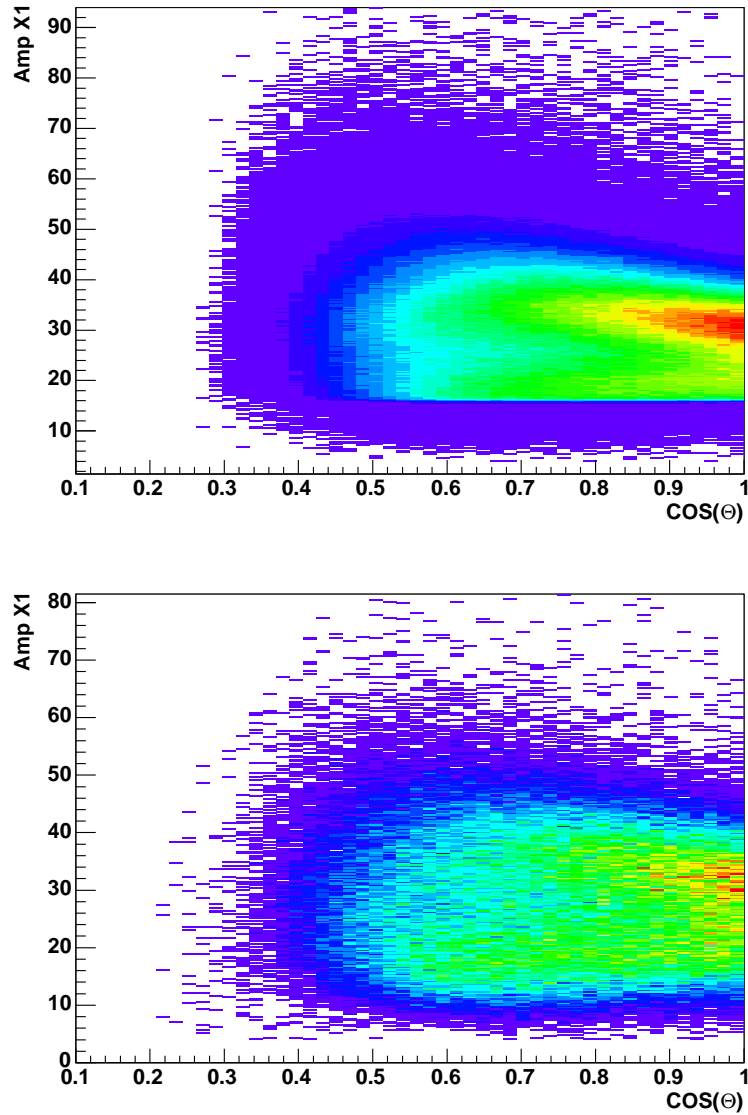
Figure 5.6: *Histograms showing the cathode signal amplitude (Amp X1) versus the emission angle (cos θ) for fission events in Target 7 (^{235}U) produced at neutron energies below 100 keV (top chart) and at energies between 1 and 10 MeV (bottom chart). Whereas, for low energies, the hardware threshold cut appears clearly below the amplitude 17, for MeV energies the hardware threshold cut is not observed .*

according to the mass of the fragment that originates the signal. The best amplitude separation between both groups was obtained when looking at the anode of the second detector, the one facing the backing.
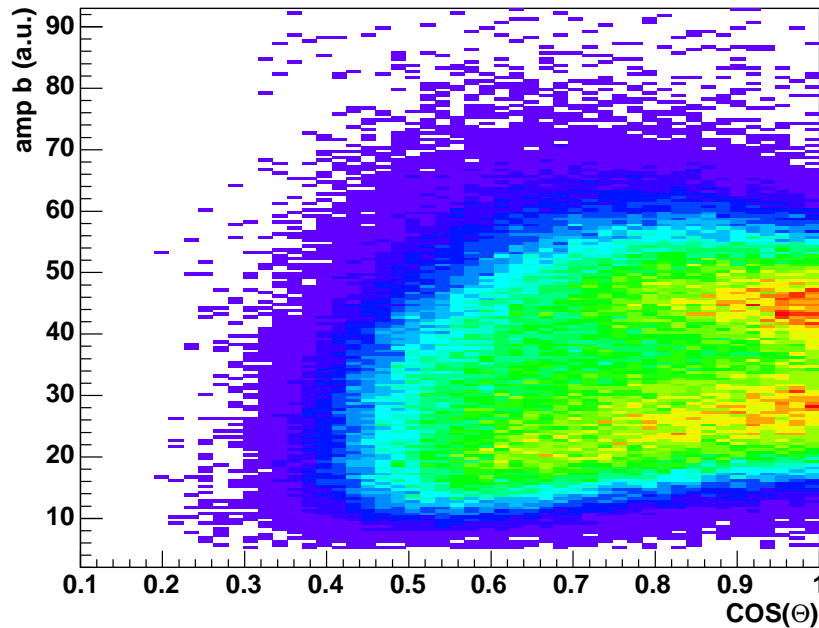
Figure 5.7: *The signal amplitude of the second anode (AMP B) is represented against the angle cosine (cos θ). The two fission fragment groups around amplitude values of 42 and 26 can be clearly distinguished, with the heavy group giving the lower amplitudes.*

Apart from the signal amplitudes which depend on several detector and fission fragment characteristics, it is usually better to use the time differences between the two complementary fission fragments to determine to which group they belong, because the time difference between both fragments is directly related with their velocity differences and, thus, with the FF kinetic energies (eq. 2.2). In spite of the short flight paths between target and detectors, the PPAC time resolution is usually good enough to distinguish which direction followed each fission fragment (Figure 5.8).

If the detection efficiency for both fission types were the same, the number of events of both types in a given cosine interval should be the same. Therefore, studying the ratio between the registered heavy and light fragments for those
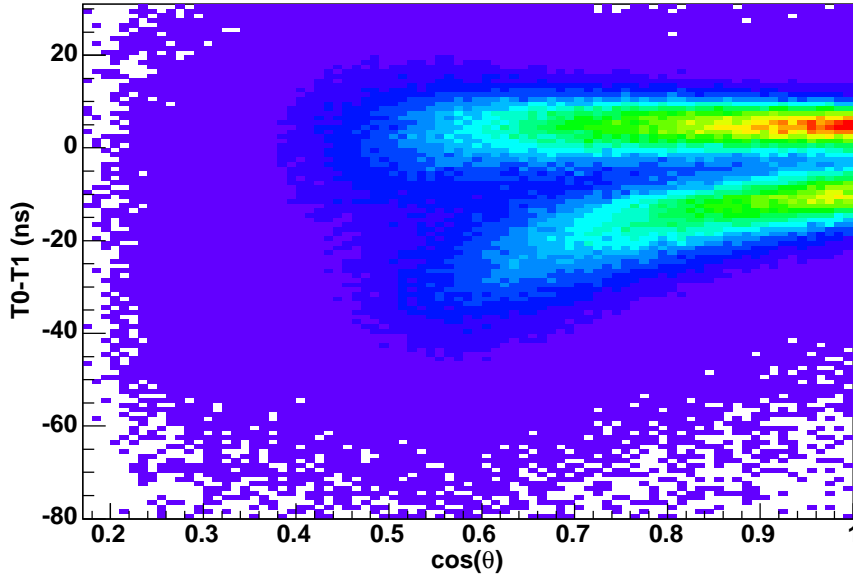
Figure 5.8: *Time difference between fission fragments from Target 0 vs. the emission angle cosine.*

detectors having a too high amplitude threshold, the influence of the hardware threshold cut in the counting rate can be estimated.

^{235}U target

The ^{235}U sample corresponds to Target 7 in the PPAC setup (Figure 3.7). Within the FADC channels involved, the channel # 45 – connected to the horizontal cathode of the detector facing the backing of this target – has a too high threshold. Actually, it presents the highest effective threshold found in the settings, so that the threshold cut is very stringent, suppressing a significant portion of the signals produced by HFFs (see the top chart in Figure 5.6).

In addition, the resolution for the time difference between complementary fragments is worse than for the other targets because the anodes of the detectors involved were connected to different Digitizers. An additional time spread seems to be produced by internal clock differences between both Digitizers, which cannot be corrected by the calibration procedure. This effect can be observed by comparing the Figures 4.6 and 4.7: for Target 7 histogram the
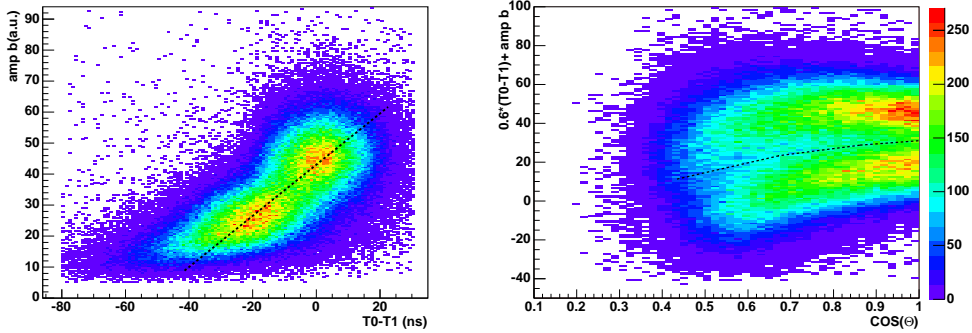
Figure 5.9: *The left 2-D histogram shows the time difference between anodes (T0-T1) vs. the amplitude for the second anode (AMP B); the axis crossing both maxima is drawn with a dashed line. In the right histogram the variable related to the projection onto this axis is represented against the emission angle cosine.*

two humps corresponding to light and heavy groups are not resolved. So the separation between both signals groups (LFF and HFF) is not fully achieved, either by time difference between fragments or by signal amplitudes. We decided to use together both time and amplitude information in order to get a group separation as good as possible (see Figure 5.9).

If we project the time difference – amplitude histogram onto the axis which is represented in the Figure 5.9 by a dashed line, we obtain the variable: $AMP\,B + 0.6 \times (T0 - T1)$ which produces histograms like that of Figure 5.10, which reproduce better the shape of the FF kinetic energy distribution.

An estimation of the proportion of both fission fragments groups depending on the neutron energy has been obtained by fitting their distributions. The variable obtained from the projection fits a sum of two Gaussians, in which the area under each Gaussian function is related to the number of each fission fragment group (LFF and HFF).

In the energy range between 1 and 4 MeV, where the hardware threshold cut is negligible and an asymmetric mass FF distribution is expected, we obtain similar values for the Gaussian areas, indicating that the low-amplitude HFF are hardly suppressed. However, at lower neutron energies, the HFF peak becomes smaller, because the suppression by the hardware threshold becomes significant. Many low-amplitude signals from HFFs fall below the hardware threshold and are not registered by the acquisition system.

Apart from the neutron energy, the FF distribution shape and the area ratio between both groups depends on the emission angle and, therefore, an
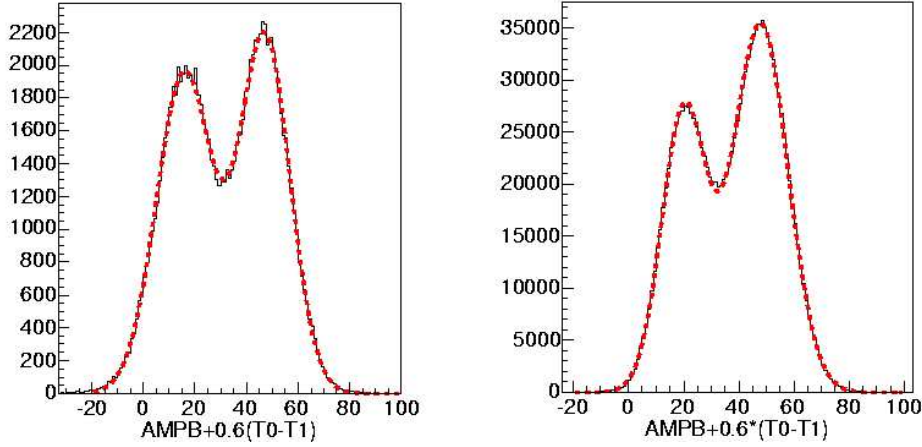
Figure 5.10: *An attempt to reproduce the FF mass distributions has been done with the information obtained from the fission events. Each peak corresponds to a FF group: LFF, the one with higher amplitude values and HFF, at lower amplitudes. Only fission events with a cosine larger than 0.8 have been selected. In the first histogram, fissions in the energy range from 1 to 4 MeV are considered; the ratio between the areas below the peaks obtained from the Gaussian fit (the dashed line) is approximately equal to 1. The distribution for energies below 1 keV is shown in the second histogram and the previously defined ratio is now around 0.6 in favour of the LFF group.*

angular dependency must be considered in the correction. In consequence, we have studied the FF distribution by grouping it into several cosine intervals. At this point, we have estimated from the fits of the distributions the total number of LFF for each cosine and energy interval. Taking into account that fragment absorption reduces the fission event acceptance for angles larger than $50°$, we can assume that, for smaller angles, the calculated number of LFF should be equal to the actual number of LFF reaching one PPAC, where it represents half of the total number of fission events we should detect. Therefore, we can take twice the LFF number as a reliable estimation of the total number of fission events in the ideal case of there was not hardware threshold cut. At high energies, this number is close to the number of events we actually detect; while in the low energy range the ratio between the detected and the predicted number of events gives a good estimation of the events suppressed by the threshold cut.
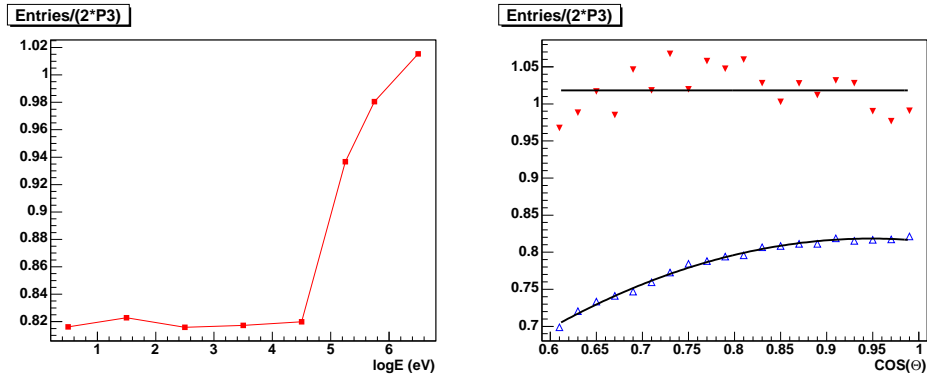
Figure 5.11: *The ratio between the measured and the calculated fission events depending on the energy (left chart) and on the $\cos(\theta)$ (right chart). In the second plot, the filled triangles represent the high energy events, whereas the empty triangles represent those with low energies.*

The behaviour of this ratio has been studied for several energy and cosine intervals. When studying small angles, the ratio between detected and expected events is close to 1 at MeV neutron energies; however, the ratio falls to 0.8 for lower energies and then it does not change with the energy, so we have grouped the events below 10 keV to study the angle dependence. The ratio behaviour with the angle cosine is flat around 1 for MeV energies, whereas, for low energies, it fits reasonably well to a second order polynomial: $-\cos^2(\theta) + 1.89 \times \cos(\theta) - 0.08$, which is shown in Figure 5.11. Once we have parameterized the threshold cut effect, it can be included as a known factor in the efficiency calculation.

^{234}U targets

The ^{234}U samples correspond to Target 0 and Target 1 (Figure 3.7). Target 0 behaves similarly to Target 7: channels 16 and 18, that correspond to both cathodes facing the target backing, have too high thresholds, thus a part of their low-amplitude signals are lost. However, for both ^{234}U targets, the procedure is simpler than for ^{235}U because the complete separation between light and heavy fission fragment groups can be achieved by means of time-of-flight information (see Figures 5.8 and 5.12).
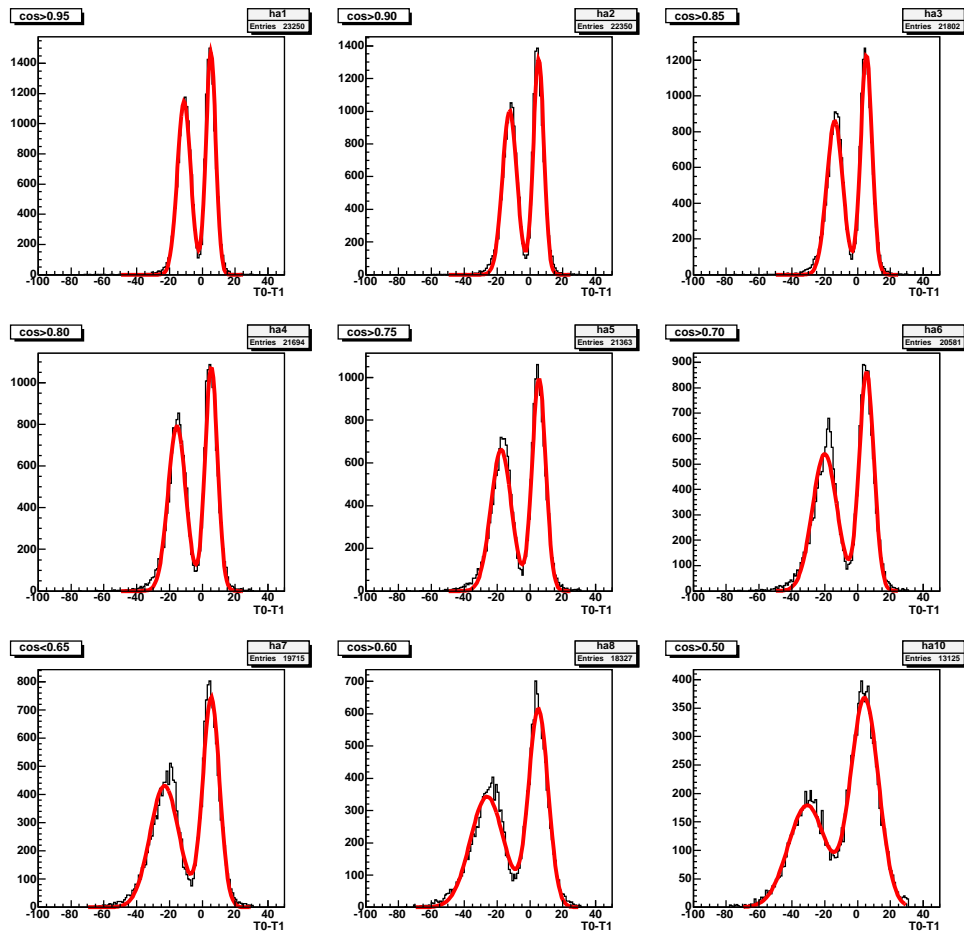
Figure 5.12: *Time-difference distributions from high-energy fission events in Target 0 obtained for different angle cosine intervals. Light and heavy fragment groups are fully resolved and the distribution shape depends on the FF emission angle.*
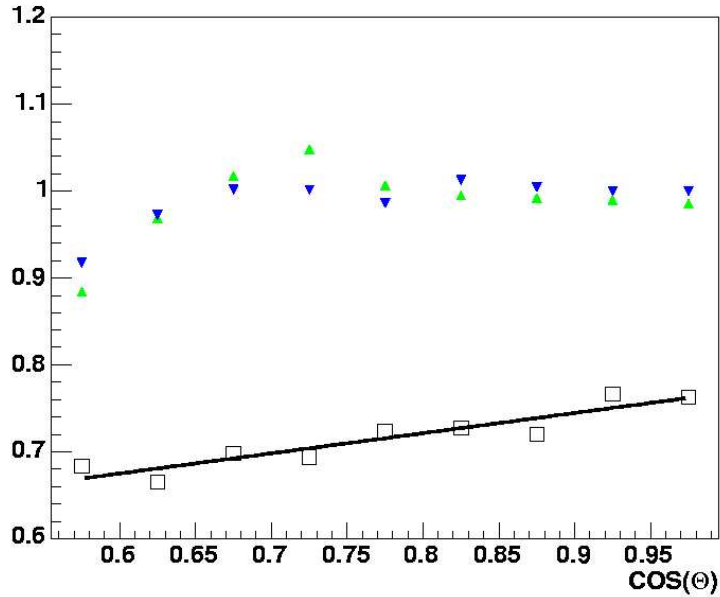
Figure 5.13: *Estimation of the inefficiency due to the hardware threshold cut for Target 0. The square markers represent the grouped data for low neutron energies compared to light and black triangle markers which correspond to energies 8-14 MeV and 2-8 MeV, respectively.*

For ^{234}U, the fission rate at low energies is much smaller than for ^{235}U, so all the events below the fission threshold (neutron energy below 200 keV) have been grouped together to get enough statistics to study the hardware threshold cut.

The results are shown in Figure 5.13. For Target 0 the threshold cut produces, at low energies, a 70 % decrease in the efficiency with respect to the counting rate at high energies. These conclusions were obtained for angles smaller than 50° ($\cos(\theta) > 0.6$), the acceptable angular range considered for efficiency determination. The efficiency behaviour with the cosine at low energies is fitted by the curve $0.54 + 0.23 \times \cos(\theta)$.

For Target 1, in both surrounding detectors, any of the cathode channels has a threshold higher than the average value. However, we checked that these thresholds are not high enough to suppress significantly the low-amplitude signals, because there is no evident cut in the cathode signals. The ratio between the measured and the estimated number of events is around 1 at both high and low energies (Figure 5.14), confirming the negligible effect of
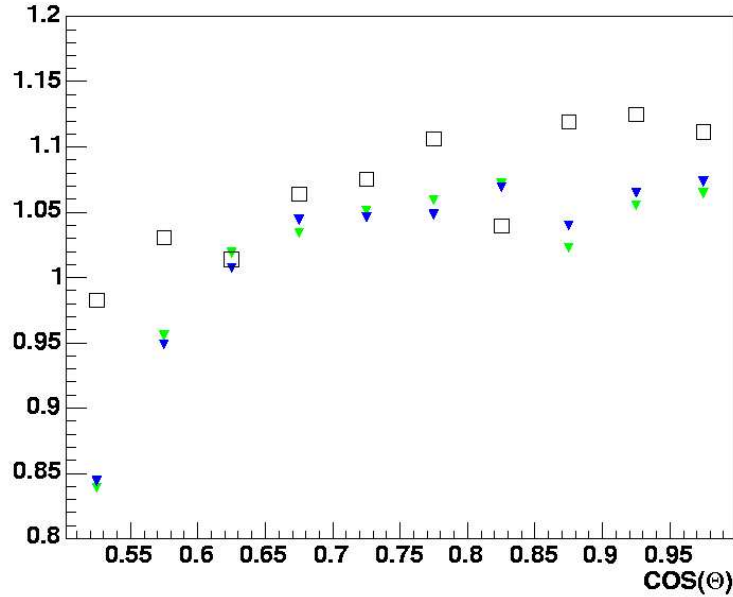
the hardware threshold cut in this case.

Figure 5.14: *Estimation of the inefficiency due to the hardware threshold cut for Target 1. The square markers represent the low energy events grouped, whereas both type of triangle markers represent high energy events.*

5.3   Anisotropy measurements

Another factor that influences the detection efficiency is the fission fragment angular distribution (FFAD). At certain energies, the FFAD differs significantly from the isotropy and must be included in the detection efficiency estimation of any experimental setup with a restricted angular acceptance. That is the case of the PPAC setup where the angular acceptance is limited because of the fission fragment absorption in the detection setup materials.

As the PPAC setup is designed to reconstruct the fission fragment trajectories and hence to determine their emission angle, it is possible to know the FFAD from PPAC measurements and to include it in the detection efficiency estimation. However, the actual situation is far more complicated because the $\cos\theta$ distribution we obtained from PPACs differs from the expected flat

behaviour when we deal with an isotropic angular distribution of the fission fragments (Figures 5.1 and 5.3). What we actually have is a cosine distribution that decreases when the angle is increased (decreasing cosine) as it is shown in Figure 5.15 for the ^{235}U.
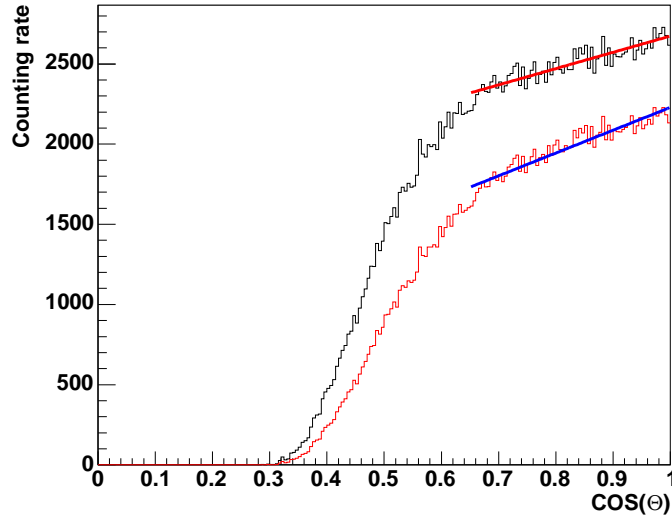

Figure 5.15: *Cosine distribution of the ^{235}U fission event with neutron energy below 0.8 eV. The red histogram represents the measured counting rate, while the black one is obtained after applying the threshold cut correction.*

At epithermal energies, where the isotropy is assured, the cosine distribution obtained after correcting the hardware threshold cut fits well for small angles to a straight line with a positive slope. This slope remains fairly constant in the whole low-energy range where no significant anisotropies are expected, leading us to assume that the slope of the straight segment of the cosine distribution does not depend on the neutron energy. This behaviour could be explained if full efficiency were not reached for the fission-event detection even at small angles, although a satisfactory explanation has not yet been achieved.

The FFAD for high neutron energies have been studied taking this feature of the cosine distribution into account. In a first approximation, the FFAD for a given energy can be parametrized by an anisotropy factor, defined as

$$B = \frac{W(0°)}{W(90°)} - 1 \tag{5.4}$$

where $W(\theta)$ is the angular distribution in the center-of-mass frame and θ is the angle between the neutron beam and the fragment emission axis. It has been shown [75] that for high-energy neutrons the FFAD may be expressed by:

$$W(\theta) = \frac{K_{norm}}{2} \left(1 + B\cos^2(\theta)\right) \qquad (5.5)$$

where K_{norm} is a normalization constant.

Previous experiments to determine anisotropies in fission reactions used monoenergetic neutron beams and the FFAD determination was limited for those neutron energies available in each experiment. However, the n_TOF experiment has a continuous spectrum from thermal to high neutron energies and the neutron energy is accurately determined by time-of-flight techniques. Therefore, a wider energy range and a higher accuracy are available at n_TOF.

In order to study the FFAD in function of the neutron energy, the fission events have been grouped in energy intervals that contain enough statistics to have useful cosine distributions. Because of the high statistics available, the intervals are quite narrow when compared with the energy spread of the monoenergetic beams and anisotropy does not vary significantly inside them.

The cosine distribution for each energy interval is fitted by a polynomial that includes both the PPAC linear behaviour and the anisotropy quadratic term. The fitting polynomial is expressed as follows:

$$F(\theta) = C \left[P_0 + P_1\cos(\theta)\right] \left[1 + B\cos^2\theta\right] \qquad (5.6)$$

where P_0 and P_1 contain the information on the energy-independent linear behaviour, B is the anisotropy parameter, strongly dependent on the neutron energy, and C is a normalization constant. Unlike for ^{235}U, there is no information about the linear behaviour at epithermal energies for ^{234}U and ^{238}U, because their small cross sections at such energies produce low statistics. Hence the parameters which define the linear contribution have been calculated at the MeV region using as reference the anisotropy values given by previous experimental measurements [76,77]. P_0 and P_1 have been determined by fitting the cosine distribution to Equation 5.6 in this energy range while B is kept fixed. These P_0 and P_1 values are then used in the whole energy range to determine the energy dependence of the anisotropy parameter B.

The anisotropy parameter obtained for the different isotopes are shown in the Figures 5.16, 5.17 and 5.18.
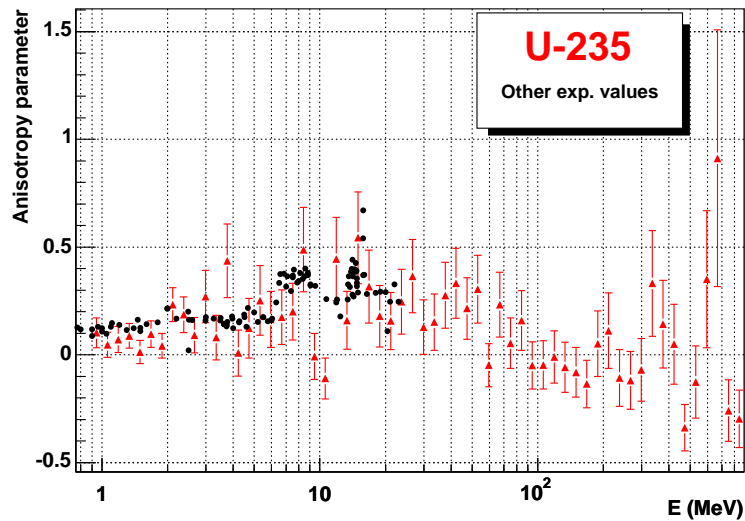
Figure 5.16: *Anisotropy parameter B obtained for ^{235}U compared to experimental values provided by other authors [76, 77] (black markers).*
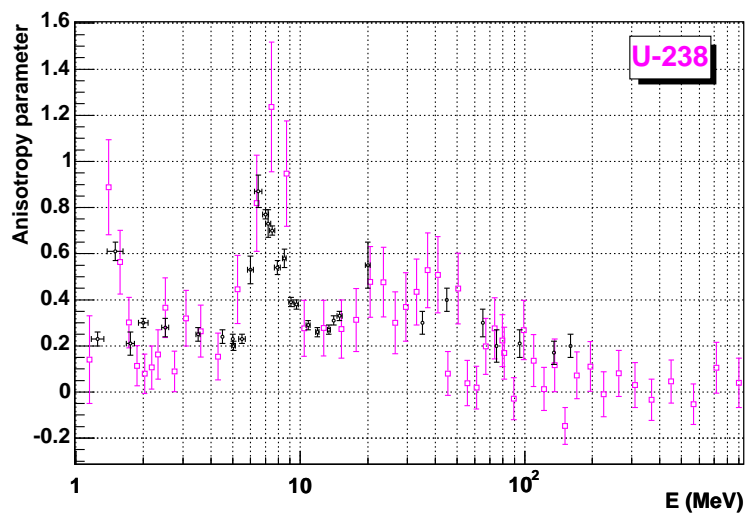
.

Figure 5.17: *Anisotropy parameter B obtained for ^{238}U compared to previous measurements [75, 76] (black markers).*
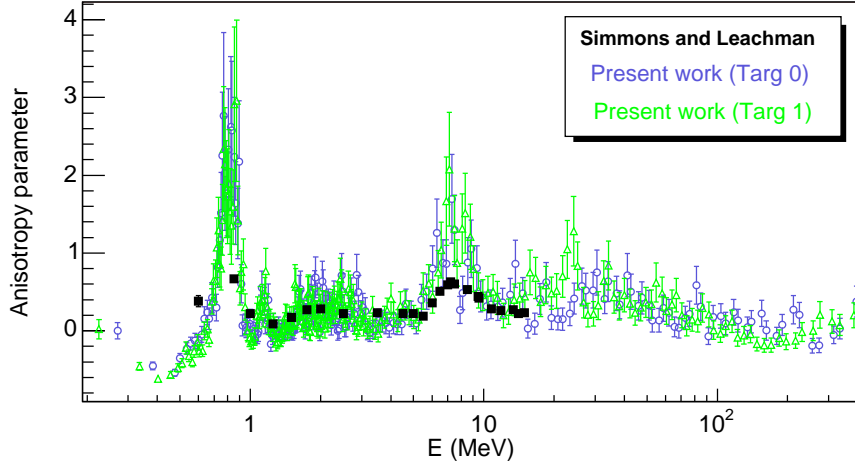
Figure 5.18: *Anisotropy parameter obtained for both targets of ^{234}U compared to experimental values provided by Leachman et al. [76] and Simmons el al. [77]*

The results obtained for ^{234}U and ^{238}U reproduce qualitatively the previous measurements, but overestimate the anisotropies at the peaked values. It must be noticed again that the angular range attainable with the PPAC is restricted and the cosine distribution behaviour must be extrapolated for large angles, affecting the accuracy of the obtained anisotropy parameter. The uncertainty estimated for the anisotropy parameter is large compared to those given by previous measurements. Therefore, in order to determine the efficiency of each target, we have used the anisotropy parameter extracted from experiments specifically dedicated to it that present less uncertainties [75–80].

It is worth mentioning that experimental measurements of the anisotropies are very scarce for neutron energies above a few tenths of MeV and that the values calculated in this work are the first measurements done at high energies for isotopes such as ^{234}U. Wherever there are no well-established references for the anisotropy, we have used our values to estimate the detection efficiency.

5.4   Efficiency estimation

The previous section described how to calculate the parameters that reproduce the cosine distribution in the full angular range, so that we can predict the expected cosine distribution outside the supposed 100 % efficiency range.
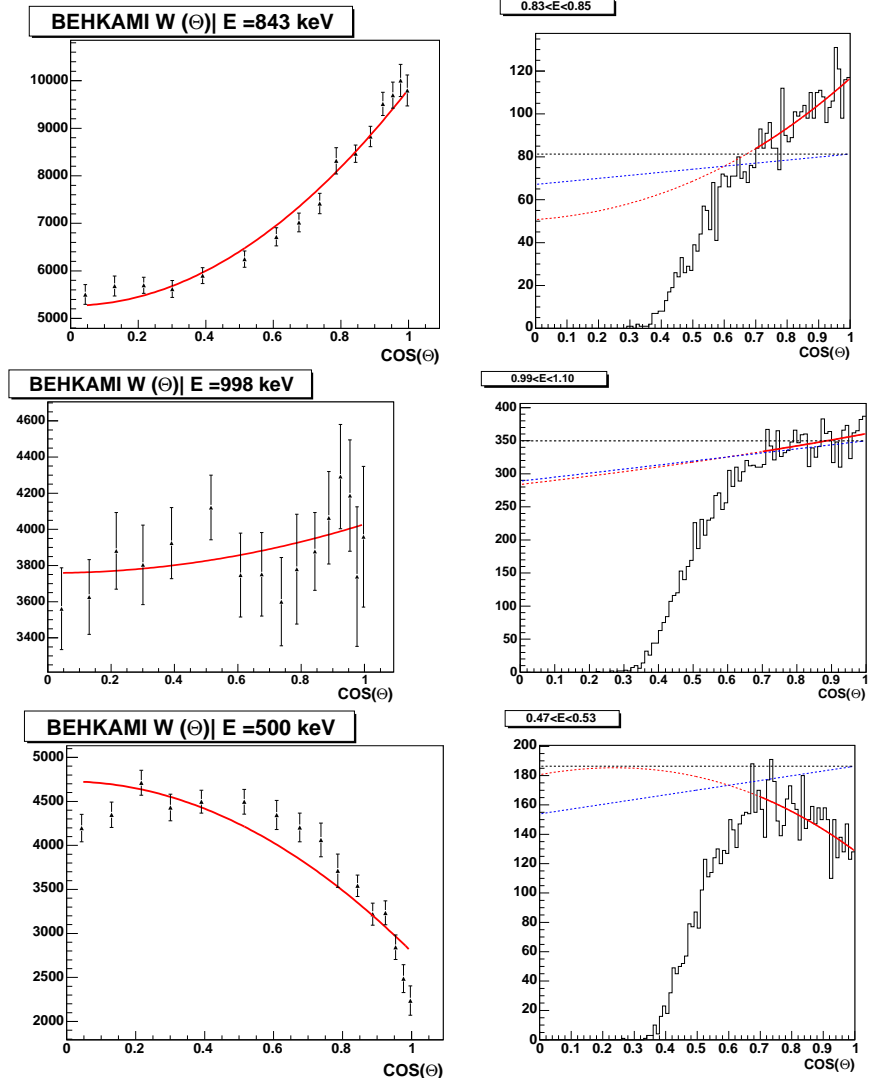
Figure 5.19: *Cosine distribution of the fission fragments at different near-threshold energies obtained by Behkami [34] (left column) and our results (right column). Red curve represents data fit from equation 5.5. Additionally, black and blue lines represent the expected and real behaviour of the cosine distribution in case of isotropy.*
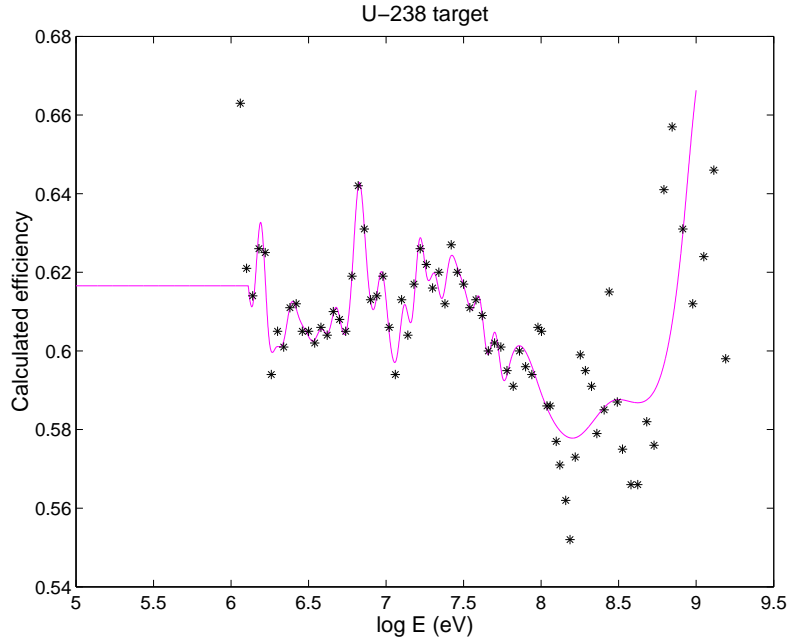
Figure 5.20: *Efficiency calculated for Target 8 (^{238}U) in the whole energy range. The black points represent the efficiency calculated for each energy interval, whereas the solid curve is the spline function obtained by least-square approximation to the data. Only values up to 14 MeV can be obtained for B from previous experiments.*

The set of Figures 5.19 shows, for different neutron energies, the predicted behaviour of the fission fragment angular distribution of ^{234}U fission in the full angular range. The three energy intervals near the fission barrier represent the possible cases: when the FF are preferentially emitted at 0°, at 90° and almost isotropically, that correspond to a positive, negative and close-zero anisotropy parameter, respectively. Our results are comparable to the angular distribution extracted from Behkami's article [34] at the same energies and the anisotropy parameter obtained by the fit in both sets of data - Behkami's and ours- are consistent. For positive values of anisotropy parameter, the FFAD agrees well with the expression $W(\theta) \propto 1 + cos^2\theta$, but the fit performance is worse when anisotropy parameter becomes negative ("sideways" angular distributions). This suggests that terms with higher cosine powers should be considered for reproducing these angular distributions (Figure 2.9). In any case, the anisotropy parameter is negative only in a limited energy range near the threshold (see Figure 5.18), so that the approximation done is good enough
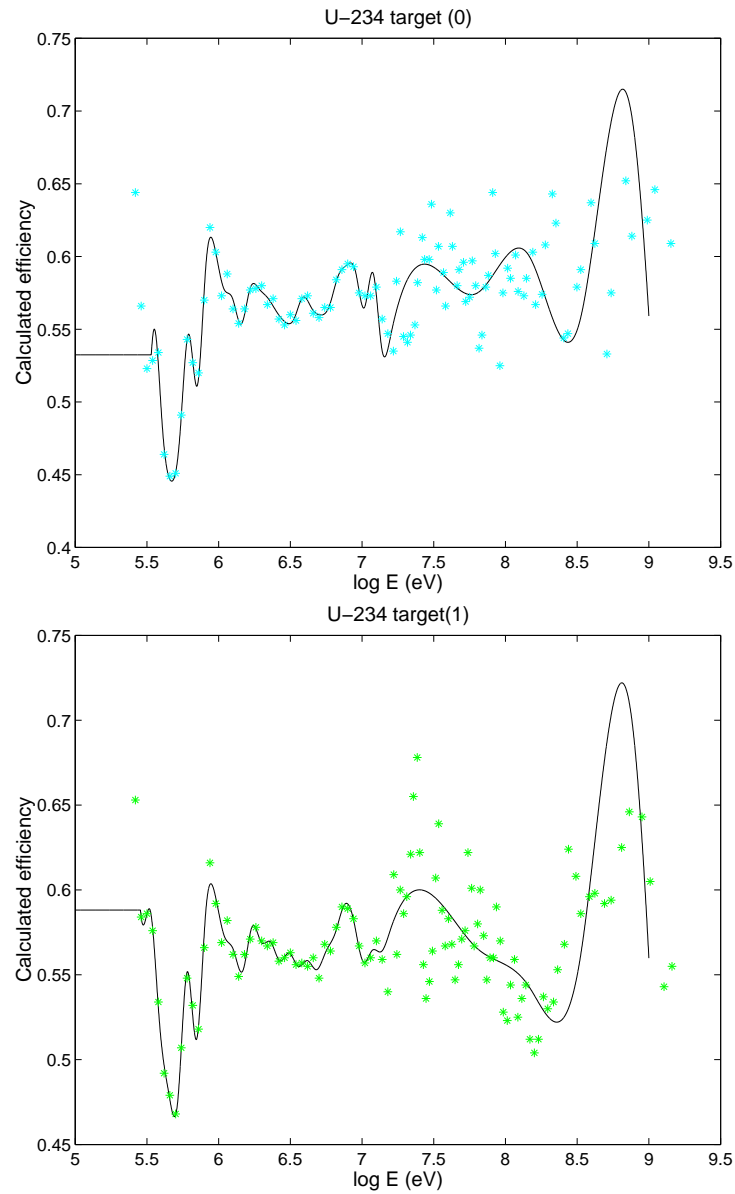
Figure 5.21: *Efficiencies calculated for Targets 0 and 1, respectively (both ^{234}U) in the whole energy range. The points represent the efficiency calculated for each energy interval, whereas the solid curves are the spline function obtained by least-square approximation to the data. The previous FFAD measurements reach up to 20 MeV.*

to calculate a suitable detector efficiency in the full energy range.

The method we have established for obtaining the detection efficiency for each target takes the full-range extrapolated behaviour of the cosine distribution and assumes that the area below the fit correspond to the total number of fission events. Therefore, the ratio between the actually detected fission events and this area represents the fission-event detection efficiency. The results of the detection efficiency in function of the neutron energy for ^{238}U and both ^{234}U targets are shown in Figures 5.20 and 5.21.
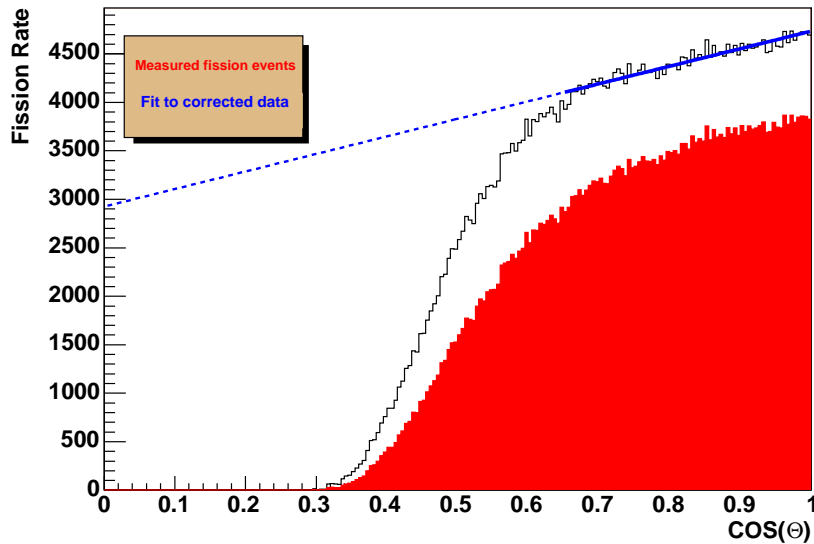

Figure 5.22: *The efficiency estimation at low energies is obtained from the ratio between the detected events (filled histogram area) and the area below the fit function (dashed line) predicted from the data after correcting the hardware threshold cut.*

The efficiency values obtained with this method are widely spread for energies larger than 20 MeV and also depend on the energy intervals we have selected, which are different for every target. Looking for an efficiency function behaving smoothly with the neutron energy, the *spline* approximation method [81] was used by means of the MATLAB program[2]. We can work directly with the spline functions and so the efficiency ratios between targets

---

[2]MATLAB (MATrix LABoratory) is an interactive software system for numerical computations and graphics [82].
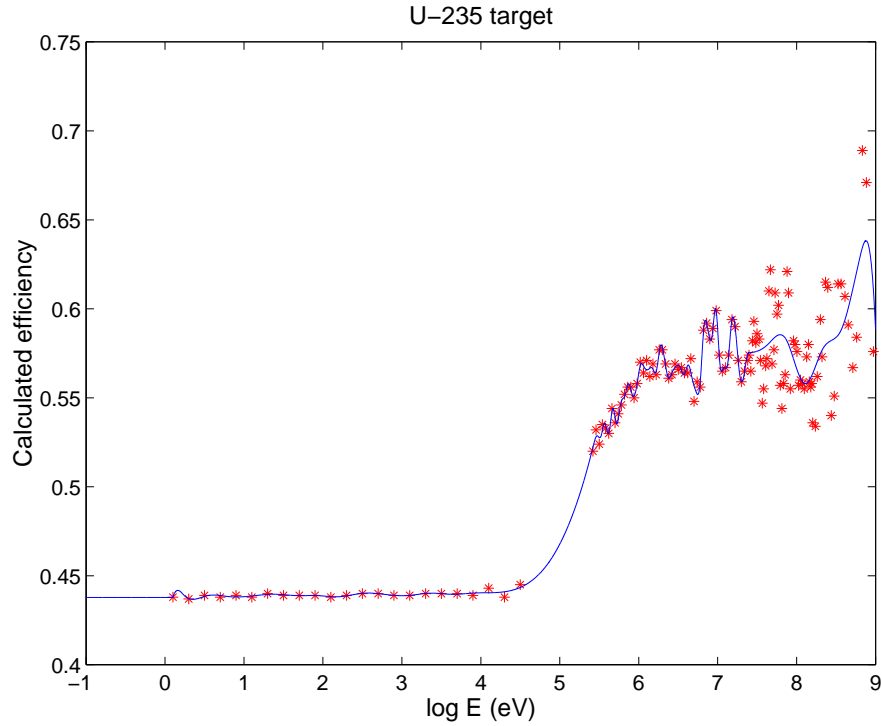
Figure 5.23: *Efficiency calculated for Target 7 (^{235}U) in the whole energy range. The red points represent the efficiency calculated for each energy interval, whereas the blue curve is the spline function obtained by least-square approximation to the data. The previous FFAD measurements reach up to 20 MeV.*

are easy to obtain. The uncertainties in the efficiency determination are estimated from the appearance of the efficiency curves. Where known anisotropy values are available the uncertainty is taken as 2 %, whereas it increase up to 10 % where we can only use the anisotropy parameter obtained by ourselves.

For the efficiency estimation at low energies, the hardware threshold cut must be taken into account. Correcting it in the cosine distribution for each energy interval and assuming isotropy for the FFAD ($B = 0$), the area below the linear fit represents our estimation for the expected number of fission events (Figure 5.22).

For the ^{235}U target, the efficiency values obtained at low energies are merged with those obtained at high energies, giving the efficiency for the full energy range (Figure 5.23).

5.5   n_TOF flux from PPAC

The cross-section extraction by means of the reference targets provides the estimated neutron flux of the n_TOF facility. This comprises the measurement of the energy spectrum and the spatial profile of the neutron beam.

The flux information is obtained from the measurements of the reference targets included in the PPAC setup, which are the ^{235}U and ^{238}U. What we obtain is the average flux over a large number of events, with enough statistics of fission events in the full energy range. The reference targets are measured simultaneously with the targets that we want to study, so the flux measurements related on this work are limited to the PS pulses of the set of runs including the ^{234}U target.

The average neutron flux can be expressed by:

$$\phi(x, y, E) = \frac{n(x, y, E)}{\sigma_f(x, y)\rho(x, y)\varepsilon(E)} \tag{5.7}$$

where ρ is the target mass density in a given surface element, $\varepsilon(E)$ is the efficiency calculated in the previous section and n(x,y,E) is the number of fissions originated at a given surface element and neutron energy interval that is also referred in this work as the fission rate. For the results on this work, the most recent evaluations for ^{235}U(n,f) and ^{238}U(n,f) cross sections obtained from the unrealesed ENDF/B-VII [83] version have been considered.

5.5.1   Neutron spectrum

The energy spectrum of the neutron flux extracted from ^{235}U and ^{238}U PPAC data is shown in Figure 5.24. It expresses the averaged energy distribution for all the neutrons impinging the target and includes the full set of runs taken during the 2003 fission campaing. Data from ^{235}U are the best suited in order to cover the whole energy range, because of the large cross section for the neutron-induced fission reaction at low energies. On the contrary, ^{238}U presents a fission threshold around 1 MeV, so it can only supply information about the flux above this energy.

The flux calculation includes the correction by the angle dependent efficiency as it was estimated in Subsection 5.4. As the efficiency depends on the energy too, it modifies the neutron flux shape.
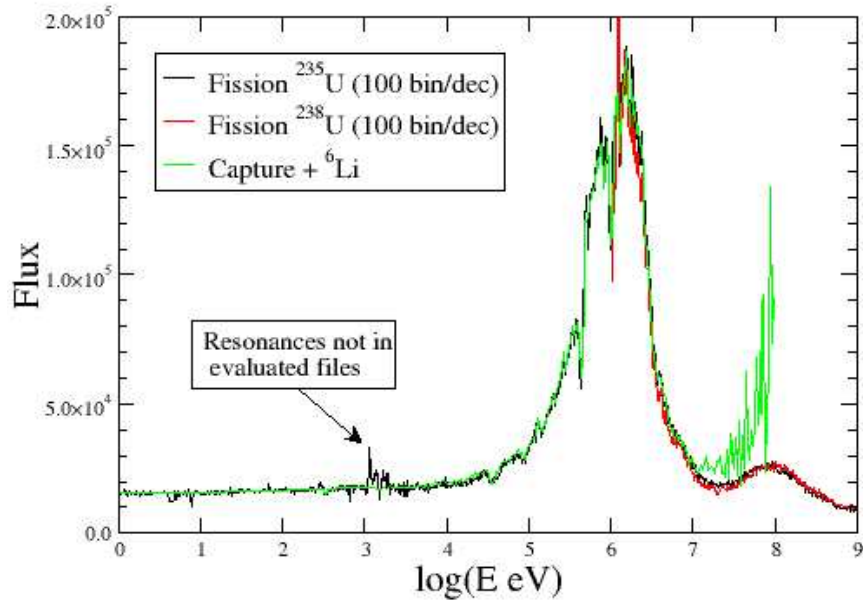
Figure 5.24: *Neutron flux obtained from PPAC data. compared to the flux obtained with the other detectors used at n_TOF during capture measurements (C_6D_6, PTB and SIMON).*

5.5.2 The beam profile

As it was previously explained, from the PPAC measurements we can extract the FF trajectory information which means that we can determine the location in the target where the fission reaction took place. The knowledge of the impact position on the target can be used to determine the beam intensity locally as function of the energy.

The fission rate distribution depending on the target position has been plotted by means of a 3-D histogram for fission events induced by neutrons below $1\,\mathrm{eV}$ (Figure 5.25). The distribution presents a clear asymmetry in both axes.

Taking into account the mass distribution measured at the IPNO (see Subsection 3.4), the neutron flux distribution can be obtained from that fission rate. In Figure 5.26, the beam profile is shown for nine neutron energy in-
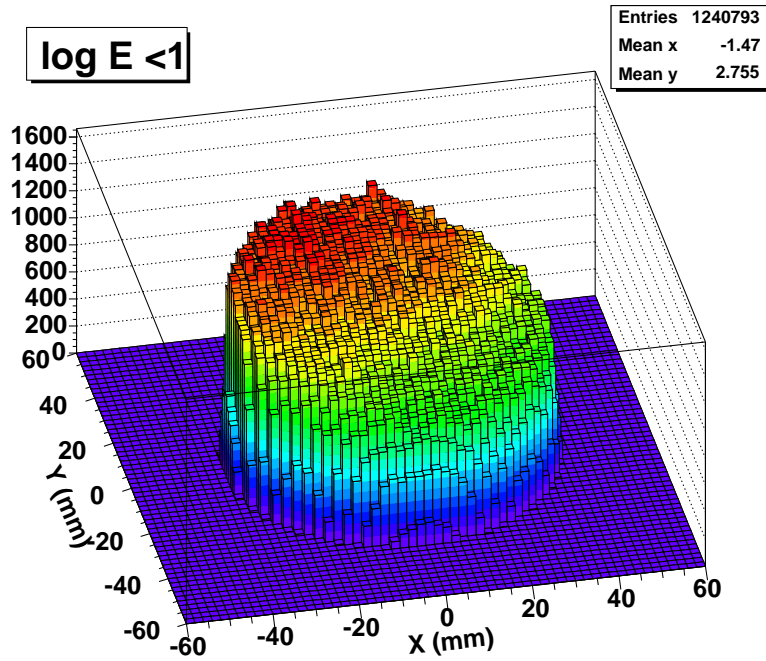
Figure 5.25: *Figure showing the fission distribution on the ^{235}U target for neutron energies below 1 eV.*

tervals. For every interval, it is obvious that the neutron beam axis is not centered in the target, but displaced to their top-left part. This is probably explained by a misalignment between the PPAC chamber and the neutron beam axis. The largest effect of this misalignment is a substantial reduction of the fission rates.
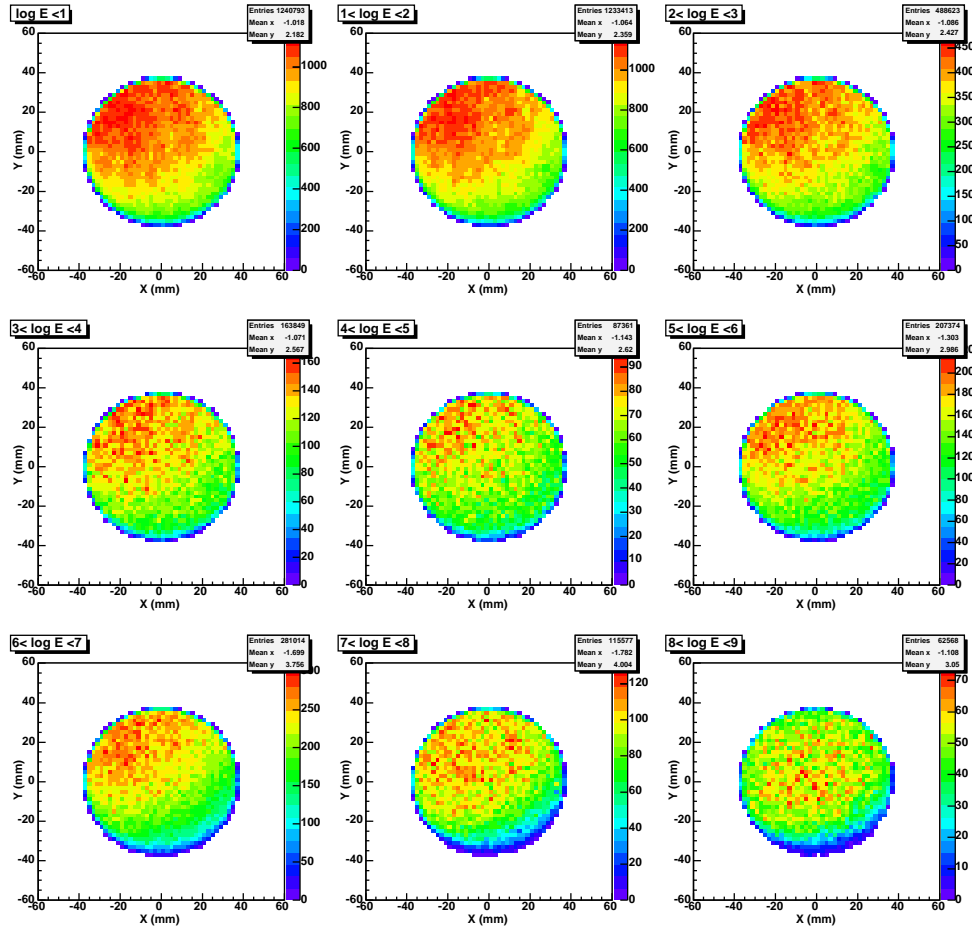
Figure 5.26: *Bidimensional profiles of the neutron beam obtained from*
^{235}U *counting rate for the different energy intervals.*

Chapter 6

^{234}U fission cross section results

The ^{234}U isotope appears in the thorium-uranium cycle from the neutron capture in the fissile uranium isotope ^{233}U, where the neutron capture competes efficiently with the fission in the case of slow neutrons. In this way, important amounts of ^{234}U are created in a reactor using thorium as fuel, so that ^{234}U neutron-induced cross sections must be accurately known to predict the performance of such type of reactors. However, ^{234}U evaluated data present discrepancies and are restricted to neutron energies below 20 MeV as illustrated in Figure 1.3.

From the theoretical point of view, ^{234}U is one of the isotopes involved in the *Th anomaly* [17] that indicates the existence of a triple-humped barrier (THB) in the potential energy. The study of the ^{234}U fission cross section at excitation energies around the barrier may reveal vibrational resonance structures, thereby directly confirming the existence of the THB.

6.1   Previous data on neutron-induced ^{234}U fission

Unlike ^{235}U and ^{238}U which have been extensively studied and are used as standards for neutron-induced fission cross sections, data on ^{234}U are scarce. Most of the fission measurements related to this isotope were performed more than two decades ago, when high neutron energy beams were not easily available. Experimental measurements with ^{234}U samples were also constrained by its high alpha activity (Half-life $= 2.457 \times 10^5$ years) and by the scarce available quantities of ^{234}U isotopically pure enough to perform a clean fission cross-section measurement. The nuclear data community is taking up again

the interest in ^{234}U because of its role in the Th-U cycle.

Most of the previous data on ^{234}U neutron-induced fission cross section are collected in the EXFOR library[1]. Experimental data found for neutron energies near and above the fission threshold are shown in Figure 6.1. It can be seen how the experimental values barely reach up to 20 MeV and they differ by at least 5 % in the MeV region. The evaluations in the resolved resonance region is mainly based on the ORELA[2] measurements performed by James et al. [84] nearly thirty years ago.
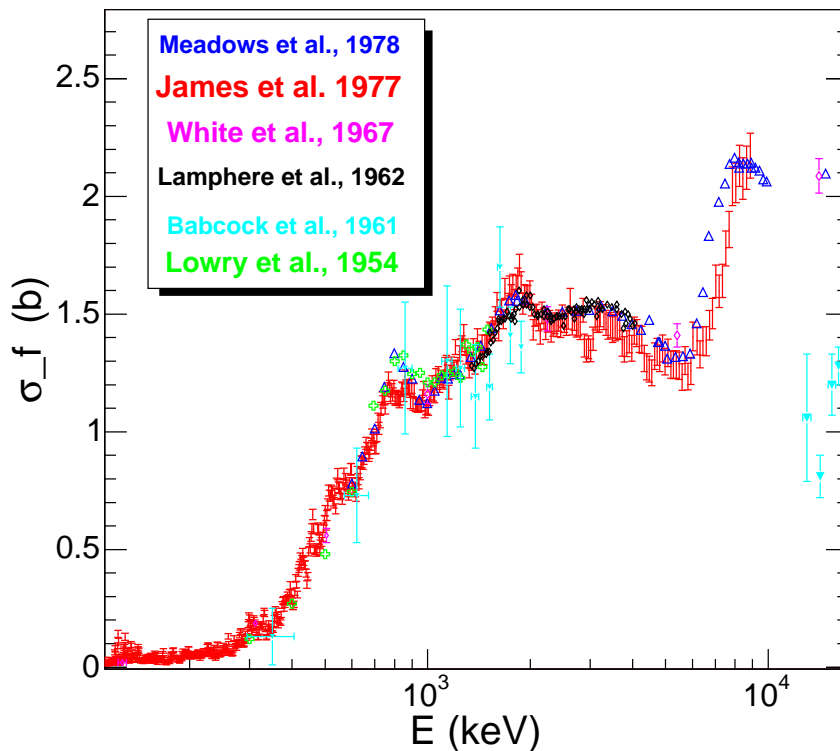

Figure 6.1: *Neutron-induced fission cross-section data in the near-barrier energy range from experimental works included in the EXFOR library [84–86].*

Because there are some discrepancies among the evaluated databases, from now on we will compare our results with the latest ^{234}U evaluation supplied by the ENDF (release ENDF/B-VI.8). By the time of writting this thesis, NEA released the 3.1 version of the JEFF database, so that we have also added the comparision with this evaluation for most cases.

6.2 Present work results

The results obtained for the ^{234}U fission cross section from the PPAC data measured during 2003 campaign are summarized in this section. Fission cross sections were measured for the entire energy range available at the n_TOF facility: from the eV region up to 1 GeV. Dealing with such a large range, the analysis had to be divided into a few energy regions in order to examine the details thoroughly.

During the 2003 fission campaign two ^{234}U targets, labelled as 0 and 1 (Figure 3.8), were put in-beam to be measured. The PPACs surrounding each target present different characteristics (thresholds, voltages,...), so that both target treatments were done in parallel - as two independent measurements with their specific corrections - until the last step when cross sections are produced. At this point, the results obtained for both targets were added to provide the final result that includes all the available statistics.

6.2.1 Fission rates.

After the data reduction process described in Chapter 4, the fission rates of every target are obtained. In order to supply the cross sections we have to refer these fission rates to the total number of neutrons impiging the targets, which is obtained from the fission rate of the reference targets (following Equation 5.2). Until now, only relative cross sections are obtained, so that the total number of atoms in every target has not been considered. The lack of an absolute reference for the cross section has been solved normalising our results to the evaluated data (ENDF/B-VI).

The statistics achieved in the measurements partially determine the uncertainty of the results (statistical uncertainty). Figure 6.2 shows the fission rate we obtained for both targets from the data reduction process. The histograms are plotted with 1000 energy bins per decade to provide an outlook of the available statistics. The statistics for every target amounts to a few hundreds counts per bin in the MeV energy range.

The fission rates have to be corrected by the efficiencies as explained in Chapter 5. The resemblance between the fision rates of both targets after
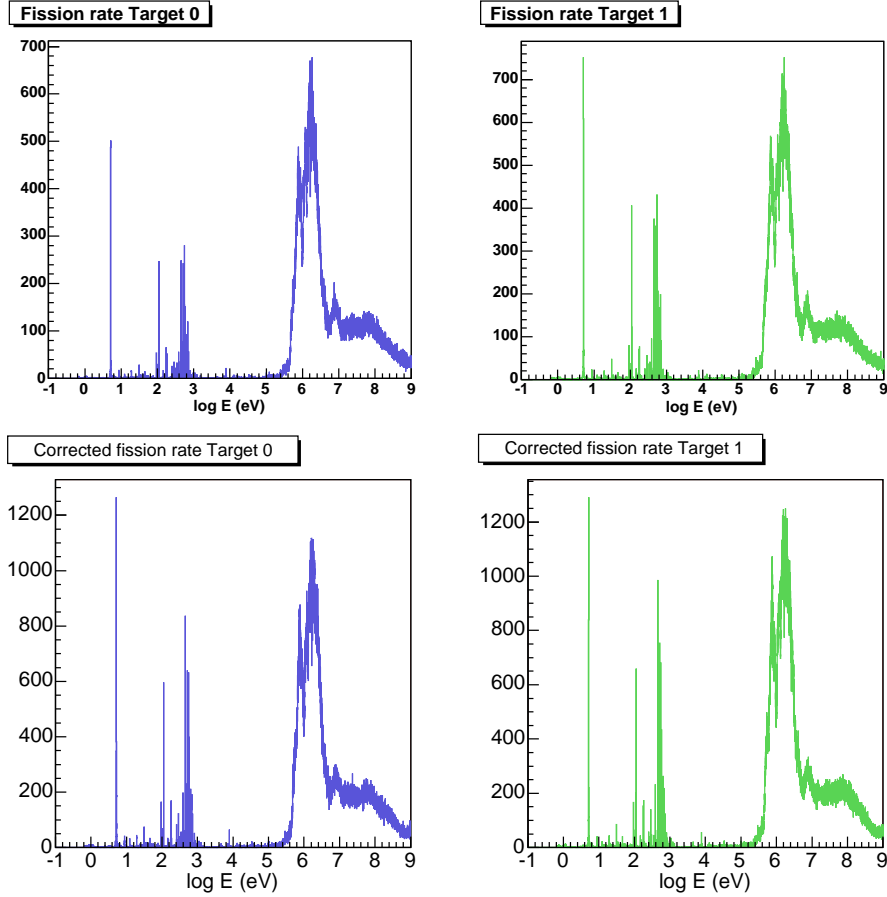
Figure 6.2: *Fission rates for both ^{234}U targets before (top histograms) and after (bottom histogram) efficiency correction.*

correction is better than before (Figure 6.3). The uncertainty introduced by the efficiency correction is added to the statistical uncertainty, being dominant at higher energies because of the indetermination in the efficiency reponse in this range.

The ratio between their fission rates is another way of comparing both targets results. For the energy range above the fission threshold there are enough statistics to reproduce this ratio with a histogram, shown in Figure 6.3. Both ratios, before and after the efficiency correction, have been normalised by a factor coming from the different number of atoms and the different inhomogeneities in the targets, that has been assumed as constant with the neutron
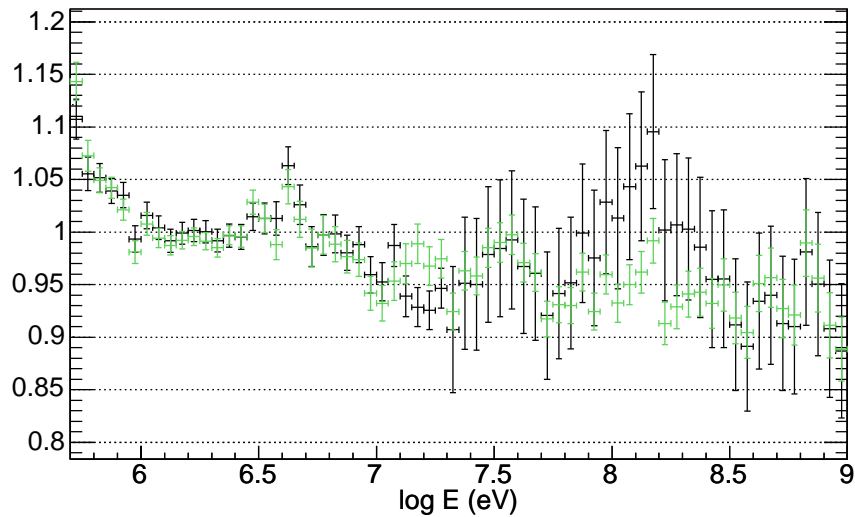
Figure 6.3: *Fission rate ratio of the two ^{234}U targets before (green markers) and after (black markers) applying the detector efficiency correction.*

energy. The ratio has a smooth behaviour in the MeV energy range corresponding to maximum counting rate at the neutron flux peak. Going up in energy, the decrease in statistics produce large uncertainties, which become even larger regarding the corrected ratio values due to the contribution of the efficiency uncertainties. At energies below the threshold, we only have enough statistics in the most important resonances to obtain a meaningful ratio between both targets fission rates. The efficiency correction becomes very important in this energy range because it accounts for the signal suppression due to the hardware threshold cut explained in Chapter 5. The ratio obtained for the largest resonances fluctuates between 0.95 and 0.98, consistent with the values obtained at higher energies. This means that the work done to estimate the loss of low-amplitude signals is heading in the right direction. Figure 6.4 shows the fission rates for some resonances, indicating that the statistics is enough to perform a resonance analysis.

6.2.2 Fission cross sections

Once the total fission rates are obtained for both ^{234}U targets including the whole set of runs, they are compared to them with the fission rates obtained for the reference targets and the same runs in order to get the ^{234}U fission
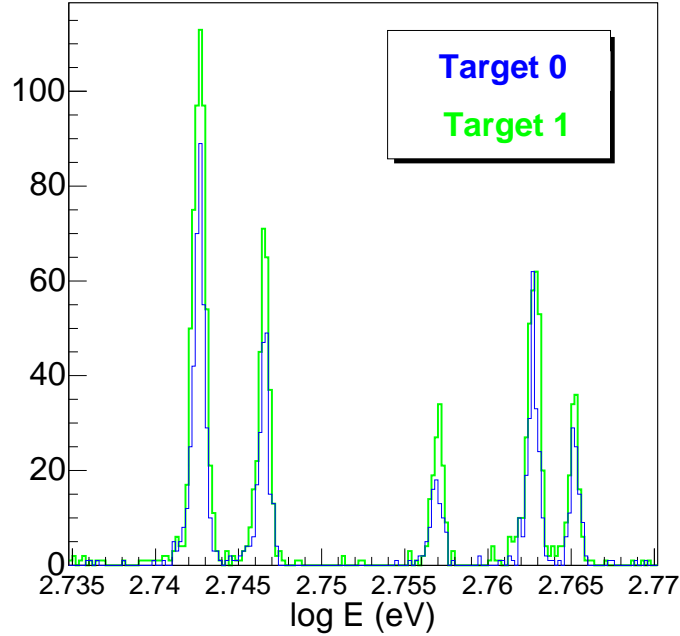
Figure 6.4: *Fission rates at a given resonance region interval for both ^{234}U targets. The resolution obtained with a histogram binning of 5000 bins/decade is enough to observe the resonance structure. To give an idea of the available statistics, the fission events under the largest resonance peak in the figure are 360 counts for Target 0 and 565 for Target 1.*

cross section. As the PS events included in the analysis of each target is the same, we can assume that the total number of neutrons impinging every target is the same. The ^{234}U(n,f) cross section (shown in Figure 6.5) have been calculated using the ^{235}U target as reference because it provides information on the whole energy range, whereas with ^{238}U only the high energy cross section can be obtained.

In order to produce a relative cross section, our results have been normalised with respect to the ENDF evaluated cross section. The energy selected for the normalisation has been the interval from 1 to 4 MeV, where the n_TOF flux is large and good statistics is assured. In addition, the uncertainty introduced by the efficiencies estimation is small, because the anisotropies of the uranium isotopes are small and well-know at these energies. ENDF/B-VI
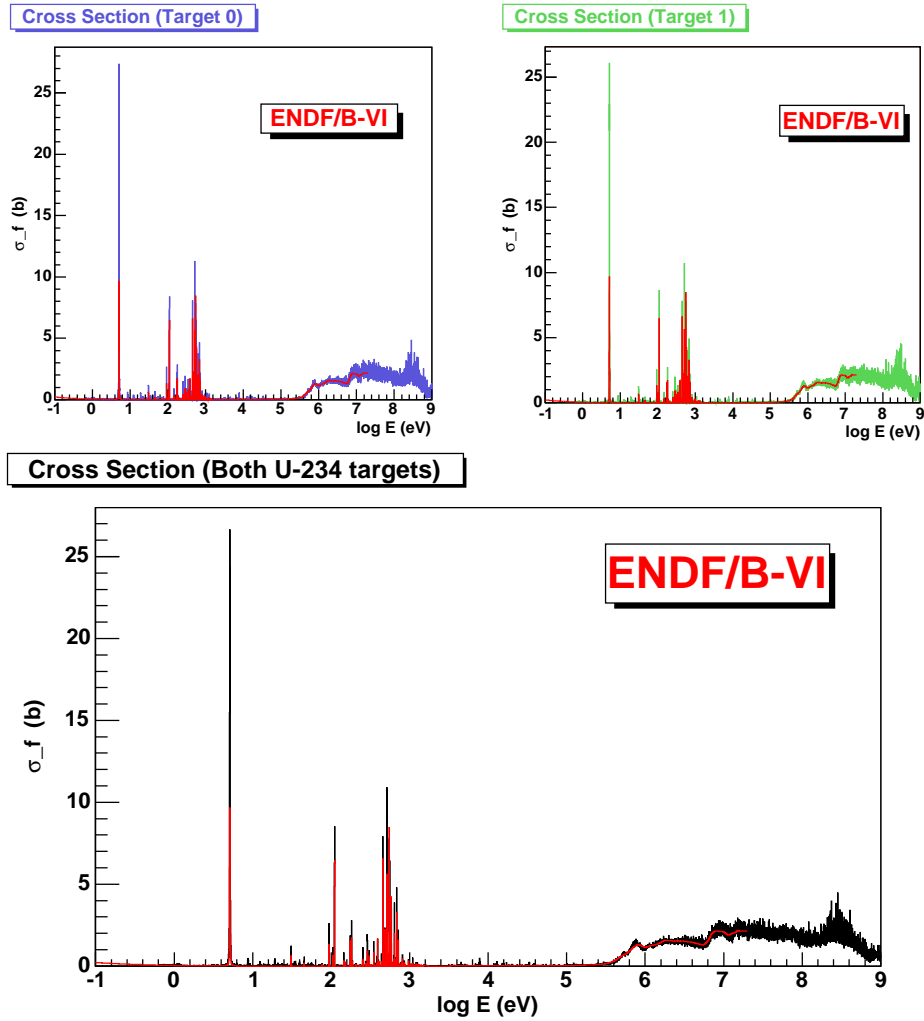
Figure 6.5: $^{234}U(n,f)$ *fission cross section in the full energy range. The histogram binning is 5000 bins/decade. This binning is enough to study the resonance region. In the top charts each target results is shown while the bottom chart represents the added results of both target. All the histograms are normalised to the ENDF/B-VI (solid red curve) between 1 and 4 MeV.*

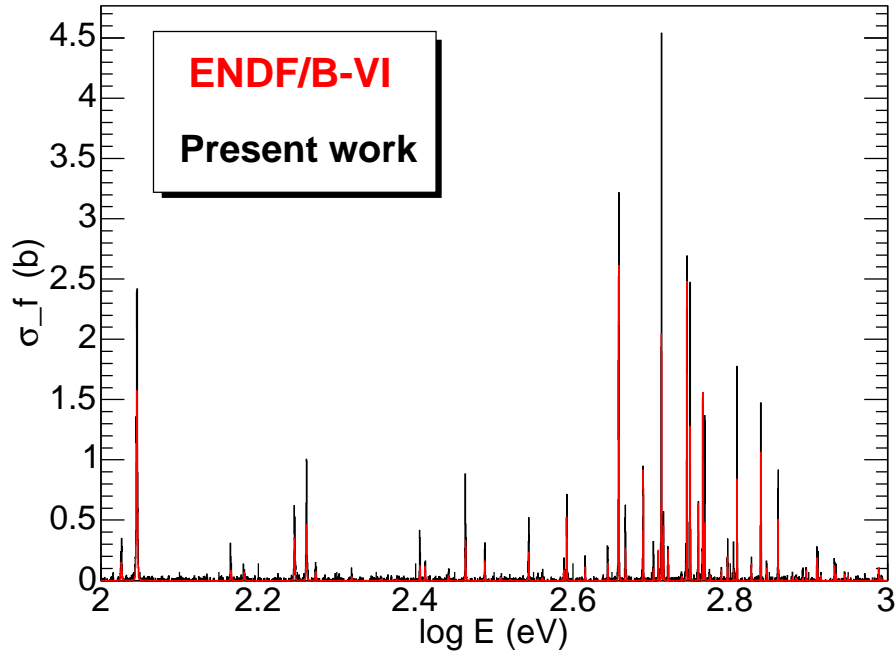and JEFF-3.1 evaluation are rather similar in this energy range, with an average discrepancy of less than 3 %.

Figure 6.6: $^{234}U(n,f)$ *cross section at the resonance region between 100 eV and 1000 eV. The clustering of the fission resonances, referred in Chapter 2, can be distinguished.*

6.2.3   Resolved Resonance Region

Contrary to other even-even actinide isotopes such as ^{238}U or ^{232}Th, the ^{234}U present remarkable subthreshold resonances as it can be observed in Figure 6.6. Actually, the largest ^{234}U fission cross section corresponds to the resonance located at 5.16 eV which was used as the reference to calibrate the time-of-flight path length corresponding to the positions of the PPACs.

In the resolved resonance region, which extends up to 1.5 keV, the resonances are fairly well separated and they are best described by the R-matrix theory [87]. The fission resonance parameters have already been determined by James et al. [84] from the data they obtained at ORNL (Oak Ridge National

Laboratory, USA). These data, together with the data obtained by C. Wagemans [88] at the IRMM (Institute for Reference Materials and Measurements) in Geel (Belgique), are compared to the n_TOF PPAC data. The better resolution we achieved with the our setup will allow us to improve the current data in the resonance region, so that a revision of the resonance parameters is foreseen.

In the neutron energy range from 100 to 1000 eV, the total area below the resonances calculated from these results were compared to the two evaluations we have considered. A better matching has been found between the obtained cross section and the recent JEFF-3.1 evaluation – 30 % larger than JEFF-3.1 cross section whereas 80 % larger than the ENDF/B-VI evaluation.

Some resonances which are not in agreement with the evaluated data have been attributed to the ^{235}U impurities in the ^{234}U sample. Beyond 1.5 keV, if resonances exists, they are so small that we have no statistics to resolve them.

Figures 6.7 and 6.8 show the most relevant resonances that have been previously reported by different authors [84,88]. When they are compared with the evaluations, the differences vary from one resonance to other, confirming the need of a detailed resonance analysis to explain such behaviour.
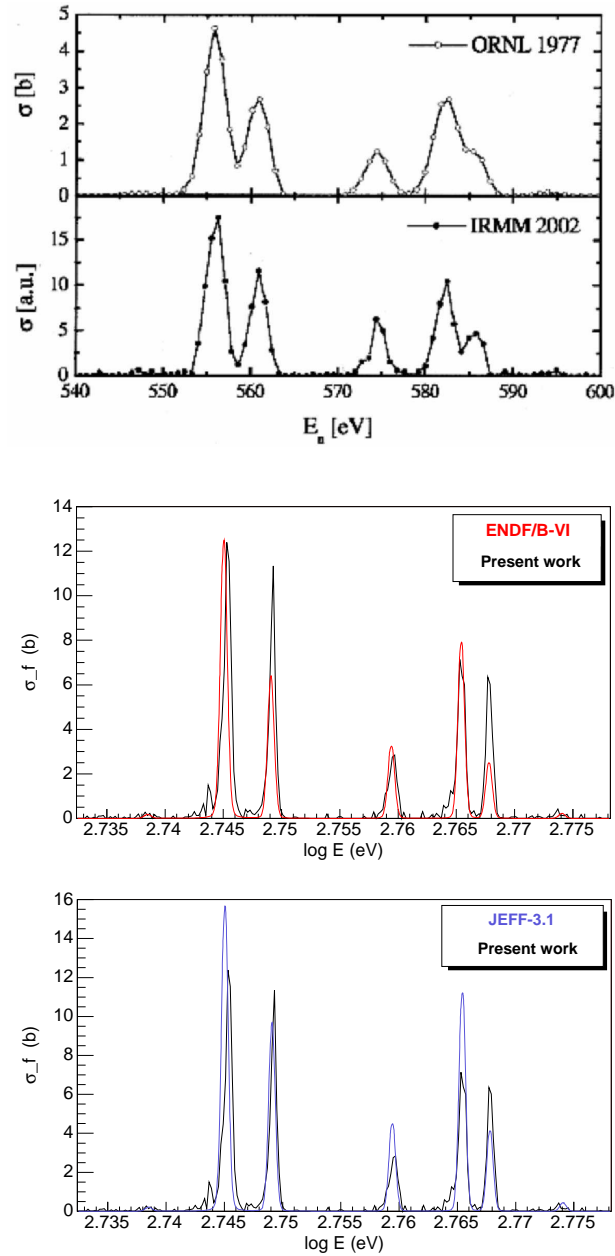
Figure 6.7: *ORNL [84], IRMM [88] and n_TOF PPAC data are shown in the energy range between 550 and 600 eV (equivalent to 2.74 and 2.78 in the logarithm scale). Our data are displayed using histograms with 5000 bins per decade, equivalent to a 0.2 eV bin width in this energy range, and compared to the last ENDF/B and JEFF evaluations.*

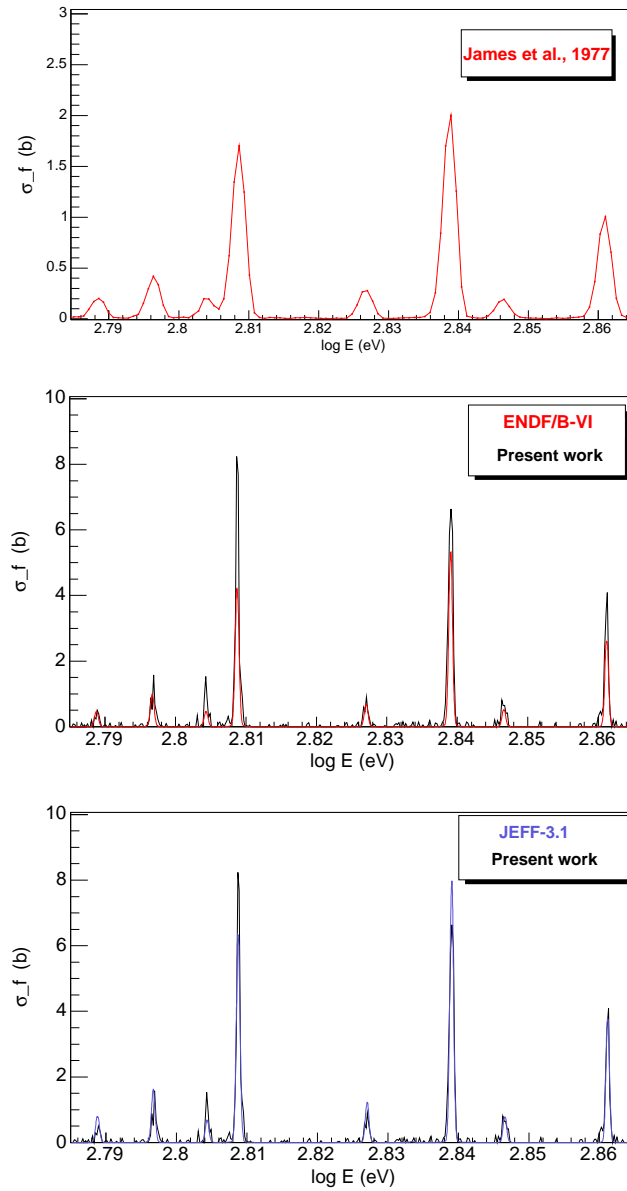**Figure 6.8:** $^{234}U(n,f)$ *fission cross section between 615 and 725 eV (equivalent to 2.79 and 2.86 in the logarithm scale). Data from James et al. [84] are shown in the top chart followed by our results compared with ENDF/B-VI (red histogram) and with JEFF-3.1 (blue histogram). The histograms have 5000 bins per decade, that means a bin width of about 0.3 eV in this energy range.*

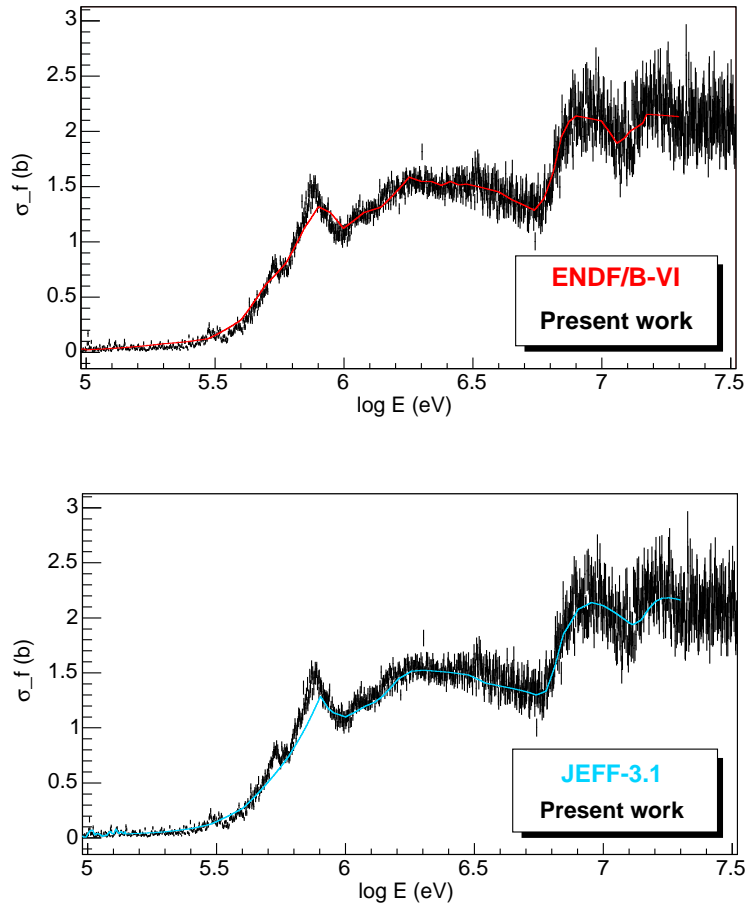### 6.2.4   Region above threshold region and up to 20 MeV

Figure 6.9: $^{234}U(n,f)$ *fission cross section is shown between 100 keV and 20 MeV compared to the ENDF/B-VI and JEFF-3.1 evaluations (solid curves).*

Figure 6.9 shows the cross section obtained in the energy range from 100 keV to 20 MeV, where we compare to the ENDF/B-VI and the JEFF-3.1 evaluations. The anisotropy values in this energy range are known from previous measurements and they are used in the efficiency estimation for each target. The histogram binning used in this region is 500 bins/decade that correspond to a binning width of $5 \times 10^{-3} \times E$, that is of the order of the energy resolution
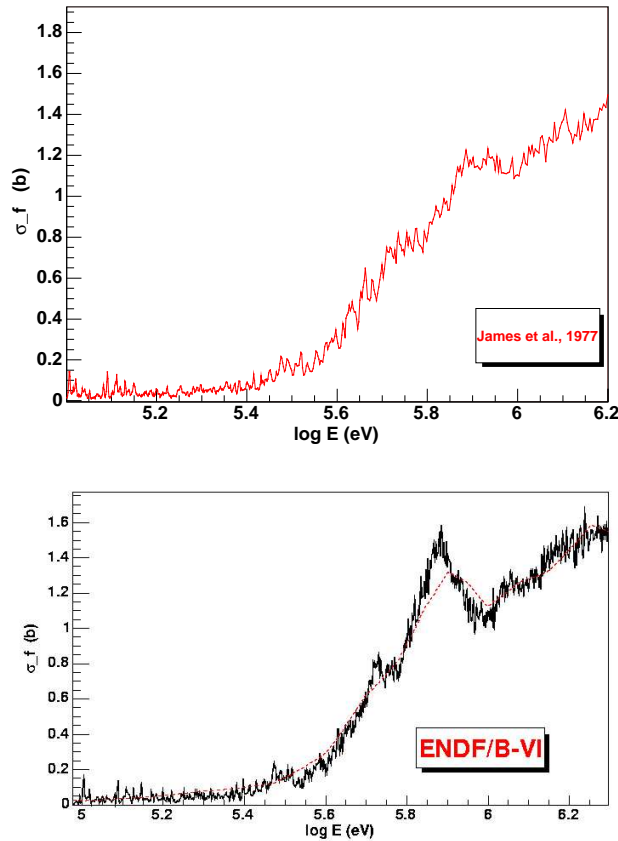
in the MeV range.

Figure 6.10: *The threshold region of $^{234}U(n,f)$ cross section is shown in detail compared with data from James et al. in the same energy range.*

The near-threshold region is quite interesting because of the structure observed near 325 keV (5.5 in the logarithm scale). Following James et al., it has been suggested that this must arise from a β-vibrational level in the second fission potential barrier minimum. Our results have a good statistical significance in this region (Figure 6.10) and confirm the structure at 325 keV. Larger differences appears at energies of 500 keV ($10^{5.7}$) and 800 keV ($10^{5.9}$). Nevertheless we have to take into account that this region is very sensitive to the quick variation in the fission fragment angular distribution, which was discussed in Section 5.6.

6.2.5   Region above 20 MeV

One notable contribution of the ^{234}U n_TOF PPAC measurement is the capability to extend the fission cross section data to energies above 20 MeV. The challenge of obtaining a more reliable efficiency correction and reducing their error is still open because of the lack of anisotropy data in the literature and other drawbacks related to the PPAC performance at very high energies (see Figures 5.20, 5.21 and 5.23). By the moment, efficiency uncertainties are as large as 10 %.
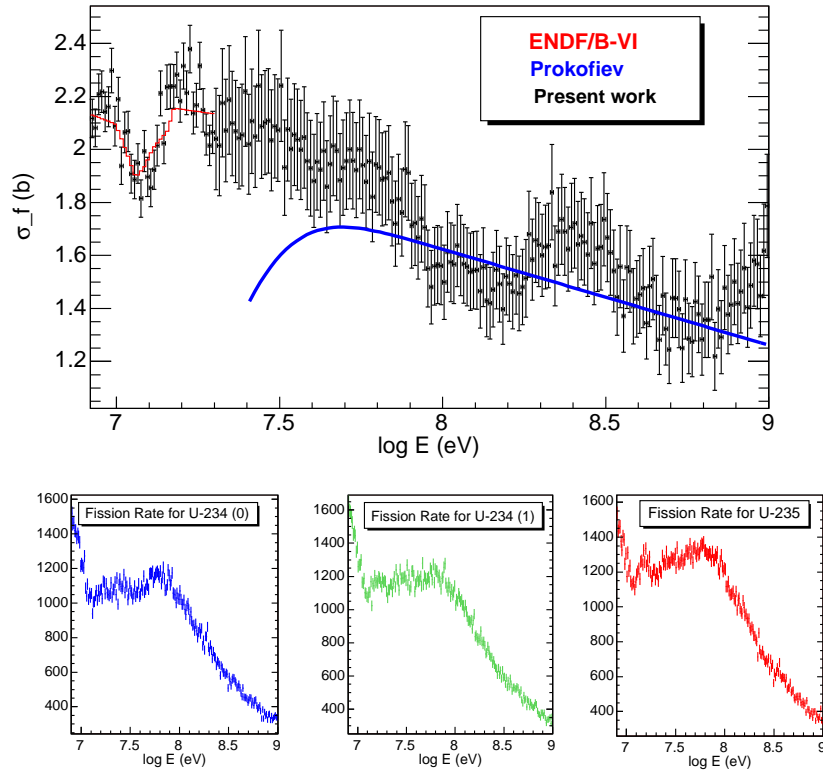
Figure 6.11: $^{234}U(n,f)$ *fission cross section obtained for neutron energies above 10 MeV. The histogram binning, 100 bins/decade, have been optimized to get statistical relevance in the fission rates as shown in the bottom charts.*

On the other hand, the counting rates at these neutron energies decrease for every target because of the reduction of the neutron flux. So that, the energy intervals in which the cross section is calculated are larger that of

lower energies. A histogram binning of 100 bins per energy decade allows us to have more than 400 counts per bin up to 1 GeV (less than 5 % of statistical error). Consequently, our fission cross section above 20 MeV has a systematic uncertainty much larger than the statistical one.

In an attempt to discuss the accuracy of our measurements above 20 MeV, where there is no neutron data, proton-induced fission cross section is assumed that behaves like the neutron cross section for very high energies. Therefore, we have considered the parametrisation of the proton-induced fission cross section collected in the EXFOR library provided by Prokofiev [89]:

$$\sigma_f(E_p) = P_1\{1 - \exp[-P_3(E_p - P_2)]\} \times (1 - P_4 \, lnE_p) \qquad (6.1)$$

where σ_f is the fission cross section (mb), E_p is the incident proton energy (MeV) and P_1, P_2, P_3 and P_4 are fitting parameters. The parameters P_2, P_3 and P_4 found for the actinide targets were equal within the uncertainty limits. For ^{234}U the adopted values were:

Parameter	P_1	P_2	P_3	P_4
Value	2348	12.1	0.111	0.067

and the curve obtained from this parametrization is shown in Figure 6.11.

It must be highlighted that the ^{235}U fission cross section, used as standard, has only been evaluated up to 200 MeV. Therefore, in order to provide a fission cross section for ^{234}U above 200 MeV, the ^{235}U data has been extrapolated. However, this extrapolation introduces a systematic uncertainty difficult to estimate.

It is possible to overcome the lack of evaluated data for referring our results by providing the ratio between the ^{234}U fission rate and any of the reference targets. The uncorrected fission ratios are shown in Figures 6.12 and 6.13.
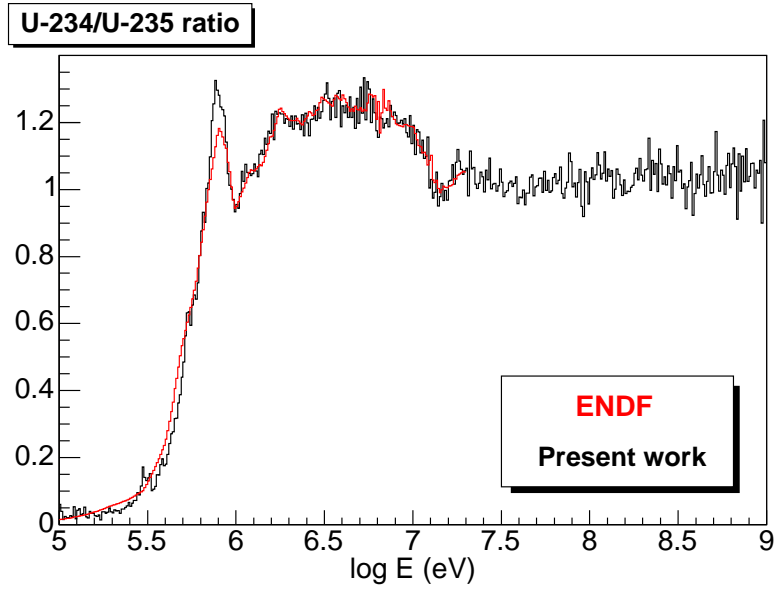
U-234/U-235 ratio

Figure 6.12: *Ratio between ^{234}U and ^{235}U fission rates for energies up to 1 GeV.*
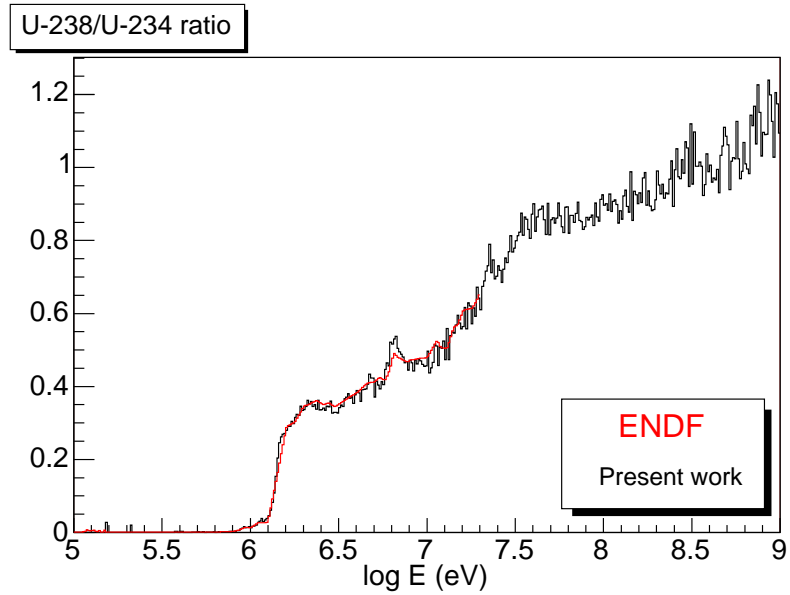
U-238/U-234 ratio

Figure 6.13: *Ratio between ^{238}U and ^{234}U fission rates for energies up to 1 GeV.*

Chapter 7

Conclusions

The aim of this work was twofold: to measure the ^{234}U neutron-induced fission cross section in an extended energy range with an unprecedented resolution, and, in the process, to validate the experimental method we used at the new n_TOF-CERN facility.

The experiment was designed in order to take advantage of the unique characteristics of the n_TOF facility: the long flight path offers a high energy resolution and the high-intensity, instantaneous neutron flux greatly reduces the background from the sample activities, making it possible to measure highly radioactive samples.

The fission detection setup is based on an innovative technique that benefits from the use of very thin targets and detectors. Up to nine targets of high purity fission samples are sandwiched by Parallel Plate Avalanche Counters (PPAC). When a fission event happens, the two complementary fission fragments are detected by the PPACs adjacent to the fissioning target in a narrow time coincidence. Because several targets are simultaneously placed in-beam, relative measurements with respect to reference nuclei can be obtained.

In this work, an original data-reduction method has been developed to deal with the particular characteristics of both the n_TOF data acquisition system, which is based on very accurate Flash-ADC digitizers, and the fission detection setup. The data reduction includes the coincidence windows and the signal amplitude requirements that we obtained from preliminary data analysis. The applied coincidence method is very powerful for dealing with the background rejection such as contamination by α activity, which is quite high for ^{234}U, and the signals produced by highly energetic reactions in the detectors. The data-reduction method also implements the fission event reconstruction using the position information obtained from the stripped cathodes and the delay

line readout, which makes it possible to determine the fission fragment angular distributions, and the time-of-flight to energy conversion.

After data reduction was completed, we entered upon the cross-section analysis. One of the key elements of fission cross-section analysis is to determine the detection efficiency, which was one of the most important undertakings of this work. Because of the setup characteristics, the angular acceptance reduces the detection efficiency to near 60 %, where acceptance is limited primarily by the absorption of the fission fragments in the dead layers of the detectors and the target backing. In order to understand the PPAC performance, simulations have been done to study the energy lost by the fission fragments crossing the detection setup.

Because of the restricted angular acceptance, detection efficiency depends substantially on the anisotropy of the fission fragment emission angle, and angular distribution has been included in the efficiency analysis. This feature has rarely been considered in previous fission cross-section measurements, but becomes relevant in the threshold regions where strong changes in the angular distribution are observed.

In this work, information on fission reaction anisotropy for ^{234}U has been obtained for energies which had never before attained.

These experimental techniques have been applied to the ^{234}U analysis, but the procedure we have developed can be used to study any target included in the PPAC setup. The ^{234}U fission cross section obtained in this work has been compared to the existing EXFOR data files and to the evaluated cross sections available from the ENDF/B-VI and JEFF-3.1 libraries. The following results can be highlighted:

- Unprecedented energy resolution for data at the resolved resonance region (δE/E= 0.46×10^{-3} at $1\,$keV).

- A new measurement in the energy range between $200\,$keV and $20\,$MeV with high statistics and good energy resolution (δE/E $< 5 \times 10^{-3}$ up to $10\,$MeV).

- First-time results above $20\,$MeV, within $15\,\%$ uncertainty.

Together, these findings indicate that a good-quality result is obtained for the ^{234}U fission cross section in the currently evaluated energy range that will help solve the existing discrepancies and could motivate a new resonance data analysis by means of specific analysis codes such as SAMMY [92]. Our data above $20\,$MeV provides a starting point for future work in the validation of current evaporation codes.

In addition, we obtained information regarding the beam profile and the energy spectrum of the neutron beam for the fission campaign configuration, that can be compared to the results obtained by other detectors for the capture campaign.

7.1   Outlook

The future of the PPAC detectors at the n_TOF facility looks promising. After two years studying the data obtained with the n_TOF PPAC setup, a lot of information has been adquired about the detectors, the acquisition system and the facility, which improve the setup performance. The main limitation in the detector performance turns out to be the significant fission fragments losses in dead layers of the setup, specially in the $2\,\mu$m target backing. New measurements with a thinner backing would improve the detection efficiency and the results. Another possibility would be to reduce the thickness of the PPAC dead layers, mainly the Mylar foils, although that implies reconsidering the structural components of the detectors.

In 2006, n_TOF activity will begin again after the mandatory stop because of the PS adaptation to LHC requirements. Among the proposals for the n_TOF Phase 2 is the construction of a second experimental area at a closer distance to the spallation target (approximately $30\,$m). Although this would somewhat affect the energy resolution, the flux intensity would increase 100-fold. This flux increase would make possible to work with less massive targets which would facilitate the measurement of very radioactive sources such as Americium or Curium isotopes, which safety regulations currently do not allow.

An alternative setup using PPACs can be designed to measure the fission fragment angular distribution in better conditions. One simple approach consists of displacing and tilting the PPACs and targets with respect to the neutron beam so that the current angular acceptance would broaden from the current $50°$ to near $90°$, even without any major modification of the current setup. The minimisation of fission losses registered at small angles would also substantially improve the results obtained for the angular distribution and subsequently for the detection efficiency.

The n_TOF PPAC capability for attaining higher energies and better resolution than previously obtained for neutron beams will lead to the development of fission experiments that confirm the nuclear models by studying cross sections, angular distributions and even mass distributions of the fission fragments.

Appendix A

FADC module time-shift

During the first stage of the PPAC data analysis, an anomalous behaviour appeared on some *configurations* (Subsection 4.2.1) that include anodes connected to different Digitizers. As an example, the correlation between the time differences of adjacent detectors in the type_3 events, including detectors 6, 7 and 8, is shown in Figure A.1. While most of the *configurations* have a time difference T1-T2 near zero (Y axis), there is a significant number grouped around 10 ns. Looking for an explanation we realise that the anodes corresponding to detectors 7 and 8 are connected to two different FADC modules and that the shifted *configurations* are grouped by PS events; this means that either every *configuration* in the PS event is shifted or none is shifted at all.
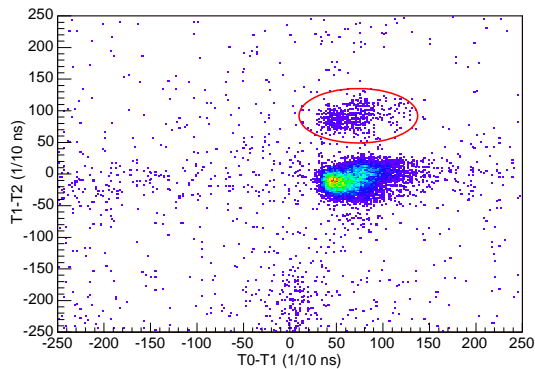

Figure A.1: *Correlation between time differences of adjacent anodes at type_3 configurations for run 5110. The shifted events appear inside the ellipse around T1-T2 = 10 ns.*

A detailed study revealed that, although all FADC modules use the same trigger signal, the internal time of some modules occasionally shifts with respect to the others. This behaviour can only be explained by an irregular Digitizer performance with the following characteristics:

- Although this behaviour is found in most of the runs, the effect is only critical in a small portion of them where more than 5 % of the events are affected.

- PS events with any time-shifted module are randomly distributed along the run, without any periodical pattern.

- Several FADC modules exhibit time shifts during the campaign, but their shift frequency varies from time to time.

- The shifts look like if they were produced by a clock jump of either 10 or 20 ns.

This kind of shifts between modules makes it difficult to recognise the fission events, for what a precision of nanoseconds is required. The cathode signal search also becomes more difficult because the time shift of the signals affects the diagonal condition (Equation 4.1).

Fortunately, it is possible to identify and correct the shifts using the Gamma Flash signal information. The Gamma Flash produces a simultaneous signal in every detector, so that the time shift of any FADC module can be observed in the respective anodes.

Identification of the shifted modules by means of the Gamma Flash

To solve the problems arising with this FADC anomalous behaviour the use of the Gamma Flash signal must be very carefully considered, because it cannot always be fully identified due to interference from signals produced by fission fragments or alpha particles.

An extensive study on the behaviour of the anode modules during the set of runs revealed that, in the FADC channels of any shifted module, the Gamma Flash signal always comes ahead of its expected value, and at least one of the modules is shifted by 20 ns.

With this information, we have implemented a method that distinguishes which PS events have any shifted module minimizing the risk of considering
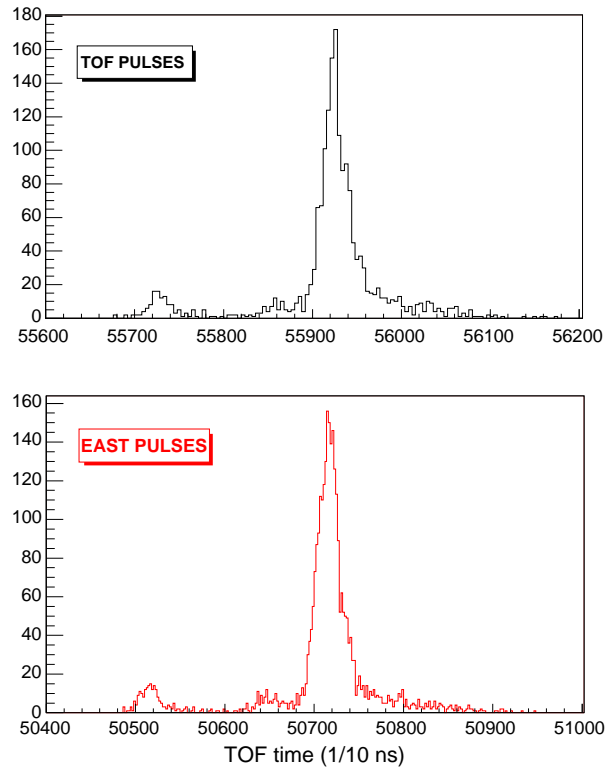
Figure A.2: *Time distribution of the Gamma Flash signal obtained from detector 8 for every PS pulse of the run 5135. The smaller peak appearing 20 ns before the main one is related with the PS pulses which present the corresponding FADC module shifted 20 ns in advance.*

normal events as shifted ones. This method checks if the Gamma Flash signal is advanced 20 ns with respect to the usual times in more than half of the FADC channels of any module containing PPAC anodes. When at least one module is found to be shifted 20 ns, the PS event is marked and the time differences between the Gamma Flash signals of these modules and those of the other modules are calculated and stored for later correction.

This identification procedure is very efficient, correctly distinguishing more than 98 % of the PS events that present any shifted FADC module. Nevertheless, it can occasionally mistake a normal PS event for a shifted one. Although the probability of this mistake is very low – estimated at about 1/1000 of the total number of events –, it is similar to the frequency of having any shifted FADC module for most runs. Therefore, the correction is only applied to the

runs where the percentage of anomalous PS events is higher than 0.5 %. In these runs, once a PS event is found to be shifted, it is corrected by delaying all the signal times belonging to channels inside the shifted modules. The introduced delay time is determined by the time differences among modules calculated from the Gamma Flash signals. This correction leaves less than 0.5 % of PS events with any module shift problem in the worst cases (runs with any shift on 15 % of the PS events).

This kind of correction based on the Gamma Flash signal only works with modules that include any anode channel. For those FADC modules that only contain cathode channels, the Gamma Flash signal obtained cannot distinguish a 20 ns shift and consequently the shift cannot be corrected. However, as the couples of FADC channels connected to the same cathode are placed in the same module, the signal position in the cathode is not affected because it is given by the time difference between the *siamese* signals which cancels any possible module shift. On the contrary, the diagonal condition (Equation 4.1) is affected, so we have to consider less restrictive limits for the runs where the FADC anomalous behaviour is relevant.

Appendix B

The linear momentum transfer (LMT)

In this appendix, the LMT correction in the emission angle is calculated for different neutron energies. The LMT effect [90] is characterised by the parameter

$$\eta = \frac{p_\parallel}{2p_0} \tag{B.1}$$

where $p_\parallel$ denotes the average longitudinal component of the transferred linear momentum and p_0 is the average momentum of the fragment in the center-of-mass (CM) frame.

The linear momentum transfer has scarcely been studied for neutron-induced reactions with uranium isotopes, so that values from proton-induced reactions on ^{238}U were used to estimate the fraction of linear momentum transferred in function of the neutron energy [91]. The value of p_0 is deduced from the total average kinetic energy release in fission, that is predicted by systematics [35].

The LMT correction markedly disturbs the angular distribution in the laboratory frame. Nevertheless, when trying to apply the LMT correction in the PPAC setup, it must be pointed out that we do not measure the angle of the fission fragment with respect to the neutron axis, but the angle between the axis that connects the fission fragment positions in the detectors and the neutron axis. These angles match when the laboratory and the center-of-mass frames coincide.

When the LMT correction corresponding to our angle is obtained, we realise that it hardly changes after the transformation to the center-of-mass frame. For example, for an angle in the CM frame of 60° and 150 MeV neu-
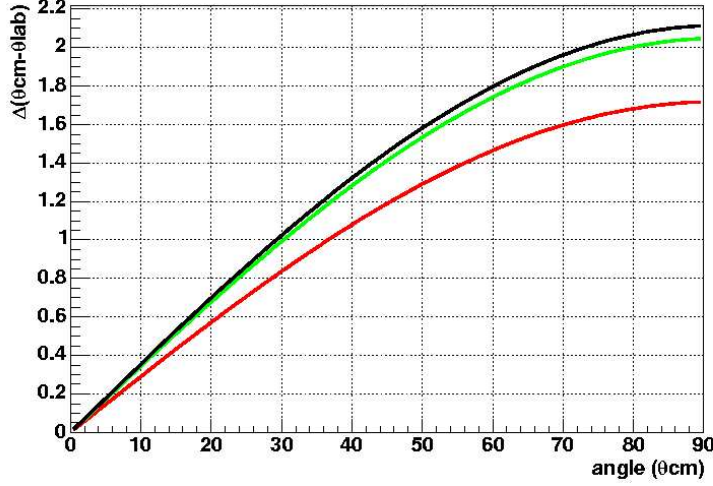
Figure B.1: *The variation due to LMT in the emission angle of the forward FF from ^{238}U fission is shown with respect to the angle measured in the center of mass frame for different neutron energies: 40 MeV (red), 90 MeV (green) and 150 MeV (black). The difference with respect the angle measured in the laboratory frame is larger for larger angles (measured with respect to the beam axis) and higher neutron energy, but for energies above 100 MeV the difference in the angle is almost constant because the fraction of linear momentum transferred decreases.*

tron energy, the conditions that maximize the LMT effect, the corresponding angle we obtained is 60,10°, indicating a correction of 0.15 %. Therefore, the error introduced by neglecting this effect is much smaller than the solid angle accuracy estimated for the PPAC setup (around 2 %). Consequently, the LMT correction in the FF emission angle has been omitted.

What remains to be studied is the effect of this correction on the detector efficiency. The relevance in the efficiency can be important at high neutron energies because the path of the fission fragment going backward is increased as the angle θ_{lab} is larger than the angle θ_{CM} for this fragment, which is also the fragment crossing the backing.

Appendix C

Energy Resolution: Experimental Determination

In time-of-flight measurements, the neutron kinetic energy is determined from the values obtained for the path length and the flight time by means the nonrelativistic formula:

$$E = (72.29825 \frac{L}{T})^2 \tag{C.1}$$

According to this, the energy resolution can be expressed by:

$$\frac{\delta E}{E} = \frac{2}{L} \sqrt{(\delta L)^2 + 1.913 \cdot E \cdot (\delta T)^2} \tag{C.2}$$

where δL is the uncertainty in the effective length of the flight-path in cm and δT is the uncertainty in the measurement of the time T in μs, taken to cover the distance L and E is measured in eV.

In a TOF measurement, time and distance uncertainties are determined by the characteristics of the basic equipment, i.e. accelerator and target-moderator assembly, and the detection system of the observed neutron reaction. Here we deal only with the first part. Consequently the main contribution to δL is the uncertainty of the moderation distance in the target-moderator, while δT is only the with of the proton pulse (7 ns). In the case of n_TOF, δL is strongly dependent, on the energy due to the large target size. From the moderation distance distribution [52] for different neutron energy the shape is skewed by a long tail, and the FWHM and the tail extension increase in the 100 keV region due to the moderation in the lead. As result, δT dominates the resolution at high energies, while δL is dominant al low energy.
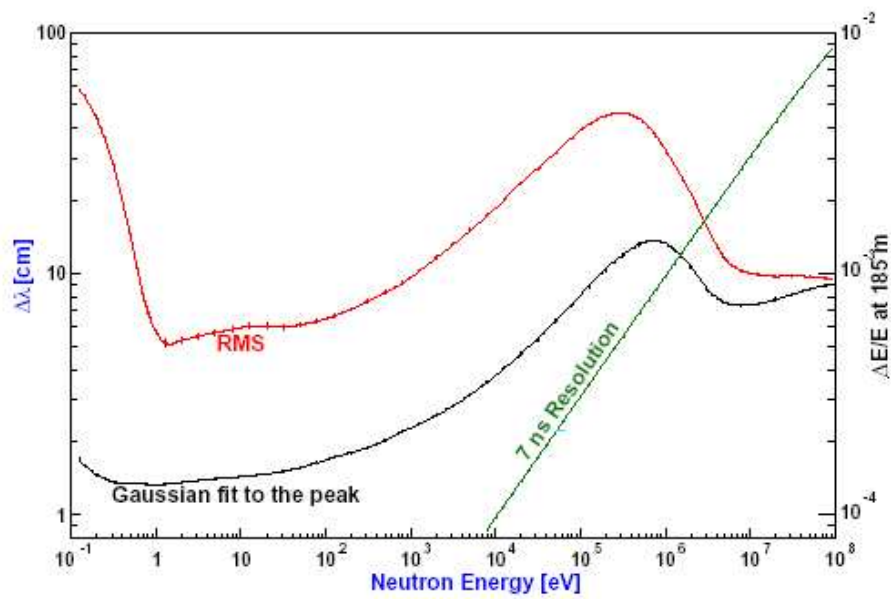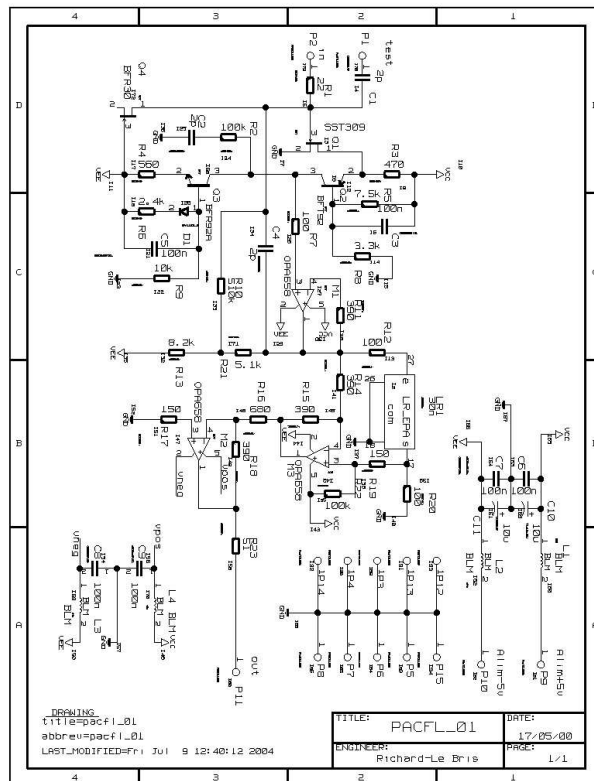
Figure C.1: *Monte Carlos simulation of the energy resolution at 185 m. The 7 ns resolution due to the proton beam becomes important for neutron energies above a few MeV.*

Appendix D

PPAC preamplifiers

Bibliography

[1] *Key world energy statistics*, Report by the International Energy Agency, 2004. http://www.oecd.org/topicstatsportal

[2] *Statistical Review of World Energy 2003*, BP Statistical Review of World Energy, 2003. http://www.bp.com

[3] *Nuclear power is the only green solution*, J. Lovelock, published in The Independent - 24 May 2004.

[4] *Introductory nuclear physics*, K.S. Krane, John Wiley & Sons, 1987.

[5] *A Technology Roadmap for Generation IV Nuclear Energy Systems. Technical Roadmap Report, September 2002.* Available from http://gif.inel.gov/roadmap/

[6] *Accelerator-driven Systems (ADS) and Fast Reactor (FR) in Advanced Nuclear Fuel Cycles. A comparative study*, Nuclear Energy Agency (NEA), 2002. Available from NEA web page: http://www.nea.fr/html/ndd/reports/2002/nea3109.html

[7] *A European Roadmap for Developing Accelerator Driven Systems (ADS) for Nuclear Waste Incineration*, The European Technical Working Group on ADS, April 2001.

[8] *A Roadmap for Developing Accelerator Transmutation of Waste (ATW) Technology*, USA Department of Energy, October 1999.

[9] *World Nuclear Association Report.* http://www.world-nuclear.org/info/inf62.htm

[10] *Thorium-based nuclear fuel: Current status and perspectives*, IAEA-TECDOC-412.

[11] *A strategic view on nuclear data needs*, Report by the NEA Secretariat. September 1993.

[12] *Measurements of Fission Cross Sections for the Isotopes relevant to the Thorium Fuel Cycle*, n_TOF Collaboration, CERN-INTC-2001-025.

[13] A. Trkov and D. W. Muir, Journal of Nucl. Sci. and Tech., Supp. 2, 1454 (2002).

[14] S. Bjornholm and J.E. Lynn, Rev. Mod. Phys., Vol. 52 No. 4 725 (1980).

[15] V. M. Strutinsky, Nucl. Phys. A95 (1967) 420.

[16] J. Blons, Nucl. Phys A502 (1989) 121.

[17] *A Detailed Study of Hyperdeformed States of Uranium in the 234U(n,f) Reaction*, The n_TOF Collaboration, Addendum to Proposal CERN-INTC-2001-025;INTC/P145.

[18] M. J. Lopez-Jimenez, Annals of Nuclear Energy 32 (2005) 195.

[19] *A high Resolution Spallation driven Facility at the CERN-PS to measure Neutron Cross Sections in the Interval from 1 eV to 250 MeV*, C. Rubbia et al., CERN/LHC/98-02 (EET), (1998) and CERN/LHC/98-02 (EET)-Add.1, (1998).

[20] *Proposal for a Neutron Time Of Flight Facility*, The n_TOF Collaboration, CERN/SPSC 99-8, SPSC/P 310 (1999).

[21] O. Hahn and F. Strassmann, Naturwissenschaften, 27 (1939) 11.

[22] *Nuclear Fission*, R. Vandenbosch, J.R. Huizenga, Academic Press, New York 1973.

[23] *The Nuclear Fission Process*, C. Wagemans, CRC Press, London 1991.

[24] *The Mechanism of Nuclear Fission*, N. Bohr and J. A. Wheeler, Phys. Rev. 56 (1939) 426.

[25] O. Haxel, Phys. Rev. 75 (1949) 1976.

[26] S. G. Nilsson, Kgl. Dan. Vid. Selsk., Mat. Fys. Medd., 29 No. 16 (1955).

[27] S. M . Polikanov et al. Zh. Eksp. Teo. Fiz., 42 (1962) 1464.

[28] F. Gönnenwein et al., Europhys. News 36 (2005) 1.

[29] M. C. Duijvestijn et al., Phys. Rev. C, 64 (2001) 014607.

[30] L.E. Glendenin et al. Phys. Rev. C24 (1981) 2600.

[31] J. Benlliure et al., Nucl. Phys. A628 (1998) 458.

[32] L.E. Glendenin et al. Phys. Rev. C22 (1980) 152.

[33] A. Bohr, Procceedings of the International Conference on the Peaceful Uses of Atomic Energy (United Nations, New York), Vol 2, p. 151.

[34] A.N. Behkami et al., Phys. Rev. 171 (1968) 1267.

[35] V. E. Viola et al., Phys. Rev C31 (1985) 1550 .

[36] F. Flynn et al., Phys. Rev.C 5 (1972) 1725.

[37] F. Pleasonton, Phys. Rev. 174 (1968) 1500).

[38] I. Ryzhov, Journal of Nucl. Sci. Tech., Supp. 2 (2002) 295.

[39] *Technical Report*, The n_TOF Collaboration, CERN/INTC 2000-018 (2000).

[40] *n_TOF Status Report*, The n_TOF Collaboration, CERN/INTC 2001-021, July 2001.

[41] *CERN n_TOF Facility: Performance Report*, U. Abbondanno et al., The n_TOF Collaboration, CERN-SL-2002-053 ECT (2002).

[42] *Results from the commissioning of the n_TOF spallation neutron source at CERN*, C. Borcea et al., Nucl. Inst. Meth. A 513 (2003) 524.

[43] *Development of a pulse shape analysis routine prototype for the Pickup signal*, J. Azevedo-Lucas et al., n_TOF internal note.

[44] *First parametrisation of the neutron source at the n_TOF and its influence on the collimation system*, D. Cano-Ott et al., CIEMAT Ref: DFN/TR-03,II-00.

[45] *Proposal for a two-step cylindrical collimator system for the n_TOF facility*, D. Cano-Ott et al., CIEMAT Ref: DFN/TR-04,II-00.

[46] *Design of a collimator for the neutron time of flight (TOF) facility at CERN by means of FLUKA/MCNP4b Monte Carlo simulation*, DFN/TR-07/II-99

[47] *An optimized C6D6 detector for studies of resonance-dominated (n,g) cross-section*, R. Plag et al., Nucl. Inst. Meth. A 496 (2003) 425.

[48] *A low background neutron flux monitor for the n_TOF facility at CERN*, S. Marrone et al., Nucl. Inst. Meth. A 517 (2004) 21.

[49] *Estudio de un monitor de neutrones para la instalación n_TOF*, Carlos Paradela, Thesis Diploma memory, 2001.

[50] V. Vlachoudis et al., Monte Carlo Simulation of the Neutron Time of Flight Facility at CERN, Proceedings of the Monte Carlo 2000 Conference, Lisbon (2000)

[51] J. Pancin et al., Nucl. Inst. Meth A, 524 (2004) 102.

[52] C. Coceva et al., Nucl. Inst. Meth A 489 (2002) 346.

[53] *Resolution Function and Flux from TOF02 C6D6 measurements*, C. Domingo and J. L. Tain, n_TOF Internal Note IFIC-2002-3.

[54] G. Lorusso et al., Nucl. Inst. Meth A 532 (2004) 622.

[55] *A comprehensive study of the n_TOF Background*, A. Ferrari, C. Rubbia and V. Vlachoudis, n_TOF Note 211009. SL-EET Note 2001-036.

[56] *Study of the Background in the Measuring Station at the n_TOF Facility at CERN: Sources an Solutions*, The n_TOF Collaboration, CERN/INTC 2001-038.

[57] *Experimental Techniques in Nuclear Physics*, D.N. Poenaru and W. Greiner, Walter de Gruyter, Belin 1997.

[58] A. Breskin and N. Zwang, Nucl. Inst. Meth. 144 (1977) 609.

[59] H. Stelzer, Nucl. Inst. Meth. 133 (1976) 409.

[60] A.A. Kotov et al., Nucl. Inst. Meth. 178 (1980) 55.

[61] L. Bianchi et al., Nucl. Inst. Meth. A276 (1989) 509.

[62] D. Harrach and H.J. Specht, Nucl. Inst. Meth. 164 (1979) 477.

[63] A. Breskin and N. Zwang, Nucl. Inst. Meth. 146 (1977) 461.

[64] *Neutron-induced fission cross section Measurements between 1 eV and 250 MeV*, C. Stephan et al., Journal of Nucl. Sci. Tech., Sup. 2 (2002) 276.

[65] *Mesures de sections efficaces de fission induite par neutrons sur les actinides du cycle du thorium a n_TOF*, Laure Ferrant, thesis Univ. de Paris-Sud.

[66] *The data acquisition system of the neutron time of flight facility n_TOF at CERN*, U. Abbondanno and the n_TOF Collaboration, Nucl. Inst. Meth. A 538 (2005) 692.

[67] *Extraction of PPAC signals*, L. Tassan-Got. Internal Paper.

[68] CASTOR: CERN Advanced Storage Manager, http://www.castor.web.cern.ch

[69] http://www.acqiris.com/Products/Digitizers/index.jsp

[70] *ROOT - An Object Oriented Data Analysis Framework*, Rene Brun and Fons Rademakers, Proceedings AIHENP'96 Workshop, Lausanne, Sep. 1996, Nucl. Inst. and Meth. in Phys. Res. A 389 (1997) 81-86. See also http://root.cern.ch/.

[71] *C++ Interpreter - CINT*, Masaharu Goto, CQ publishing, ISBN4-789-3085-3 (Japanese).

[72] *Fission of actinides induced by neutrons at n_TOF*, L. Tassan-Got, Proceedings of ND2004 Conference, Santa Fe, September 2004. Available from n_TOF web page.

[73] http://geant4.web.cern.ch/geant4/

[74] *The Stopping and Range of Ions in Matter*, J.F. Ziegler. Software available from http://www.srim.org

[75] G.A. Tutin et al., Nucl. Inst. Meth. A457 (2001) 646.

[76] R.B. Leachman and L. Blumberg, Phys. Rev. 137B (1965) 814.

[77] J.E. Simmons and R.L. Henkel, Phys. Rev. 120 (1960) 198.

[78] R.L. Henkel and J.E. Brolley, Phys. Rev. 103 (1956) 1292.

[79] J.E. Brolley and W. C. Dickinson, Phys. Rev. 94 (1954) 640.

[80] J.E. Brolley et al., Phys. Rev. 99 (1955) 159.

[81] *A Practical Guide to Splines*, C. de Boor, Springer-Verlag, 1978.

[82] http://www.mathworks.com/

[83] *Standards evaluation results*, R. Capote, Internal communication.

[84] Intermediate structure studies of ^{234}U cross sections. G.D.James et al. Phys. Rev. C 15 (1977) 2083

[85] R.W. Lamphere and R.E. Greene, Phys. Rev. 100 No 3 (1955) 763.

[86] R.W. Lamphere, Phys. Rev. 104 (1956) 1654.

[87] A.M. Lane and R.G. Thomas, Rev. Mod. Phys. 30 (1958) 257.

[88] C. Wagemans et al., IRMM Scientific Report (2002) 64.

[89] A.V. Prokofiev, Nucl. Inst. Meth. A463 (2001) 557.

[90] *Angular distribution of fragments from neutron-induced fission of ^{238}U in the intermediate energy region*, Magnus Carlsson, Uppsala University Neutron Physics Report ISSN 1401-6269. June 2004.

[91] M. Fatyga et al., Phys. Rev. C 32 (1985) 1496.

[92] *Updated Users' Guide for SAMMY: Multilevel R-Matrix Fits to Neutron Data Using Bayes' Equation*, N.M. Larson, ORNL/TM-9179/R3, ORNL (Sept. 1996) (Included in PSR-158).